Wireless Applications of Radio Frequency Micro-Electro-Mechanical Systems

Yi Yang

A thesis in fulfillment of the requirements for the degree of
Doctor of Philosophy

UNSW
SYDNEY·AUSTRALIA

in the
School of Electrical Engineering and Telecommunications
Faculty of Engineering

March 2014

PLEASE TYPE

THE UNIVERSITY OF NEW SOUTH WALES
Thesis/Dissertation Sheet

Surname or Family name: **Yang**

First name: **Yi** Other name/s:

Abbreviation for degree as given in the University calendar: **Ph.D.**

School: **School of Electrical Engineering and Telecommunications** Faculty: **Engineering**

Title: **Wireless applications of radio frequency micro-electro-mechanical systems**

Abstract:

With mass proliferation of wireless communication technologies, there is a continuous demand on fast data transmission rate and efficient use of frequency spectrum. As a result, reconfigurable systems are of significant importance and research is being conducted in numerous universities.

The purpose of this research is to develop novel RF MEMS based reconfigurable wireless systems. By utilizing the RF MEMS switches as a basic building block, this thesis focus on developing a unique design technique for the design and development of RF MEMS delay line phase shifter, frequency reconfigurable antennas and pattern reconfigurable antennas. This thesis work is divided into four parts:

1. Investigation and development of nano-electro-mechanical systems (NEMS) based 3-bit phase shifter. Analyzing the slow wave structure to further reduce the size of delay line phase shifter.

2. Development of frequency reconfigurable antennas to compete with broadband and multi-band antennas. Two novel MEMS-loaded frequency reconfigurable antennas were designed with spectrum switchable between WPAN band (57 to 66 GHz) and the whole E-band (71 to 86 GHz).

3. Investigation of microstrip-to-coplanar striplines (CPS) transition balun used for antennas to explain the inherent phase delay of this type of structure. Based on the discovery, a pattern reconfigurable quasi-Yagi antenna was designed. The antenna exhibits excellent RF performance, compact size and switchable end-fire radiation pattern with the goal to replacing existing phased array antennas. It has the full functionality of a multi-antenna phased array plus phase shifting network while its size is same as a fixed single Yagi antenna.

4. Development of full seven masks all metal fabrication process of the RF MEMS integrated reconfigurable antennas. The fabrication processes are optimized based on Australian National Fabrication Facility (ANFF) New South Wales node's equipment.

Signature	Witness	**30/March/2014** Date

FOR OFFICE USE ONLY Date of completion of requirements for Award:

Copyright Statement

I hereby grant the University of New South Wales or its agents the right to archive and to make available my thesis or dissertation in whole or part in the University libraries in all forms of media, now or here after known, subject to the provisions of the Copyright Act 1968. I retain all proprietary rights, such as patent rights. I also retain the right to use in future works (such as articles or books) all or part of this thesis or dissertation.

I also authorise University Microfilms to use the 350 word abstract of my thesis in Dissertation Abstract International (this is applicable to doctoral theses only).

I have either used no substantial portions of copyright material in my thesis or I have obtained permission to use copyright material; where permission has not been granted I have applied/will apply for a partial restriction of the digital copy of my thesis or dissertation.

Signed ……………..……………..…………………............

Date …………………30/March/2014……………............

Authenticity Statement

I certify that the Library deposit digital copy is a direct equivalent of the final officially approved version of my thesis. No emendation of content has occurred and if there are any minor variations in formatting, they are the result of the conversion to digital format.

Signed ………………...……………………..……………………............

Date …………………30/March/2014……………….............

Originality Statement

I hereby declare that this submission is my own work and to the best of my knowledge it contains no materials previously published or written by another person, or substantial proportions of material which have been accepted for the award of any other degree or diploma at UNSW or any other educational institution, except where due acknowledgement is made in the thesis. Any contribution made to the research by others, with whom I have worked at UNSW or elsewhere, is explicitly acknowledged in the thesis. I also declare that the intellectual content of this thesis is the product of my own work, except to the extent that assistance from others in the project's design and conception or in style, presentation and linguistic expression is acknowledged.

Signed ……………...……………………………………….............

Date …………………30/March/2014……………….............

Abstract

With mass proliferation of wireless communication technologies, there is a continuous demand on fast data transmission rate and efficient use of frequency spectrum. As a result, reconfigurable systems are of significant importance and research is being conducted in numerous universities and scientific centers.

In this thesis, novel designs based on radio frequency micro-electro-mechanical systems (RF MEMS) that can lead to the reconfigurable wireless transceivers are proposed. By utilizing the RF MEMS switches as a basic building block, this thesis focus on developing a unique design technique for the design and development of RF MEMS delay line phase shifter, frequency reconfigurable antennas and pattern reconfigurable antennas.

- Nano-electro-mechanical systems (NEMS) switches based 3-bit phase shifter was designed and investigated. Problems like high insertion loss of the transmission line, CPW bend phase error and impedance mismatch of the T-junction were encountered during the design. The enlarged delay line, air bridges and a miter step connector were employed to the design to overcome these drawbacks.
- Two types of slow wave structures are proposed and. The purpose of this work is to further reduce the size and cost of existing microwave circuits. Especially for the delay line type phase shifter I designed, the transmission line occupies most

of space on the substrate.

- Two new RF MEMS-integrated millimeter-wave frequency reconfigurable antenna is then proposed. The operation frequency of the antenna is switchable between the millimeter wave 60 GHz WPAN band (57-66 GHz) and E-band (71-86 GHz) by actuating of the RF MEMS switches employed on the driven and director dipole elements.
- A novel new type of RF MEMS-integrated millimeter-wave pattern reconfigurable quasi-Yagi antenna is proposed. The E-plane radiation beam direction is switchable between -15°, 0° and 15°by actuating of the RF MEMS switches on the driven dipole and transition delay line elements. This design can replace the bulky and complex phased array consists of phase shifting network and multiple antenna configuration, while has the size same as a single fixed Yagi antenna. A germanium very low conductivity biasing configuration is used for antenna design for the first time. The germanium lines are invisible to the antenna at 60 GHz therefore guarantees the excellent radiation performance.
- A full seven-mask all metal fabrication process of the RF MEMS integrated reconfigurable antenna is proposed and optimized based on the equipment provided in the Australian National Fabrication Facility (ANFF) labs located in the University of New South Wales.

Acknowledgements

It has been a long journey since I started my Ph.D. in July 2010. I do not want to look back on the countless sleepless nights I have spent for my research. I would however, like to express my sincere gratitude to the following people, without them, I could not finally be here.

First, I wish to express my appreciation and gratefulness to my supervisor Professor Rodica Ramer from UNSW for her guidance, insight and care. She is my mentor not only in academic research also personal character formation. It could be a much tougher road for me if without her supports. She is my lifetime friend and a great figure to follow.

I would like to thank Dr. King Yuk Chan who introduced me to the world of MEMS and give me kind guidance in my academic works. Thanks all my friends and colleagues in the Microsystems Group and office 318 in UNSW, with whom I have had the pleasure to work over the years. Thank you Yuanyuan Yang, Vicki Zhu, Eugene Siew, Dr. Daniel Krcho and Liang Gong for your collaboration and help with my research.

My family is the most precious treasure in my life. They motivate, encourage and support me with all their efforts over the years. I own them too much and my affection to them cannot be expressed using any word. My deepest gratitude goes to my family: Guiyong Yang, Jin Wang and Guoxin Teng!

LIST OF PUBLICATIONS

Journals

Y. Yang, K. Y. Chan, N. Nikolic and R. Ramer, "Experimental Proof for Pattern Reconfigurability of 60GHz Quasi-Yagi Antenna," under review of IEEE Antenna and Wireless Propagation Letters.

L. Gong, **Y. Yang**, K. Y. Chan, and R. Ramer, "An RHCP Pattern Reconfigurable Spiral Antenna Biased with Two DC Signals," accepted by Mobile and Optical Technology Letters, 2013.

Conferences

Y. Yang, K. Y. Chan and R. Ramer, "60GHz Pattern Reconfigurable Quasi-Yagi Antenna-Proof through Computational Design," 2014 IEEE International Workshop on Antenna Technology (iWAT), 4-6 March 2014.

Y. Yang, K. Y. Chan, R. Ramer, "Comparison of 60 GHz quasi-Yagi antennas using different microstrip-to-CPS transitions," Wireless Information Technology and Systems (ICWITS), 2012 IEEE International Conference on, 11-16 Nov. 2012

Y. Yang, Y. Cai, K. Y. Chan, R. Ramer, Y. J. Guo, "MEMS-loaded millimeter wave frequency reconfigurable quasi-Yagi dipole antenna," Microwave Conference Proceedings (APMC), 2011 Asia-Pacific , pp.1318-1321, 5-8 Dec. 2011.

E. Siew, K. Y. Chan, Y. Cai, **Y. Yang**, R. Ramer, A. Dzurak, "RF MEMS-integrated frequency reconfigurable quasi-Yagi folded dipole antenna," Microwave Conference Proceedings (APMC), 2011 Asia-Pacific, pp.558-561, 5-8 Dec. 2011.

Y. Yang, K. Y. Chan, R. Ramer, "Design of 600 GHz 3-bit delay-line phase shifter using RF NEMS series switches," Antennas and Propagation (APSURSI), 2011 IEEE International Symposium on, pp.3287, 3290, 3-8 July 2011.

TABLE OF CONTENTS

LIST OF FIGURES

LIST OF TABLES

LIST OF ABBREVIATIONS

3D	Three-dimensional
Au	Gold
CMOS	Complementary metal-oxide-semiconductor
CPS	Coplanar stripline
CPW	Coplanar waveguide
Cr	Chromium
dB	Decibel
DI	Deionized
DC	Direct current
FET	Field-effect transistors
GaAs	Gallium arsenide
HFSS	High frequency structure simulator
HMDS	HexaMethylDiSilazan
IPA	Isopropyl alcohol
IC	Integrated circuit
IIP3	Third-order intercept point
LHP	Left hand polarized
MEMS	Micro-electro-mechanical systems
MMIC	Monolithic microwave integrated circuit

NEMS	Nano-Electro-Mechanical Systems
NMP	N-Methyl-2-pyrrolidone
RF	Radio frequency
RHP	Right hand polarized
RIE	Reactive ion etching
Ti	Titanium
UNSW	University of New South Wales
UV	Ultra violet
VNA	Vector network analyzer

CHAPTER 1

INTRODUCTION

1.1. MOTIVATION

Over the last three decades, wireless technologies are being increasingly used in our daily lives. The market of wireless products has shown a surprisingly growth. Today mobile devices such as mobile phones process not only voice but also digital data packets and GPS signals. With the explosion of high speed data transmission, wireless components have to handle multiple frequency bands as well as provide special diversity for multi input and multi output signals depending of the situations. A conventional approach is to utilize multiple transceivers in one device. However, this approach increases the cost, size, and power consumption, so these devices mostly have a shorter battery life. A more preferable approach is the reconfigurable wireless communication systems with multifunctional capabilities. This solution not only increases the bandwidth, reduce the noise, but also allows the device to operate with arbitrary network protocols which unveils the potential of wireless technologies, most importantly lower manufacturing costs. However, to facilitate such wireless communications devices, new technologies and fabrication processes for circuits, devices and components, as well as the development of new materials are required.

A key component to enable reconfigurable wireless communication devices is a switch. It is a component to connect or disconnect different circuits within a reconfigurable system. Currently, there are two dominating categories for wireless communication switches. They are the mechanical switches and the semiconductor switches. The most common types of mechanical switches are coaxial type and waveguide type. They offer very low insertion loss at ON state (connected) and very high isolation at OFF state (disconnected). These switches can handle very high power as well. However, the mostly known drawback of this type of switches is their bulky physical sizes and heavy weight. Also, being mechanical switches, they inherently have relatively slow switching speed. The most well-known semiconductor switches are the FET switches and PIN diodes. They offer very high switching speed, small physical size and lower weight. But because of their switching mechanism where switching is done by generating and choking electrical channels, they usually have much higher insertion loss and DC power dissipation. Also because of this reason, their OFF state isolation is very limited and power handling is generally poor.

Micro-electro-mechanical systems, a completely new type of switch is becoming no longer a far-fetched idea but a real opportunity due to the mature of CMOS fabrication technologies. MEMS switches have both the advantages of mechanical and semiconductor switches. MEMS switches are small in size and weight, low in cost and provide good radio frequency (RF) performance. These switches exhibit high linearity with higher operational bandwidth as compared to the existing standard technology. Major application for RF MEMS switches include mobile communications, test equipment, telecom infrastructures, aerospace and defense.

Phase shifter is an essential component found in microwave and millimeter-wave communication, radar and phased array antennas. Currently, the phase shifters are based on PIN diodes, ferrite materials or FET switches. The advantage of PIN diode phase shifters is that they provides low loss in the device, but consume more power than FET switches. The FET-based shifter can be built on the same substrate with the amplifiers, thereby reducing the assembly cost. The ferrite device can handle high RF power while offering excellent performance, but they are very expensive to fabricate and consume a relatively high DC power than the other two types of phase shifter. So that the role of MEMS switches in phase shifter designs can be immediately seen. MEMS switches result in considerable reduction in the DC power and lower loss. Since MEMS switches can be fabricated directly with antenna on ceramic, quartz or silicon wafers, they lead to a low cost phased array.

With mass proliferation of wireless communication technologies, reconfigurable antennas have received much attention since they can offer the diversity in radiation pattern, polarization, and operating frequency spectrum. In particular, pattern reconfigurable antennas can maneuver away from the noisy environment, improve security, and save the power, all by pointing the radiation beam toward the specific customers. These hallmarks used to be achieved with phased antenna arrays, which consume more surface area on a monolithic microwave integrated circuit (MMIC) and are complex to employ. Another important member of reconfigurable antenna family is frequency reconfigurable antenna. It allows one antenna being shared for multiple high data-rate wireless services. Frequency tunable antenna has been reported to serve several wireless communications air interfaces using varactor diodes. However, very little research work has been reported on the design of millimeter wave frequency reconfigurable antenna.

1.2. OBJECTIVES

The purpose of this research is to develop RF MEMS based reconfigurable wireless systems. By utilizing the RF MEMS switches as a basic building block, this thesis focus on developing a unique design technique for the design and development of RF MEMS delay line phase shifter, frequency reconfigurable antennas and pattern reconfigurable antenna. This thesis work is divided into four tasks:

1. Investigation and development of nano-electro-mechanical systems (NEMS) based 3-bit phase shifter. Analyzing the slow wave structure to discover the potential of reducing the size of delay line phase shifter.
2. Development of two novel frequency reconfigurable antennas to compete with broadband and multi-band antennas.
3. Investigation of microstrip-to-coplanar striplines (CPS) transition balun used for antennas to explain the inherent phase delay of this type of structure. Development of pattern reconfigurable antenna that exhibits excellent RF performance, compact size and switchable end-fire radiation pattern with the goal to replacing existing phased array antennas.
4. Development of full seven masks all metal fabrication process of the RF MEMS integrated reconfigurable antennas. The fabrication processes are optimized based on Australian National Fabrication Facility (ANFF) New South Wales node's equipment.

1.3. THESIS OUTLINE

The motivation and research objectives are outlined in chapter 1. Chapter 2 provides a brief review of mechanical and semiconductor switches. This chapter also presents an overview of existing RF MEMS switches and the theory behind them. In addition, a literature survey on RF MEMS phase shifter and reconfigurable antennas are illustrated. Chapter 3 gives a design approach of RF MEMS phase shifter. A 3-bit NEMS delay line type phase shifter has been demonstrated. After that two types of slow wave structure units and branch-line coupler based on them are presented. Chapter 4 presents two new design of millimeter wave frequency reconfigurable antennas using RF MEMS switches to change their working spectrum between WPAN band and E-band. Chapter 5 discusses the discovery found from the microstrip-to-CPS transition study, which has led to a new type of pattern reconfigurable antenna employing RF MEMS to realize the reconfigurability. In addition, a RHCP pattern reconfigurable spiral antenna is demonstrated using PIN diode technology. A seven-mask all metal MEMS integrated reconfigurable antenna fabrication process is detailed in Chapter 6. Chapter 7 summarizes the contribution of the thesis and proposes future works.

CHAPTER 2

BACKGROUND AND LITERATURE SURVEY

2.1. OVERVIEW

A review of RF switches is discussed at the beginning of this chapter. Conventional switches can be divided into two categories of mechanical and semiconductor switches. The advantages and shortcomings of these two types of RF switches are discussed and then some commercial switches and application examples are provided. An overview of MEMS technology is introduced. RF MEMS switches operation principle and RF MEMS switches types are then provided in detail. A brief literature survey on existing phase shifters and 60 GHz spectrum follows. Reconfigurable antennas along with the developed structures are then reviewed in the last part of this chapter.

2.2. CONVENTIONAL RF AND MICROWAVE SWITCHES

Communication systems involves radio frequency components to be utilized in high frequency applications. A very common device in the telecommunication networks is a RF switch. Applications include phase shifters, impedance tuning networks, tunable amplifiers and switch matrices. Switch is the sole device that encompass the entire spectrum of the electromagnetic wave, from a few hertz up to microwave and millimeter wave spectrum. Switches typically have two states: ON and OFF. These two states generates totally different effects to electrical circuits. RF switches can be integrated in series or shunt configuration depending on the utilization. In the series configuration these switches use to connect (ON) or break (OFF) a transmission line and in shunt configuration they either pass a signal or short it to ground. The evaluation of RF switches depends on many factors but critical factors like insertion loss and isolation are the most important ones because they determine the overall RF performance of the whole system. Another important factor is power consumption of the switches. Especially for mobile communication, people prefer to leave the charging cable behind so the battery is the only source to provide the power. With high power consumption, the size of the portable device gets larger due to the enlarged battery size. In the case of satellite, the only energy source available is from a solar cell which has limited output. In the following section, conventional RF switches are reviewed while their advantages and limitations are also presented.

2.2.1. MECHANICAL SWITCHES

A mechanical switch is a switch that achieves switching by mechanically connecting or breaking a signal path. It can be controlled either electronically or mechanically. A typical method to control RF mechanical switches is to apply different electrical signal using electromagnetic relays. However, in latching switches, the switches remain in a preselected position until state changes. This configuration must be pulse controlled with a pulse duration of 20ms to 100ms. Mechanical switches exist in many different forms. The most common form is a single-pole double-throw switch (SP2T) which has one input port and two selectable output ports. A multi-position switch is a switch that has one input ports and more than two selectable output ports. They are generally called single-pole, multi-throw or single-pole, N-throw switches or in short, SPMT or SPNT. Another common type of mechanical switch is the transfer switch. It has two independent paths that operate simultaneously in one of two selectable positions.

Figure 2.1 shows schematics of a typical SP2T and a transfer switch [1]. Figure 2.2 (a-b) shows a commercially available product of coaxial switch from Narda Microwave, L-3 Communications Corporation and DowKey Microwave Corporation [2-3]. Coaxial switch uses electromagnetic relays for switching operation. Power is applied to the actuation coils to change the states by moving the arm. The RF coaxial switch has a maximum switching speed of 15ms. Typical RF mechanical switches have very good RF characteristics. They can offer better than 0.5 dB insertion loss and 60 dB isolation at below 18 GHz [1]. Figure 2.2 (c-d) represent a waveguide switch from DowKey [1, 4-5]. Switching is done by rotating the waveguide from its normal position to the desired ports. Waveguide switches could be controlled manually or electronically with electrical signal applied on relays or motors. Waveguide switches generally offer very low insertion loss of 0.1 dB and a very high isolation of 60 dB at 18 GHz [4].

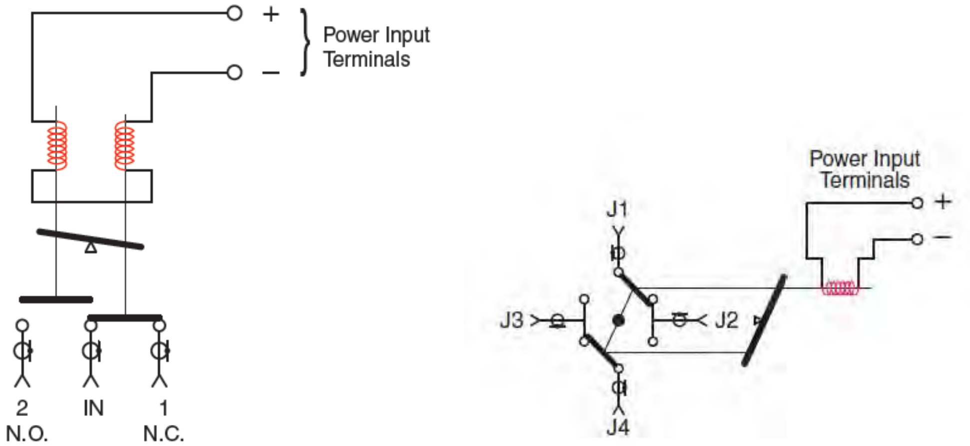

(a) (b)

Figure 2.1. Schematics of (a) a SP2T switch and (b) a transfer switch [1].

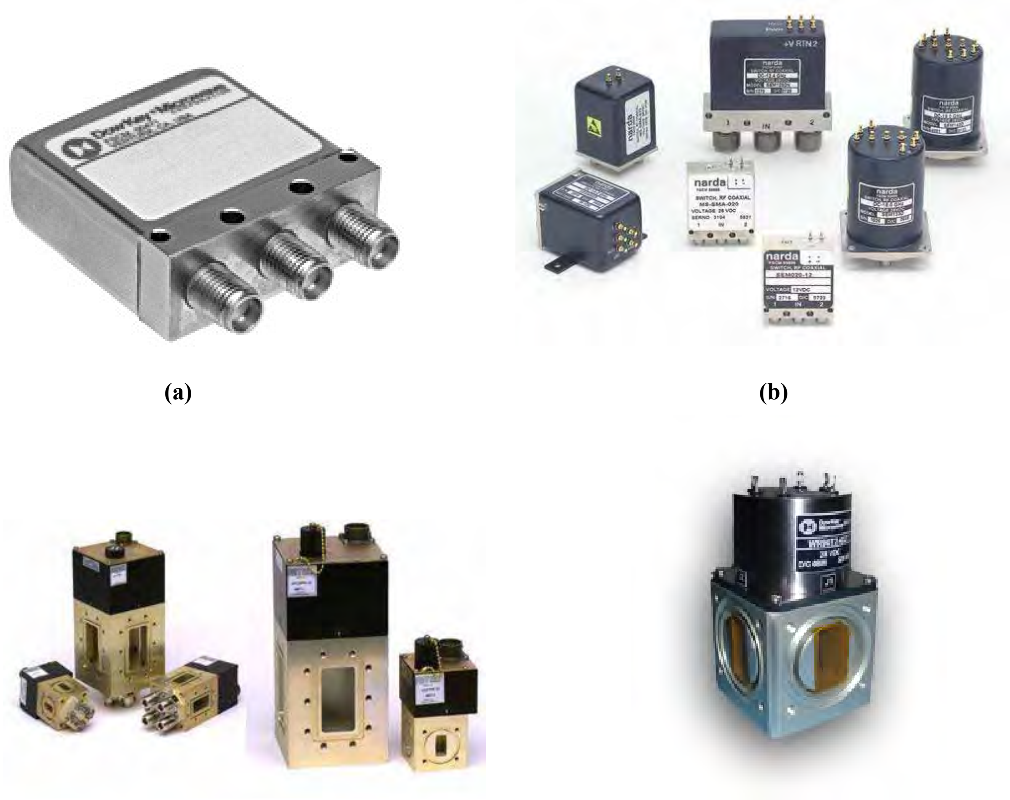

(a) (b)

(c) (d)

Figure 2.2. Pictures of mechanical switches, (a) (b) coaxial switches [5] and (c) (d) a waveguide switch [4].

Important characteristics of mechanical switches are that they offer superior RF performance and very good power handling capabilities. They are capable of carrying signal power up to kW range. The shortcomings of these switches are relatively slow switching speed, typically in the order of millisecond [6], very heavy weight and bulky size as can be seen in figure 2.2.

2.2.2. SEMICONDUCTOR SWITCHES

Mechanical switches are not suitable for applications require high speed switching. For those tasks of fast switching semiconductor or solid state switches are preferred. Semiconductor switches includes field-effect transistors (FET) and PIN diodes. Semiconductor switches are fabricated with gallium arsenide (GaAs) and silicon germanium (SiGe) for over 1 GHz utilizations. They are small in size and have much faster switching speed than mechanical switches. However, their RF characteristics and power handling capability is inferior when compared to mechanical switches.

The most common electronic switch is the PIN diode. PIN diodes can be employed in series or shunt configuration. They achieve low insertion loss in series design while provides high isolation in shunt design. The basic principle behind these devices is that they behavior as resistors or capacitors under different biases for an RF signal. Under zero or reverse bias, a PIN diode acts as a capacitor and will not pass much of an RF signal; while under forward bias, the channel of the diode changes from capacitive to resistive. A typical PIN diode will have a resistance of around 1Ω, which makes it a good RF conductor. Figure 2.3 shows the PIN diode switch configuration in series and shunt designs.

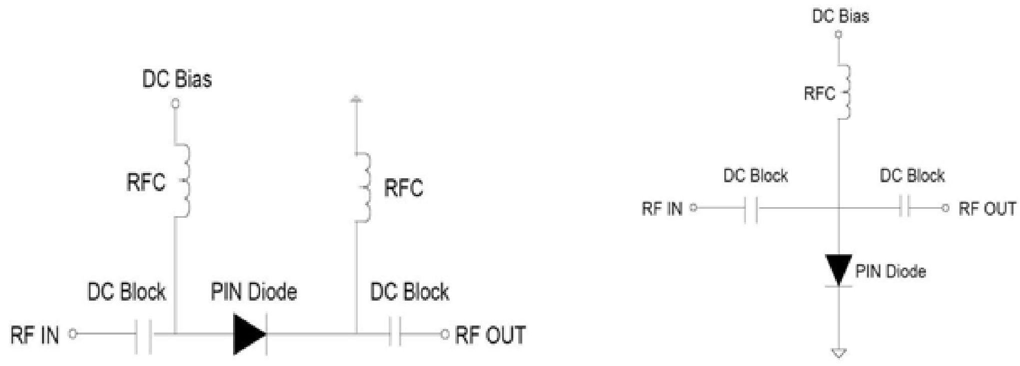

(a) **(b)**

Figure 2.3. PIN diode configured as (a) a series switch and (b) a shunt switch.

A major disadvantage of PIN diodes is that they consume DC power during ON state (forward bias). In applications such as mobile and satellite communications, where low power consumption is a critical criterion, they are replaced by FETs. FET switches are used as they consume little power. A FET switch is three terminal device in which gate voltage acts as the control signal as shown in figure 2.4. Other than the input and output ports (source and drain), it has a gate input to control its status. Due to that the control gate of a FET switch is not coupled with the source and drain, no bias network is required to separate the bias signal from the RF. A FET is turned ON when the gate voltage is greater than the pinch off voltage. Similar to PIN diodes, FETs are not perfect switches as they do not have perfect ON-OFF. FETs have a finite on resistance when conducting and has a finite off capacitance. Just like PIN diodes, FET switches can also be designed in series or shunt configuration. In both cases the FET can be turned ON or OFF by tuning the gate voltage. Figure 2.4 shows the FET switch in series and shunt configurations.

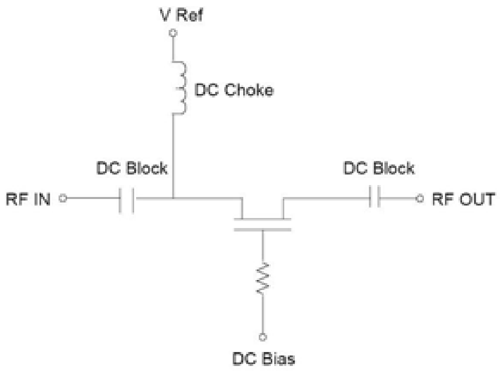

(a)

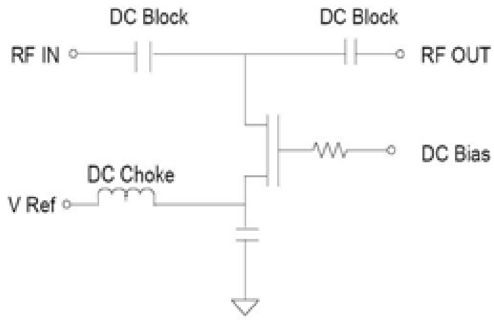

(b)

Figure 2.4. FET configured as (a) a series switch and (b) a shunt switch.

Typical FET has RF performance of 0.7-1.2dB insertion loss, 30dB isolation and 45 dBm IIP3 at 2.5 GHz. The drawback of FET switches is that they have low power handling capability while compared to PIN diodes [7]. The semiconductor switches can be manufactured in a hybrid integrated circuit or in Monolithic Microwave Integrated Circuitry (MMIC) circuits using different techniques as soldering or wire bonding. These approaches do not have any attached discrete component thus reduce losses. The advantages of MMIC technology are low manufacturing cost, compact size, simple package and better reliability. Figure 2.5 shows PIN diode and FET switches and switch matrix using above techniques.

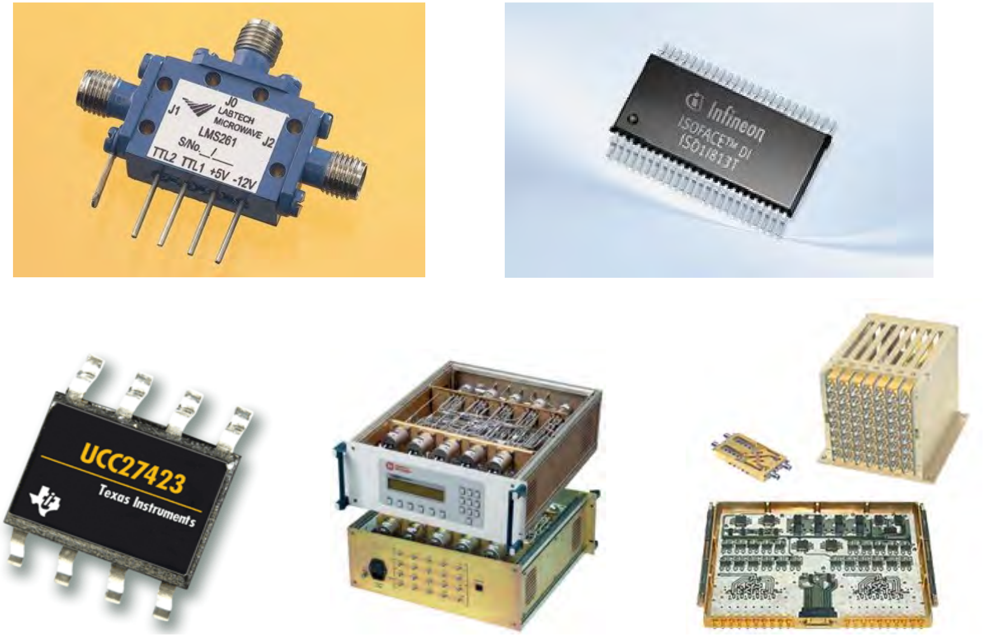

Figure 2.5. Semiconductor switches and switch matrices by different companies [1, 3, 8-10].

2.3. MEMS OVERVIEW

Micro-electro-mechanical Systems (MEMS) are also known as Microsystems Technology (MST) or micromachines. MEMS generally relate to micro-scale systems. MEMS are a combination of electrical and mechanical components on one substrate by using the microfabrication technology [11]. MEMS have competitive advantages such as good performance in terms of loss, isolation, linearity and power consumption. These type of devices are potential substitution of currently used semiconductor circuits. MEMS fabrication process are compatible with integrated circuits (IC) batch processing technique so their costs are reasonable for mass production. MEMS technology possess a number of distinct features. For example, they are miniature embedded systems which enable higher level functions and often integrate smaller functions together into one package for greater utility. They can also be cost effective through low unit pricing [12]. MEMS adopt significant parts from the IC technology which builds structures on silicon wafer with multilayer thin films of materials patterned using photolithographic methods. MEMS technology utilize basic process steps of deposition, lithography and etching [13]. The fast development of MEMS has led to many systems on chip and smart systems. An example of lab-on-a-chip includes the combined vacuum and shear driven system on a chip layout [14]. Smart systems are those circuits can gather the information (sensing), process it and implement the gathered information (computing) and affect through an actuator (actuating) [15]. While researchers have investigated MEMS like devices for the last three decades, Richard P. Feynman first predicted the development of micro scale devices in a lecture entitled " There's plenty of room at the bottom" in 1959 [16]. Many processes for deposition, patterning and etching were developed with the evolvement of IC industry in 1960s and 1970s. While physical properties like mass and area were significantly reduced, other properties like stress in thin films became significant.

Intense researches have been carried out during last two decades and the first MEMS structure as a simple sensor was fabricated. Since then MEMS have proven to be applicable in all areas of engineering systems such as microfluid, optical, bio-medical and microwave (Figure 2.6).

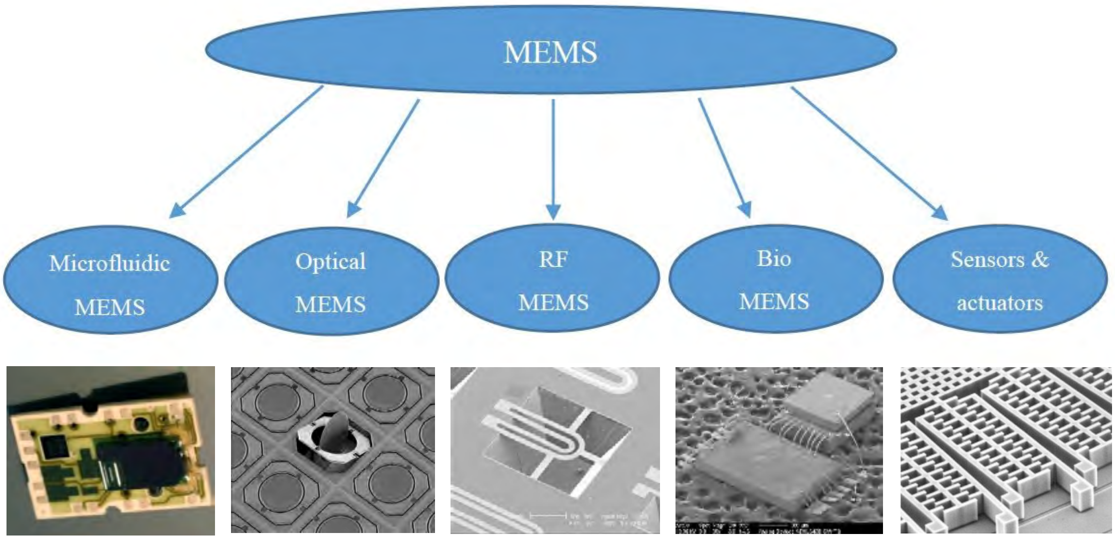

[17] [18] [19] [20] [21]

Figure 2.6. MEMS applications

2.4. RF MEMS

The term RF MEMS refer to the design and fabrication of MEMS for radio frequency integrated circuits [22]. The goal of RF MEMS is to extend the device benefits all the way to the system level to acquire unprecedented system performance [23]. There are two methods RF MEMS designers used to enhance the system performance. They are top-down and bottom-up design. In the top-down approach, devices and structures are made using many of the same techniques as used in MEMS except they are made smaller in size, usually by employing more advanced photolithography and etching methods. Designers develop new system level architectures as shown in [24-25]. The bottom-up approach typically involves deposition, growing, or self-assembly technologies.

2.5. RF MEMS SWITCHES

MEMS have been studied over the past few decades. Recently, MEMS technology has been utilized to fabricate RF switches. RF MEMS switches combine the advantages of both mechanical and semiconductor switches. RF MEMS switches are small in size, light in weight and offer very good RF performance. RF MEMS switches can also provide extremely low DC power consumption with certain actuation mechanism. Electrostatic actuation is the most commonly used actuation method. One reason is that it offers virtually zero power consumption as there is no DC current flowing.

Table 2.1. Electrical performance comparison of FETs, PIN diodes and RF MEMS electrostatic switches [26]

Parameter	RF MEMS	PIN	FET
Voltage (V)	20-80	±3-5	3-5
Current (mA)	0	3-20	0
Power consumption (mW)	0.05-0.1	5-100	0.05-0.1
Switching time	1-300 μs	1-100ns	1-100ns
C_{up} (series) (fF)	1-6	40-80	70-140
R_s (series) (Ω)	0.5-2	2-4	4-6
Capacitance ratio[b]	40-500[b]	10	n/a
Cutoff frequency (THz)	20-80	1-4	0.5-2
Isolation (1-10 GHz)	Vey high	High	Medium
Isolation (10-40 GHz)	Very high	Medium	Low
Isolation (60-100 GHz)	High	Medium	None
Loss (1-100GHz) (dB)	0.05-0.2	0.3-1.2	0.4-2.5
Power handling (W)	<1	<10	<10
Third order intercept point (dBm)	+66-80	+27-45	+27-45

a: Includes voltage up converter or drive circuitry; b: Capacitive switch only

Table 2.1 shows a summary between different switch technologies. Note that only electrostatic actuated MEMS switches are considered in the table. Ideally, MEMS, mechanical and FET switches do not consume DC power. However, because of their operation mechanisms, voltage converters are occasionally used in RF MEMS, mechanical and drive circuit in FET. The power consumption of these supporting circuits must be taken into account.

It is expected that manufacturing cost of MEMS switch fabrication can be driven down by mass production similar to PIN diode and FET switches. By comparing different technologies, MEMS based switches seem very promising and could possibly represent the replacement technology. Primary areas of concern for current researchers are reliability and packaging. For RF MEMS switches the reliability issue is improving steadily as stiction issues are being resolved with new release techniques. On the other hand, packaging has a significant impact on the system performance as moisture and dust can cause RF MEMS switch failure. Therefore a smart packaging solution is required for the good performance.

2.5.1. TYPES OF RF MEMS SWITCHES

RF MEMS switches can be classified in many different ways. They could be categorized in six classes based on their main attributes. These are: the actuation mechanism, switch movement direction, contact type, circuit configuration beam type and beam location. Table 2.2 summarized these characteristics in each attribute.

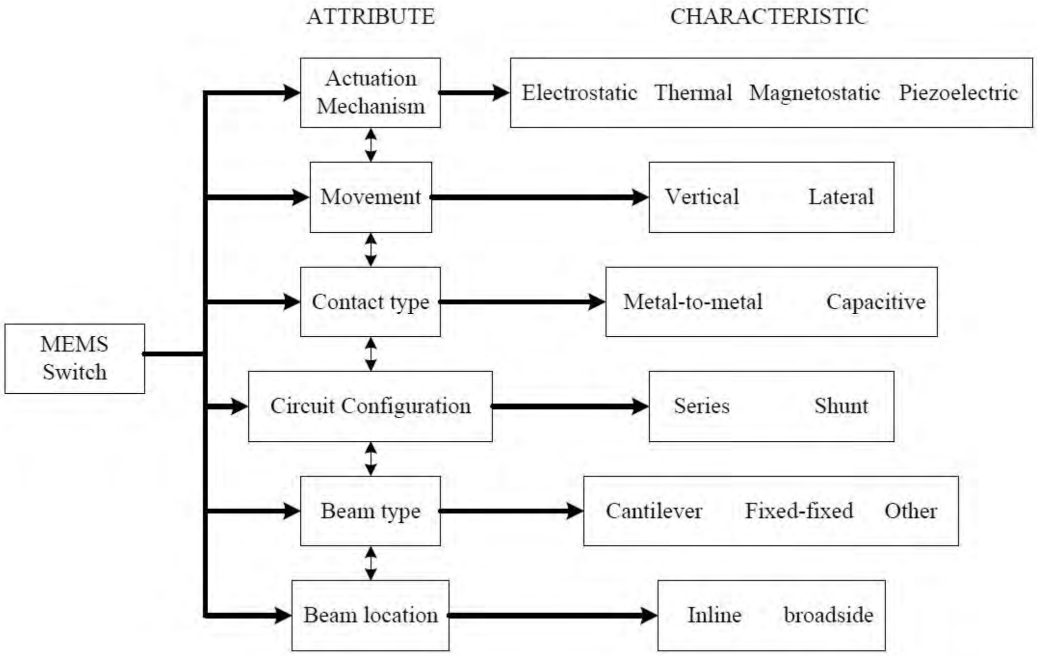

Table 2.2. MEMS switch type classification.

Currently, there are four main actuation mechanisms that are used for RF MEMS switches. These are the electrostatic, thermal, magnetostatic and piezoelectric actuations. Each of these exhibits different advantages and are suitable for different applications or situations. Electrostatic actuation is the most common technique. Same as the piezoelectric actuation, these two mechanism virtually consume no DC power. They are mostly used in power limited situations. They are relatively fast switches with switching speed in the range of a few to hundreds of microsecond. Thermal and magnetostatic types of MEMS switches only require very low actuation voltage. This is beneficial when integrating with solid state circuits as the voltage range is quite similar so no additional bias network is needed. However, as DC current is required for actuation, switching speed of these switches are usually slow. They could be ranging from hundreds of microsecond to a few milliseconds.

MEMS switches could be grouped by their moving direction. Depending on fabrication processes, MEMS switches can be designed to move vertically out of plane (small size) or laterally (large size).

Contact type is another criterion of grouping. RF MEMS switch could be of metal-to-metal (resistive) contact or capacitive contact. The only difference between the two is whether or not a direct metal-to-metal contact exists between the beam and the transmission line when the switches are actuated. In general, resistive metal-to-metal contact is chosen when wide band operation is essential (from DC to high frequency). This type of contact could be designed with very high isolation at low frequency as contact area could be customized to achieve the desired isolation. A capacitive contact is not functional at low frequency so they are chosen when low spectrum is not necessary. This type of contact usually allows much lower insertion loss at higher frequency because they do not suffer from the contact resistance exists in a metal-to-metal contact.

MEMS switches, like other switches, can be grouped by circuit configuration. MEMS can be configured as a series or a shunt switches. In a series configuration, MEMS switches are used to connect or break an RF signal path. While in a shunt configuration, they are used to either pass RF signals between input and output ports or to short the signals to ground.

RF MEMS switches can be cantilever beam or fix-fix membrane (beam) switches as shown in figure 2.7. A cantilever beam is a beam that is anchored on one side and is free to move on the other side. A fixed-fixed beam is a beam that is anchored on both sides of the beam and the beam can only move in the center. If both a cantilever beam and a fixed-fixed beam have the same dimensions, a cantilever beam would have a much smaller spring constant.

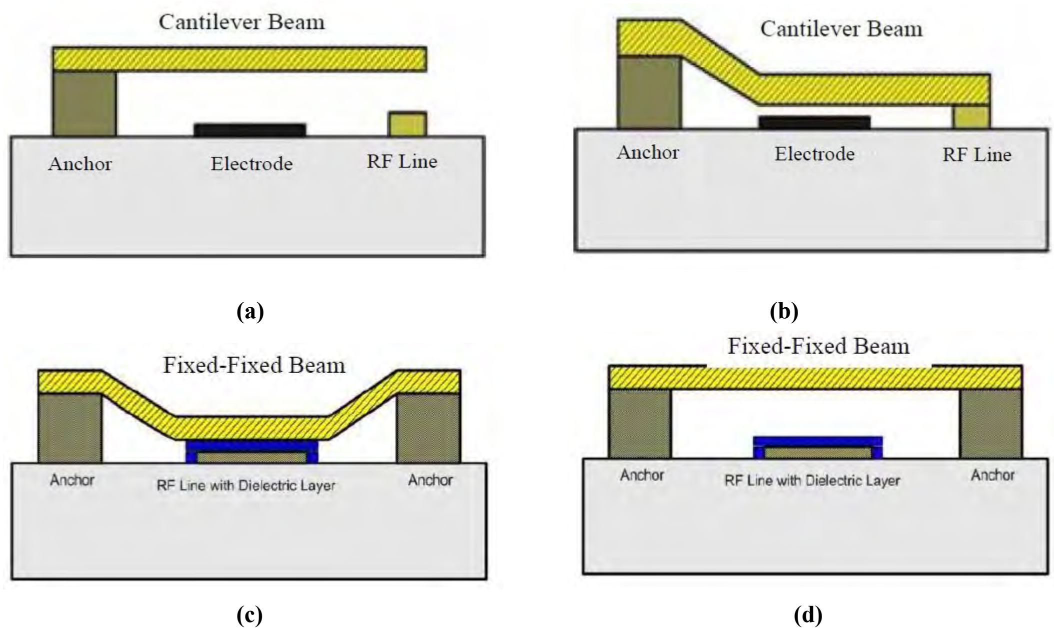

Figure 2.7. Schematic view of cantilever type RF MEMS switch (a) OFF state (b) ON state and fixed-fixed type switch (c) OFF state (d) ON state

The last type of grouping is the beam location. Again, this is a unique switch classification used only in mechanical switches. This type uses the beam location or direction relative to the single path. If the switch is in the same direction of the signal path, it is called an inline switch. If the direction is perpendicular, it is called a broadside switch.

2.5.2. ELECTROSTATIC ACTUATION RF MEMS SWITCHES

Up to date, electrostatic actuation is the most used and well established technique. This type of switches have relatively simple fabrication processes and spend nearly zero DC power. A good number of works has been reported on the development of electrostatic actuation RF MEMS switches [22, 26]. The most common type of electrostatic MEMS switch is of cantilever type. It has a vertical movement, metal-to-metal contact with series circuit configuration. A typical example is the Northeastern University MEMS switch developed by the Northeastern University and the Analog Devices [27]. This switch has a thick electroplated gold cantilever of 7 - 9 μm and 75 μm long by 25 - 30 μm wide beam dimension. The beam is suspended 0.6 - 1.2 μm above the pull-down electrode as shown in figure 2.8. Due to the thick and short beam design, the cantilever has a very high spring constant of greater than 100 N/m. The cantilever does not touch the electrode when the switch is actuated due to stiffness. As the result, no dielectric is needed for isolating the beam and the electrode.

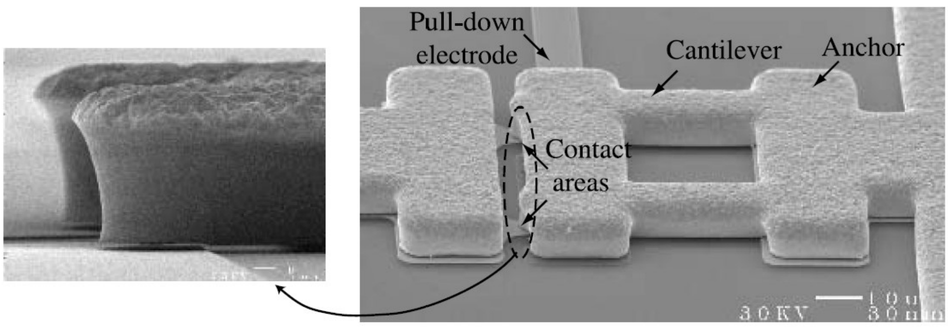

Figure 2.8. SEM of The Northeastern University MEMS inline DC-contact series switch

The Lincoln laboratory inline DC-contact MEMS series switch is presented in figure 2.9 [28]. This switch features a curled cantilever arm with the purpose to increase the isolation when the switch is at the OFF state. In order to reduce the coupling in the electrode, it is fabricated using very high resistance material. Due to the large gap between the contacts (10 - 15 μm), this switch gives a very high off state isolation. Also because of the curled beam, the switch has a very small dimension. This switch has a reported actuation voltage of 80 V. It offers a very fast switching time of less than 1 μs thanks to the small size (50 x 50 μm^2) and large actuation voltage.

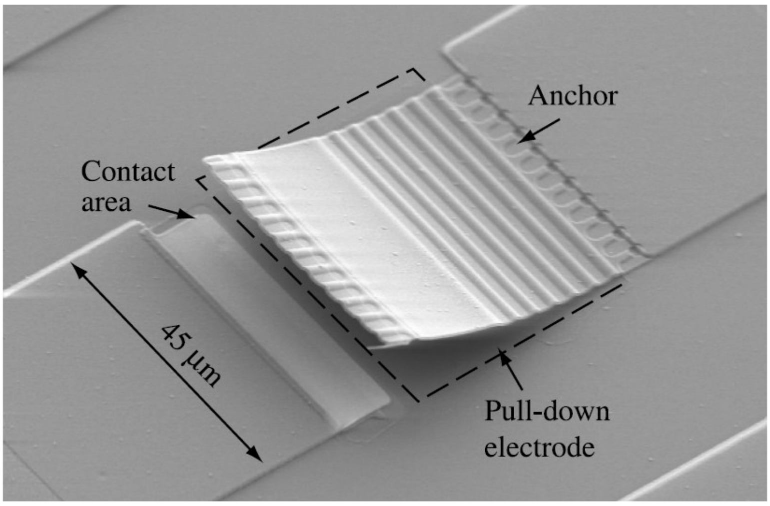

Figure 2.9. SEM of Lincoln Laboratory inline DC-contact MEMS series switch

Fixed-fixed beams are also widely employed in RF MEMS switches. A good example is the Rockwell Scientific DC-contact MEMS series switch as shown in figure 2.10 [29]. The switch is fabricated on GaAs substrate by surface micromachining and has a membrane that is connected to the substrate on four anchor points through a folded cantilever arms. The membrane is a 1 - 2 μm silicon dioxide layer. The top electrodes are two thin gold rectangles that are fabricated over this membrane. Micro-sized holes are distributed across the membrane to release sacrificial layer as well as to reduce film damping. Pull-down electrodes are located right under the top electrodes. The entire switch is suspended 2 – 2.5 μm above the substrate. Two pairs of metal contacts are placed under the membrane right above the opened transmission line as shown

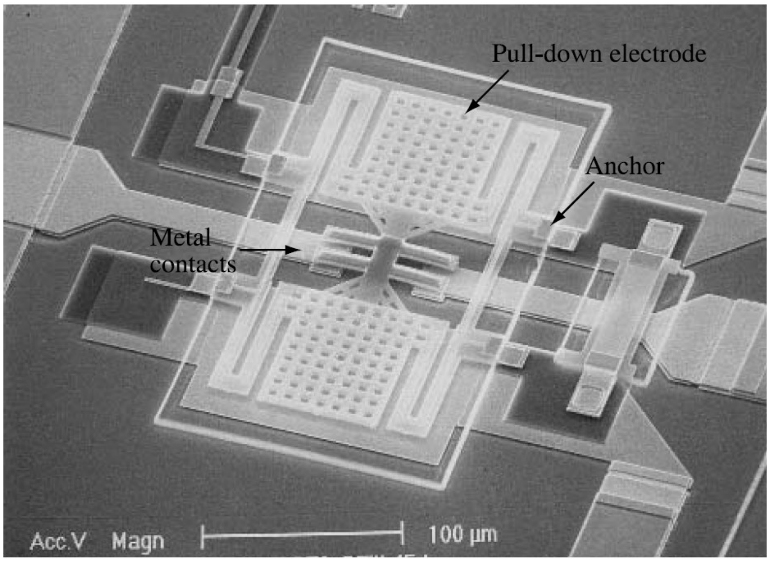

Figure 2.10. SEM of the Rockwell Scientific MEMS series switch [29].

While the most dominate electrostatic MEMS switches are designed to be inline, a number of publications are reported with a broadside configuration [30-34]. One good example is the Hughes Research Laboratories series MEMS switch as shown in figure 2.11 [32]. As can be seen in the photo, instead of an inline configuration, the switch is aligned to the broadside. This switch initiate a three layer beam as shown in figure 2.11 (b). The top electrode consist of an electroplated gold layer of 2.2 - 2.5 μm thick sandwiched by two silicon nitride layers. The two nitride layers are used to isolate the top electrode from contacting the bottom electrode and for stress balance purposes. The tip of the cantilever consists of gold-alloy contacts. When the switch is actuated, the contacts complete the transmission line and allow RF signal to pass. In general, broadside switches have larger dimensions than inline counterparts. But for the longer beams and larger actuation areas, they can offer much smaller actuation voltage. Although the switching speed suffers. In the case of the HRL DC-contact MEMS series switch, the report actuation voltage is 30 - 40 V and the switching speed is only 30 μs.

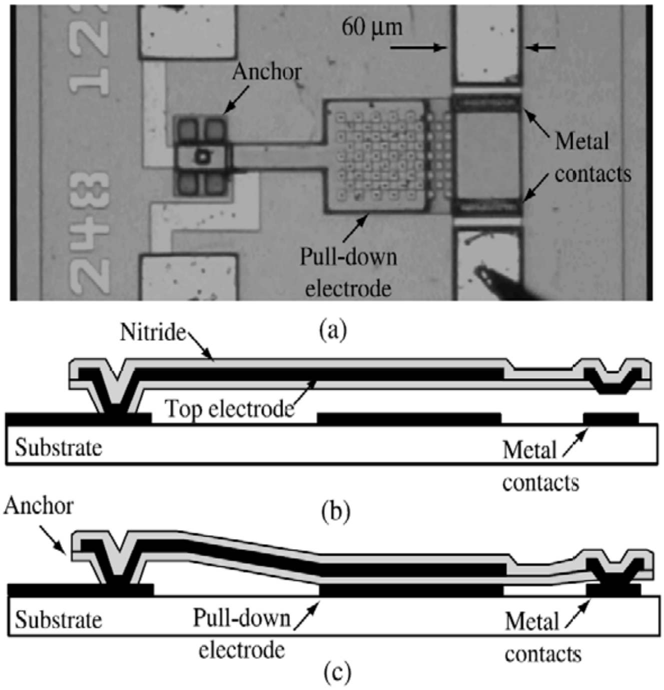

Figure 2.11. (a) SEM of HRL MEMS switch and (b), (c) cross section of the switch [32].

To further reduce the actuation voltage, the push-pull technique (also called the seesaw configuration) is introduced to fabricate RF MEMS switches [33-34]. Figure 2.12 shows two MEMS switches using the push-pull technique with two actuation electrodes. In the example demonstrated by Hah in [33], a push pull switch is reported to have pull-down voltage of 3 - 14 V.

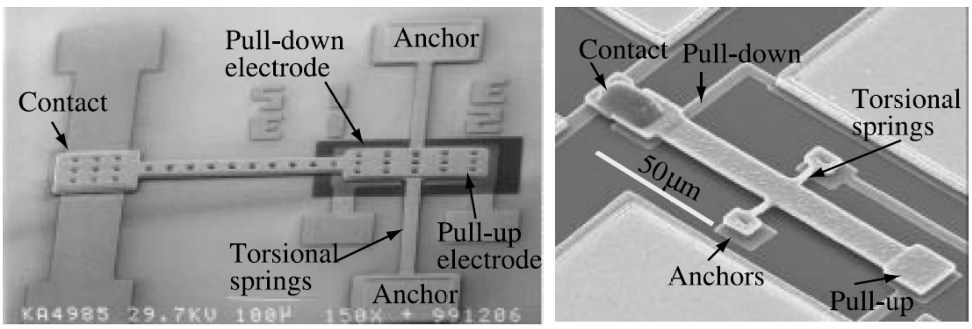

(a) **(b)**

Figure 2.12. SEM photos of push-pull MEMS series switches reported by (a) Hah [33] and (b) Chiao [34].

Although most of RF-MEMS switches have a beam fixed to the substrate with at least one anchor, the switch reported in [35] has a freely move beam. This is beneficial to the actuation voltage because the beam does not have to overcome elastic deformation during actuation whereas one end fixed switches have. Therefore, a freely movable beam only requires an electrostatic force to overcome the gravitational and fractional forces. As figure 2.13 shows, when voltage is applied between the electrode and the movable contact pad, the contact pad can move vertically without experiencing deformation. As a result, this switch achieved a very low actuation voltage of 5 V which is compatible with CMOS IC technology unlike most other RF MEMS switches where a voltage converter is a necessity. Also, thanks to the freely movable beam, the switching speed is very high. The reported switch speed is 0.12 μs and 0.13 μs for turning the switch on and off respectively.

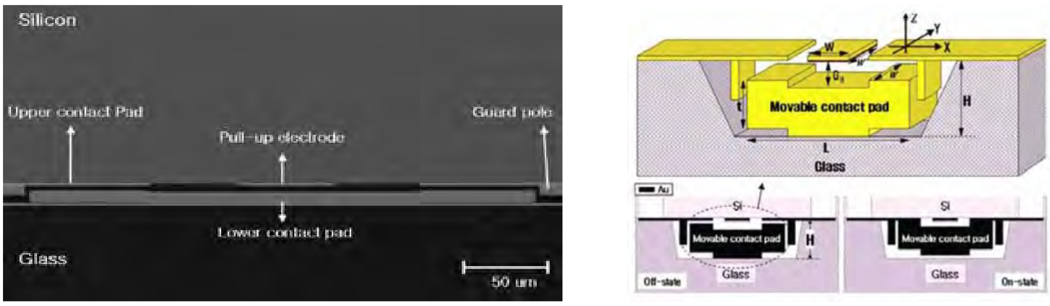

(a) **(b)**

Figure 2.13. (a) SEM photo and (b) 3D model of the freely move RF MEMS switch [35].

Other than series switches, capacitive type switches or shunt switches also important type of MEMS switches. As mentioned previously, a series switch is used to open or short input and output ports by disconnecting or connecting transmission lines respectively. Shunt switch is used to either pass RF signal between input and output ports or short it to ground. Both of them are best suited in different frequency range. The most well-known shunt switches: Texas Instruments switch, the Raytheon shunt switch and the University of Michigan low-voltage MEMS shunt switch are shown in figure 2.14 [36-37].

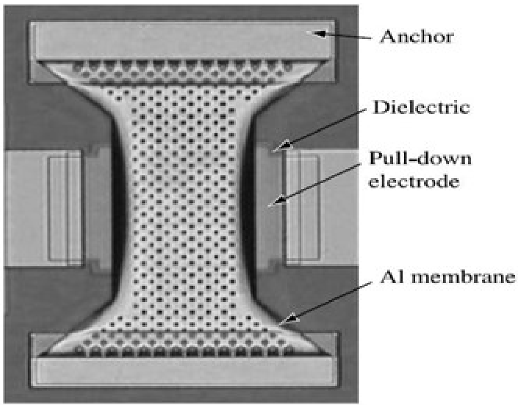

(a)

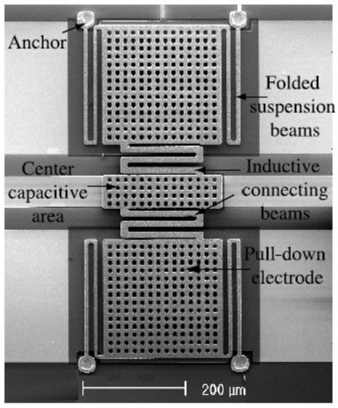

(b)

Figure 2.14. SEM photos of (a) Raytheon MEMS capacitive shunt switch [36] and (b) the University of Michigan low-voltage MEMS shunt switch [37].

2.5.3. THERMAL ACTUATION BASED RF MEMS SWITCHES

Electrostatic RF MEMS switches are easy to fabricate and consume virtually zero DC power. However, to achieve large displacement; researchers are also working on the thermally actuated RF MEMS switches. Thermal expansion amplification is the mechanism for thermal actuation RF MEMS switches generate motion. A small amount of thermal expansion in one part of the device leads to a larger amount of expansion in whole device. Beside their advantages, thermally actuated RF MEMS switches are not commonly used in many applications because of their higher DC power consumption. Most reported thermally actuated RF MEMS devices are fabricated using the MUMPs fabrication process provided by the MEMSCap [38].

Different types of thermal actuators have been fabricated. Figure 2.15 shows a V-shaped thermal actuator fabricated by Sandia Labs [39]. The V-shape thermal actuators are commonly referred as "chevron" or "bent-beam" thermal actuators. These thermal actuators are mostly used in applications requiring high force and reliability. The switch actuated when current is passing through the legs of the actuator. The current can generate Joule heat on these legs which lead to a constrained thermal expansion. This results in motion of the center shuttle as shown by the arrow in the figure 2.15.

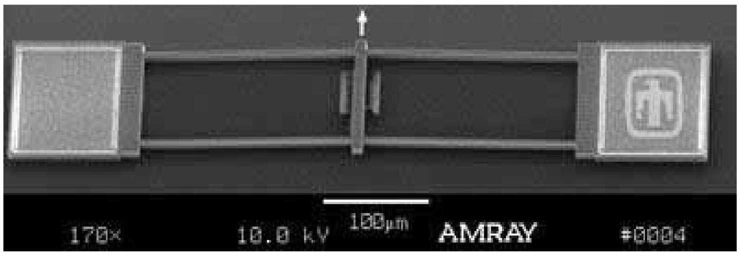

Figure 2.15. V-shaped thermal actuator for on-chip in-plane high-force linear-motion actuation [39]

A number of bent beam thermal actuation based RF MEMS switches have been presented in [40-42]. Figure 2.16 shows the buckled beam thermally actuated RF MEMS switch developed by UPC Barcelona Tech. Spain [40]. The switch was fabricated by using PolyMUMPs process and contains a resistive beam anchored at both ends. The beam have a bend in the center making thermal expansion stresses applied in the angled direction. The amount of deflection depends on the level of power applied.

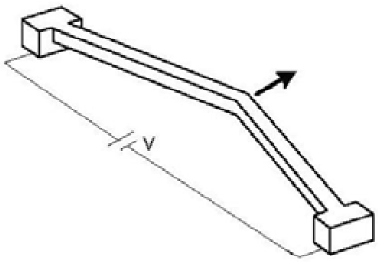

(a)

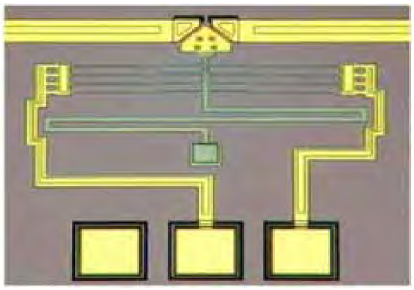

(b)

Figure 2.16. The buckle-beam thermal MEMS switch from UPC-Barcelona Tech. (a) schematic layout indicate the motion and (b) SEM photo of series switch

A bent beam electro thermal actuator developed by University of Wisconsin, USA [41]. The cascaded thermal actuators were fabricated by depositing three materials: polysilicon, Ni plated beam and boron doped single crystal silicon beam. The thermal actuators achieved a static displacement of 10µm with a power dissipation of 100mW.

As an alternative to high DC power consumption, the University of Alberta developed thermally actuated latching RF MEMS switch is shown in Figure 2.17 [42]. The device was fabricated using metal MUMPs process. Two thermal actuators were used in this design connecting to two separated center conductors of CPW transmission lines. The switch operates with short pulses of either low voltage or low current, remaining in steady state with zero DC power consumption. However, due to the intrinsic property of thermal actuators as they require time to heat up and expansion, they cannot be used when high switching speed is necessary. In general, thermal actuators can only operate with millisecond switching speed. In the latching mechanism where multiple operations are needed, switching speed could increase to seconds which greatly restrict its use in selected applications.

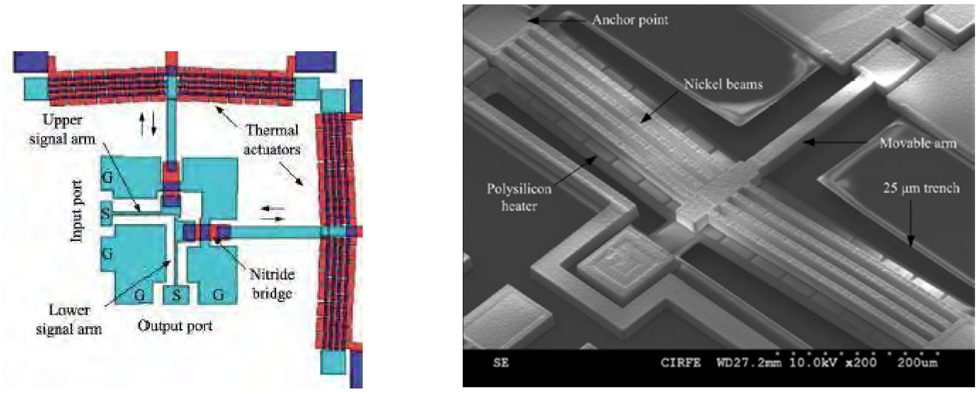

(a) (b)

Fig. 2.17. (a) Schematic layout (b) SEM photo of University of Alberta thermal actuation latching MEMS switch [42]

2.5.4. MAGNETIC ACTUATION BASED RF MEMS SWITCHES

Magnetic actuation based RF MEMS is a MEMS device that bases on magnetic actuators. Generally permanent external magnetic field or permalloy materials are necessary. There are limited publications related to this topic including the Jiaotong University bi-stable MEMS switch and the Korea Advanced Institute of Science and Technology KAIST RF MEMS switch actuated by combination of electromagnetic and electrostatic forces [43]. Figure 2.18 shows the Jiaotong University bi-stable MEMS switch. The switch is built based on CPW transmission line structure. The actuator consists of a beam fixed at the center by torsional springs with permanent magnets and the coils for magnetic actuation. Different magnetic forces are generated according to the current flowing in coil. The cantilever is then moved from one stable state to another. Due to the necessity of a permanent magnet, fabrication is complex and stress in different layers has to be taken good care of. Because of the complexity of the fabricated, no mechanical and RF performance results are reported to date.

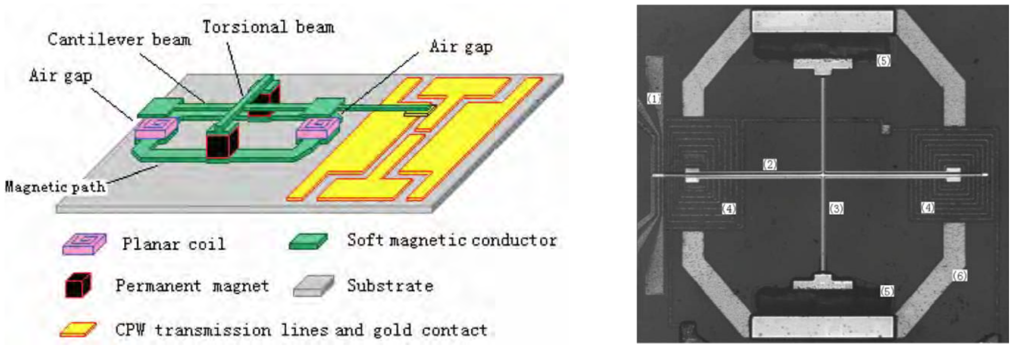

(a) **(b)**

Fig. 2.18. (a) Schematic layout and (b) SEM photo of Jiaotong University bi-stable MEMS switch [43]

The KAIST RF MEMS switch is a more mature design where external magnetic field is used instead of using fabricated permanent magnet on chip [44]. Like the Jiaotong University's design, coils are employed to generate magnetic fields to interact with the external field to result in a magnetic force. Instead of the bi-stable design demonstrated, this design shown in figure 2.19 used electrostatic force to hold the switch in position. A voltage of 2 V with 53 mA current for magnetic actuation and a hold voltage of 3.7 V for electrostatic actuation is reported. This switch demonstrates the capability of lowering applied voltage by combining of electromagnetic and electrostatic actuation mechanism. The only shortcoming of this design is the actuation speed. The reported switching time is 380 μs which is much higher than electrostatic actuation alone.

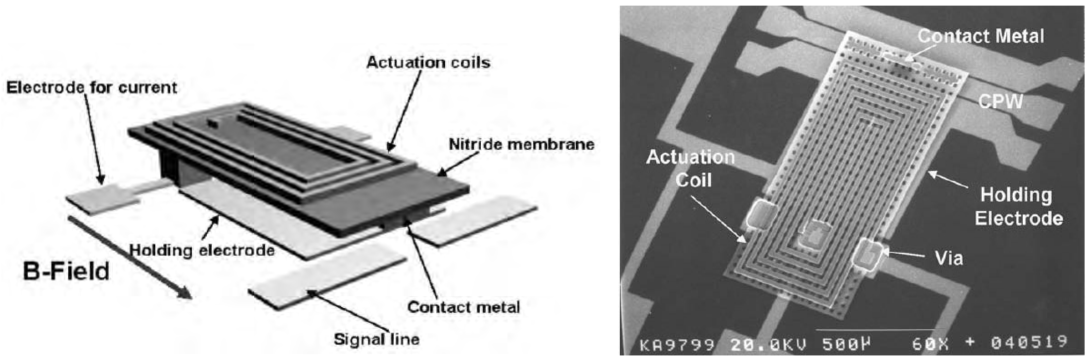

(a) **(b)**

Fig. 2.19. (a) Schematic layout and (b) SEM photo of KAIST RF MEMS switch [44]

University of Michigan reported a push pull SPDT switch design after above two [45]. The switch actuates by the electromagnetic force and holds its position by electrostatic force. The actuation was done by using the external magnetic field. As can be seen in figure 2.20, the switch structure composes of only one symmetric membrane and it rotated along a torsion bar which always connected one of the output ports to the input port. Small amount of power is consumed only during the electromagnetic actuation for a short time. While in holding position the switch utilizes electrostatic mode which consumed negligible power. The switch was fabricated on glass substrate with electroplated Au layers. The switch reported actuation voltage was less than 4.3V with a 166 million life cycle.

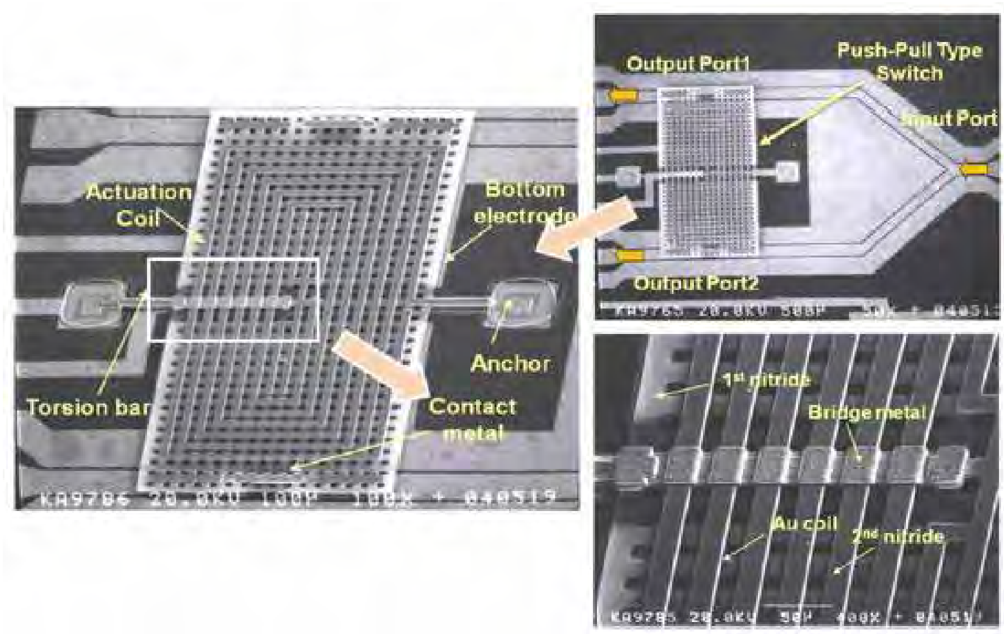

Figure 2.20. SEM photo of SPDT RF MEMS switch fabricated by University of Michigan [45]

2.5.5. PIEZOELECTRIC ACTUATION BASED RF MEMS SWITCHES

Piezoelectric actuators make use of the piezoelectric effect in materials that exhibit piezoelectricity. Piezoelectric effect is a phenomenon in which an electric field or electric potential is generated when materials experience stress. In piezoelectric actuator, the reverse piezoelectric effect is used where stress is controlled by applied voltage. Piezoelectric actuation generally requires very small voltage (typically below 5 V) compared to electrostatic actuation. It also does not inherent the charging effects in electrostatic designs. However, there is very limited work reported on RF MEMS using piezoelectric actuator, due to the difficulty and complexity of fabricating piezoelectric materials. Some reported papers include the LG piezoelectrically actuated DC-contact series switch [46] and the piezoelectric switch reported by Polcawich et al. in [47] as shown in figure 2.21.

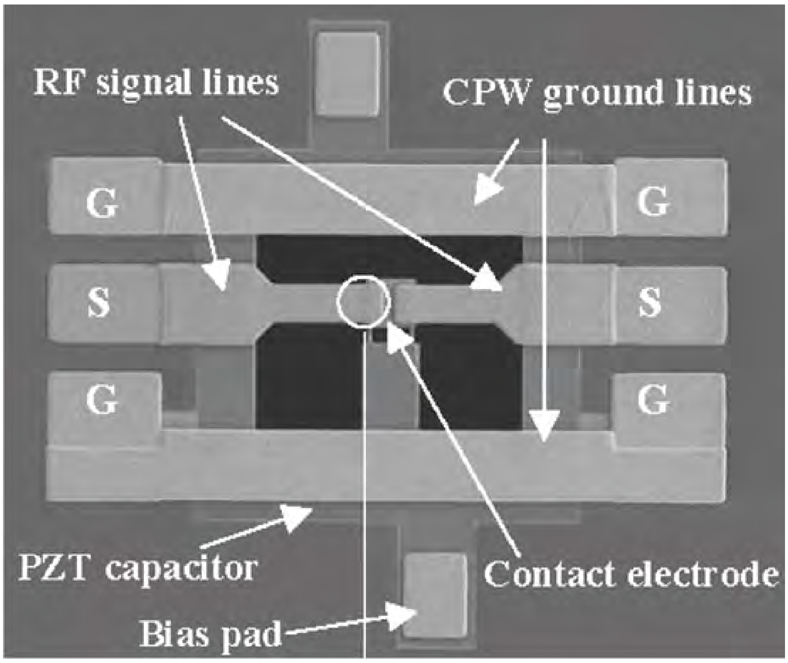

(a)

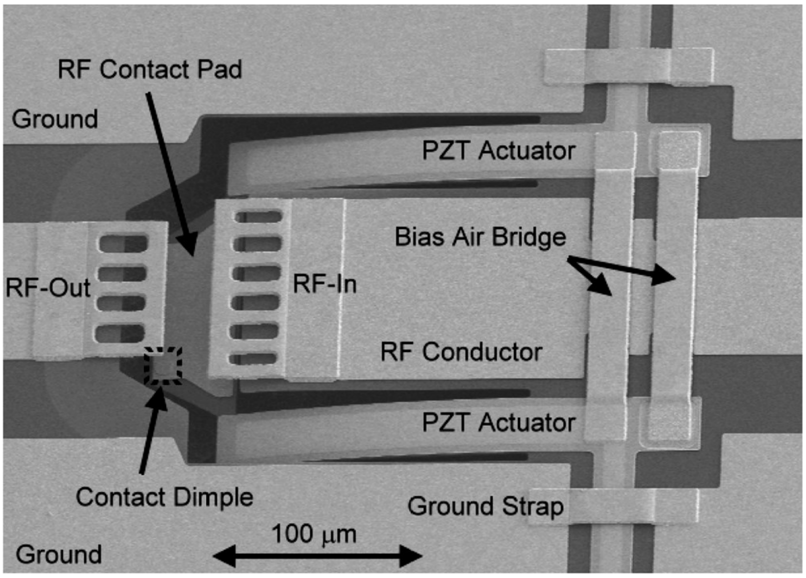

(b)

Figure 2.21. Piezoelectric actuation RF MEMS switch developed by (a) LG [46] and (b) by Polcawich et. al [47]

Both switches were fabricated with very similar fabrication techniques, where both surface and bulk micromachining were used. Both switches had their beams fabricated under a gap between input and output of transmission line. The major difference between the two designs was the use of elastic layers to introduce stress on the beams. The reported actuation voltage is as low as 2.5V while achieved a comparable RF performance to electrostatic MEMS switches. The piezoelectric actuation mechanism seems ideal, but it has its own problems. Thermal instability and oscillation during actuation remain as key challenges. Also the piezoelectric film has aging problems [48-49] which could be a major problem when lifetime is important.

2.6. RF MEMS PHASE SHIFTER

Phase shifter is an essential component found in microwave and millimeter-wave communication, radar and phased array antennas. The main reason why conventional MMIC technology is used was because of the demand to miniaturize phase shifters so that they could be easily integrated into compact phased array antenna systems. Currently, the phase shifters are based on PIN diodes, ferrite materials or FET switches. The advantage of PIN diode phase shifters is that they provides low loss in the device, but consume more power than FET switches. The FET-based shifter can be built on the same substrate with the amplifiers, thereby reducing the assembly cost. The ferrite device can handle high RF power while offering excellent performance, but they are very expensive to fabricate and consume a relatively high DC power than the other two types of phase shifter. So that the role of MEMS switches in phase shifter designs can be immediately seen. MEMS switches result in considerable reduction in the DC power and lower loss. Since MEMS switches can be fabricated directly with antenna on ceramic, quartz or silicon wafers, they lead to a low cost phased array [26].

There are many different technologies that can be used to implement a phase shifter such as switched-line, reflection topology, loaded-line, and switched-filter [50]. Switch line type is one of the easiest way to implement a digital phase shifter, which have one or more cascaded stages of switched delay lines, with two switches per stage. Reflection topology have a one or more cascaded directional couplers, reflection terminations with either lumped- or distributed-elements and single-pole multiple-throw switches, so this type of phase shifter has a relatively small operation bandwidth. Loaded line shifter is to load a transmission line with two different capacitive membrane SPST switches for phase delay and always use a midsection matching network, this topology have excellent performance for small phase delay. Switched filter type phase shifter has cascaded stages of low-pass and high-pass filters that are switched using either two SPDT switches per stage or a DPDT switch between stages.

2.6.1. RF MEMS SWITCHED-LINE PHASE SHIFTER

A flurry of papers on RF MEMS digital switched delay line shifter has been reported. Hayden et al. reported a 2- and 3-bit distributed phase shifter constructed based on coplanar waveguide [51]. The design uses distributed MEMS transmission line loaded with high capacitance varactors which are fabricated using a series combination of MEMS bridges and fixed value metal-insulator-metal (MIM) capacitors. The fabricated device achieved a true time delay from 1 to 10 GHz with a reflection coefficient smaller than -15 dB and a 180 degree per dB of insertion loss at 8-10 GHz. One advantage of this design is the performance of the device is relatively insensitive to the MEMS capacitance ratio and the fabrication procedure. Tan et al. demonstrated a 2-bit and 4-bit true time delay networks fabricated on 8 mil GaAs substrate [52]. This semi-lumped approach employing microstrip transmission line and MIM capacitors for both reduce circuit size and avoid the high insertion loss found in typical structures. The 2-bit phase shifter has an average insertion loss of 0.7 dB at 9.45 GHz with an associated phase error of ±1.3°. This shifter measured to work over 6 - 14 GHz with a return loss better than 14 dB. Borgioli et al. reported a 1-bit K-band distributed low loss MEMS phase shifter [53]. Again, MEMS capacitive membrane switches were used, with having an actuation voltage of 75 V. An 8.6 mm long CPW line on a glass substrate achieved a DC to 35 GHz bandwidth, with a relative phase shift and insertion loss of 270° and 1.7 dB, respectively, at 35 GHz. Due to the variation in the characteristic impedance of the CPW line, from 66 Ω in the OFF state to 38 Ω in the ON state, the inherent impedance mismatching creates unwanted ripples in all the frequency responses. The same team then went on to report a 3-bit distributed delay line shifter using the same transmission line topology, substrate and MEMS switches [54]. Lakshminarayanan et al. reported a true time delay MEMS phase shifter comprised of impedance-matched slow wave unit cell [55]. The MEM beams are actuated using high resistance SiCr bias lines with typical actuation voltage around 30 - 45 V. The measured results show a maximum phase deviation of 3% with the reflection coefficient less than 19 dB from 1 to 110 GHz. The worst insertion loss is 0.9 dB for 12 GHz, 1.16 dB for 50 GHz and 2.65 dB for 110 GHz.

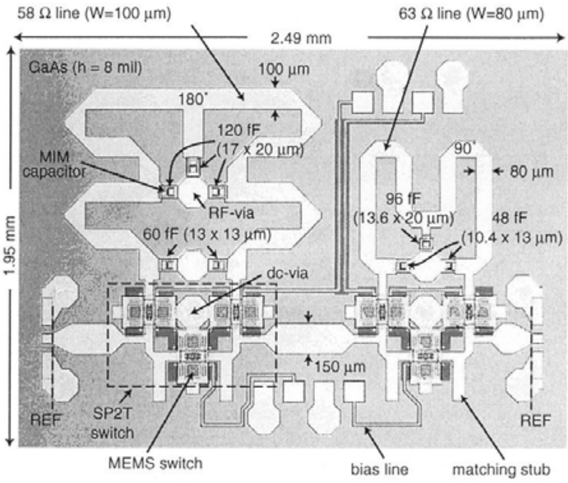

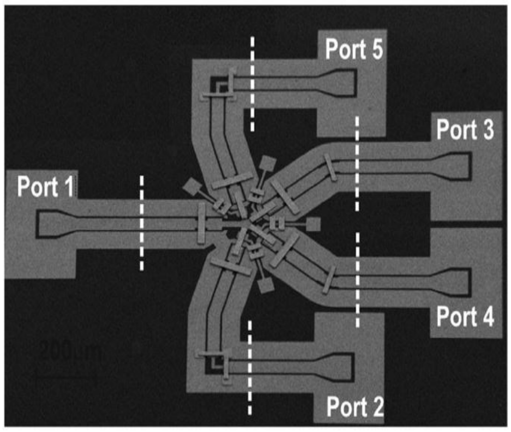

[56] [57]

Figure 2.22. RF MEMS based switched-line type phase shifters

2.6.2. RF MEMS REFLECTION-TYPE PHASE SHIFTER

Park et al. has reported a V-band 2- and 3-bit reflection-type phase shifter, with micromachined coplanar waveguide coupler and switches [58]. The microfabricated air-gap overlay coupler and the direct contact series switches were employed to reduce the insertion loss. The measured results show a relatively small phase error, but the insertion loss and the return loss are 4.1 dB and 11.7 dB, respectively, at 50 to 70 GHz. The 3-bit phase shifter (shown in figure 2.23 (b)) is realized by cascading the 2-bit phase shifter and a 180° phase shifter, the size of the 3-bit shifter is 3.2 mm ×2.1 mm. In the next year, this team continued to report a 5 - 17 GHz wideband phase shifter using capacitive MEMS switches [59]. The micromachined reflection-type shifter have an average insertion loss of 3.48 dB and maximum phase error of ±1.8° over the operation bandwidth. From the measured diagrams, the shifter has a flat phase response over the required spectrum which is essential for wireless communication applications. Malczewski et al. also reported a two-stage 2-bit reflection-type delay line shown in figure 2.23 (c), using tapped delay line reflection terminations. At X-band, the measured insertion loss was around 1.5 dB, with 60% of this loss being attributed to the Lange directional couplers [60].

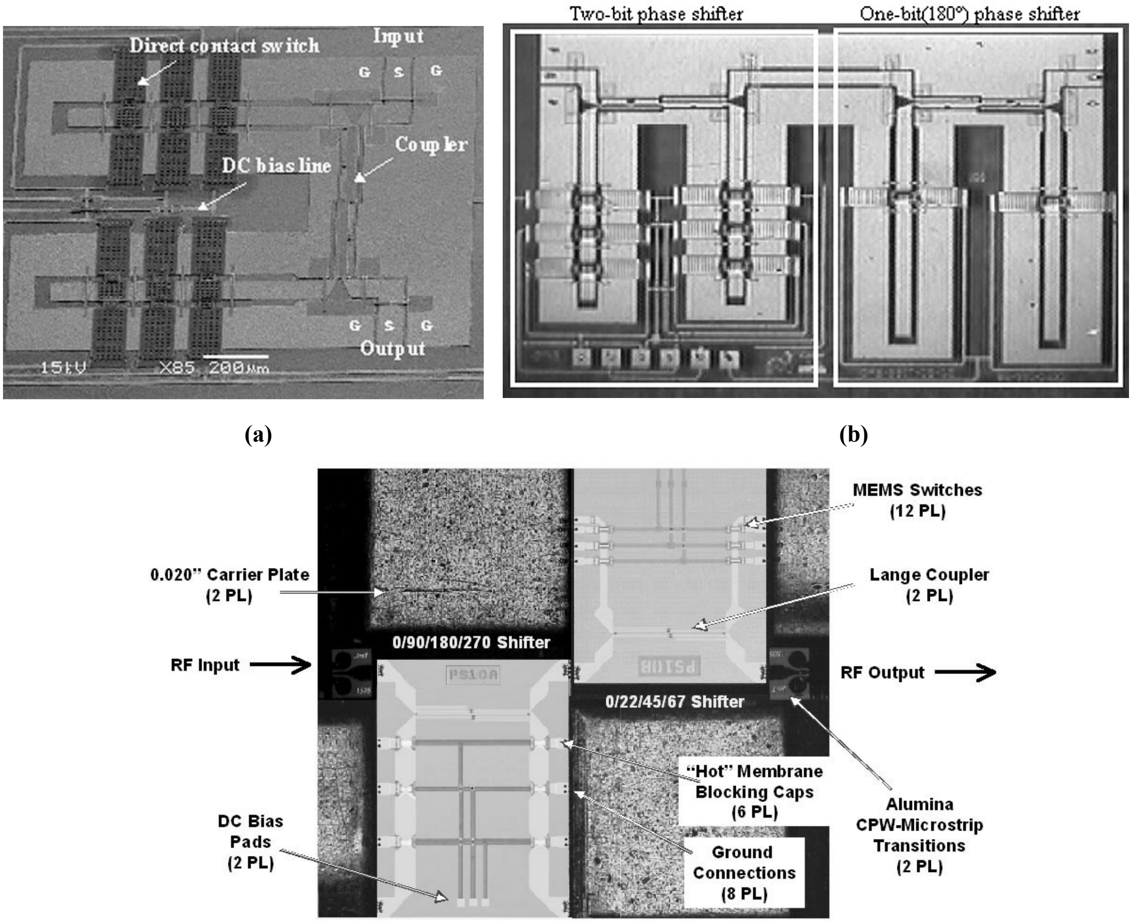

(c)

Figure 2.23. MEMS based reflection-type phase shifters (a) 2-bit (b) 3-bit by Park et al. [59] (c) by Malczewski et al. [60]

2.6.3. RF MEMS DISTRIBUTED LOADED-LINE PHASE SHIFTER

MEMS distributed loaded-line based shifters have also been reported. By applying a single bias voltage to either the signal conductor of the coplanar waveguide (CPW) line or the MEMS bridges lying over this center conductor, the effective distributed capacitance of the line can be changed, which in turn changes the phase velocity and, thus, the associated propagation delay through the transmission line. Using this principle, Barker and Rebeiz reported a true time wideband loaded-line phase shifter with MEMS switches [61]. The device is fabricated on a 500 μm quartz substrate with fixed-fixed beam MEMS bridge capacitors located periodically over the CPW transmission line, thus creating a slow-wave structure. A single analog control voltage is applied to CPW center conductor for changing the phase velocity. This design demonstrates a DC to 60 GHz phase shifter with 2 dB loss per 118° at 60 GHz and 1.8 dB loss per 84° at 40 GHz. A high isolation of 40 dB is found in switches from 21 to 60 GHz. The same team went on to demonstrate a 2-bit implementation at X-band [62]. MAM capacitors have replaced MIM switches with Kim et al. [63] demonstrating a 4-bit 40 to 70GHz implementation, but suffering from high insertion loss, and later Hayden and Rebeiz [64] reported a DC to 37GHz version.

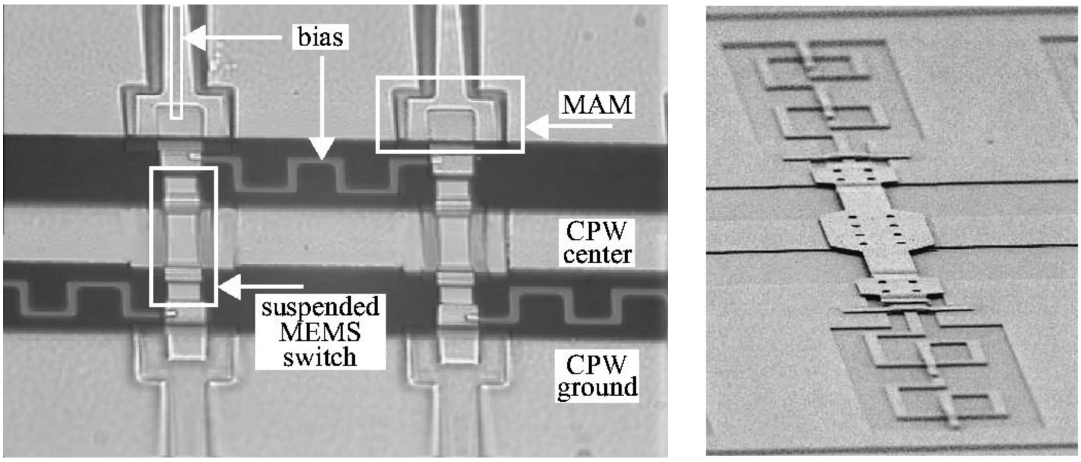

(a) **(b)**

Figure 2.24. MEMS based reflection-type phase shifters (a) by Kim et al. [63] (c) by Hayden and Rebeiz [64]

2.7. SPECTRUM ALLOCATED AT 60 GHz

In 2001, the Federal Communications Commission (FCC) allocated a bandwidth of 7 GHz between 57–64 GHz for unlicensed use. This is certainly unprecedented when it compares to less than 0.5 GHz of a spectrum approved between 2 to 6 GHz for Wi-Fi and other license-free applications. It has unique operational advantages that overweigh traditional 2.4GHz or 5GHz license-free radios and licensed-band millimeter-wave radios. Thus, it is attractive for various devices requiring high data transmit speed [65]. For the first time, multi-gigabit wireless links were made possible thanks to a sufficient spectrum. Therefore, a considerable effort has been made since then to the development of wireless communication systems working in the frequency band centered at 60 GHz [66].

Signals at 60 GHz are strongly attenuated by oxygen. This property greatly limits the coverage of 60 GHz links but offers advantages in terms of interference reduction and security enhancement over other wireless systems. 60 GHz antennas are intended to be used in small cells so the oxygen absorption can help to confine the radiation inside the cells. This property isolate one cell from another which indicates that it can limit the noise from adjacent cells and secure the transmitted data from detecting by devices outside the intended area.

2.8. RECONFIGURABLE ANTENNAS

Antennas are necessary and critical components of wireless communication and radar systems. Arguably, there are nine different types of antennas have proliferated during the past 50 years. They are dipoles/monopoles, loop antennas, slot/horn antennas, reflector antennas, microstrip antennas, log periodic antennas, helical antennas, dielectric/lens antennas, and frequency-independent antennas. Each type possesses inherent benefits and drawbacks that make them more or less suitable for particular applications. When faced with a new system design, engineers modify and adapt these basic antennas, using theoretical knowledge and general design guidelines as starting points to develop new structures that often produce acceptable results.

Nevertheless, the choice of an antenna from the families mentioned above imposes restrictions on the overall system performance because the antenna characteristics are fixed. Making antennas reconfigurable so that their behavior can adapt with changing system requirements or environmental conditions can improve or eliminate these restrictions and provide additional levels of functionality for any system.

Ideally, reconfigurable antennas should be able to alter their operating frequencies, impedance bandwidths, polarizations, and radiation patterns independently to accommodate changing environment. However, the development of these antennas poses significant challenges to both antenna and system designers. These challenges lie not only in obtaining the desired levels of antenna functionality but also in integrating this functionality into complete systems to achieve efficient and cost-effective solutions.

2.8.1. FREQUENCY RECONFIGURABLE ANTENNAS

Frequency reconfigurable antennas (also called frequency tunable antennas) can be classified into two categories: switched and continuous. Switched antennas use certain kind of switching mechanism to operate at separated frequency bands. Continuous reconfigurable antennas, on the other hand, allow for smooth transitions within or between operating bands without jumps.

Many common antennas including linear antennas, loop antennas, slot antennas, and microstrip antennas, are usually operated in resonance. In other words, the effective electrical length of these antennas dominate the operating spectrum, its associated bandwidth, and the current distribution on the antenna that dictates its radiation pattern. There are different reconfiguration mechanisms to achieve frequency reconfigurability such as: switches-employed, variable reactive loading, structural/mechanical change, and material changes.

2.8.1.1. SWITCHES

The designers can change the effective length of the antenna, and hence its operating frequency, by adding or removing part of the antenna length through electronic, optical, mechanical, or other means. Groups have demonstrated different kinds of switching technology, such as optical switches, PIN diodes, FETs, and RF MEMS switches, in frequency reconfigurable monopole and dipole antennas for various frequency bands. For instance, Panagamuwa et al. presented a balanced dipole fabricated on high-resistivity silicon was equipped with two silicon photo-conducting switches, as shown in figure 2.25 [67]. Light from infrared laser diodes guided with fiber-optic cables was used to control the switches. With both switches closed, the antenna operated at a lower frequency of 2.16 GHz, and with both switches open, the antenna operated at 3.15 GHz. The researchers also note variability in antenna gain as a function of the optical power used to activate the switches. A similar design approach was taken by Freeman et al. to change the effective length of a monopole antenna using optical switches, which helped to eliminate some bias line effects that can occur with other kinds of switches [68]. Kiriazi et al. present a similar example of antenna length changes using RF-MEMS switches in [69]. In this work, a simple dipole antenna was printed on a high-resistivity silicon substrate. By turning ON and OFF a pair of RF MEMS switches integrated on the dipole antenna, the antenna can work in one of two frequency bands.

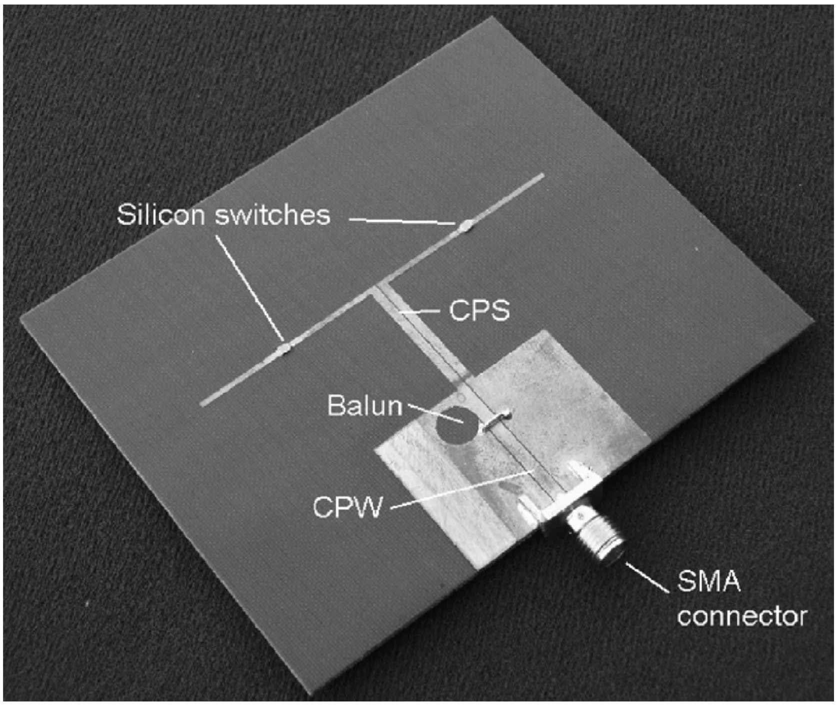

Figure 2.25. Photograph of an optically switched dipole antenna that provides frequency reconfigurability [67]

Using four PIN diodes, Roscoe et al. developed a reconfigurable printed dipole antenna to deliver three operating bands between 5.2 and 5.8 GHz [70]. Others have applied the same approach to microstrip patches [71-72], microstrip dipoles [73], and Yagi antennas [74]. Anagnostou et al. discuss a reconfigurable monopole based on a Sierpinski gasket with RF-MEMS switches to connect sections of the antenna together to provide multiple operating bands [75]. Subsequent work with direct integration of RF-MEMS switches provided three separate operating bands with similar omnidirectional radiation characteristics [76]. This direct integration of the antenna and switches on a substrate helps to eliminate the package parasitics and other nonideal effects that would be generated if the switches were prepackaged and then bonded using solder and/or bond wires.

Switched frequency-radiating slots with a variety of geometries and radiating properties have also been proposed by a number of researchers. One reconfigurable slot antenna was proposed by Gupta et al. [77]. With a nested ring layout, it was fed with a single slotline or coplanar waveguide (CPW) line. Using eight PIN diode switches, the lower of two operating frequencies was set by the perimeter of the outer loop. When shorter slot sections in two opposing sides of the loop are switched in place, the antenna operates in the upper frequency band [77]. Peroulis et al. [78] demonstrated a tunable antenna using four PIN diode switches that changed the effective length of an S-shaped slot to operate in one of four selectable frequency bands between 530 and 890 MHz. A diagram of the antenna is shown in figure 2.26.

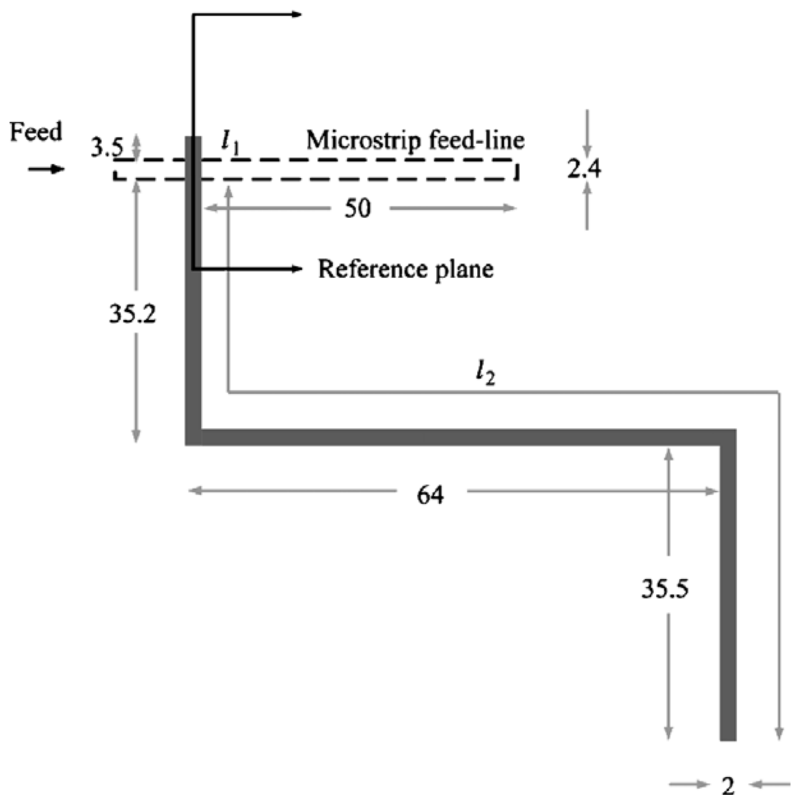

Figure 2.26. Diagram of the reconfigurable S-slot antenna with microstrip feed line. All units are in mm. [78]

Changes over such a wide-frequency band are often along with changes in input impedance; however, these investigators positioned the switches and adjusted the slot geometry such that the four frequency bands were attainable through switching alone without needing changes in the matching network or feed point position. Parasitic effects are also considered in this design. The DC bias network for each diode switch and its equivalent circuit model are shown in figure 2.27. These models were incorporated into simulations to refine the final antenna design.

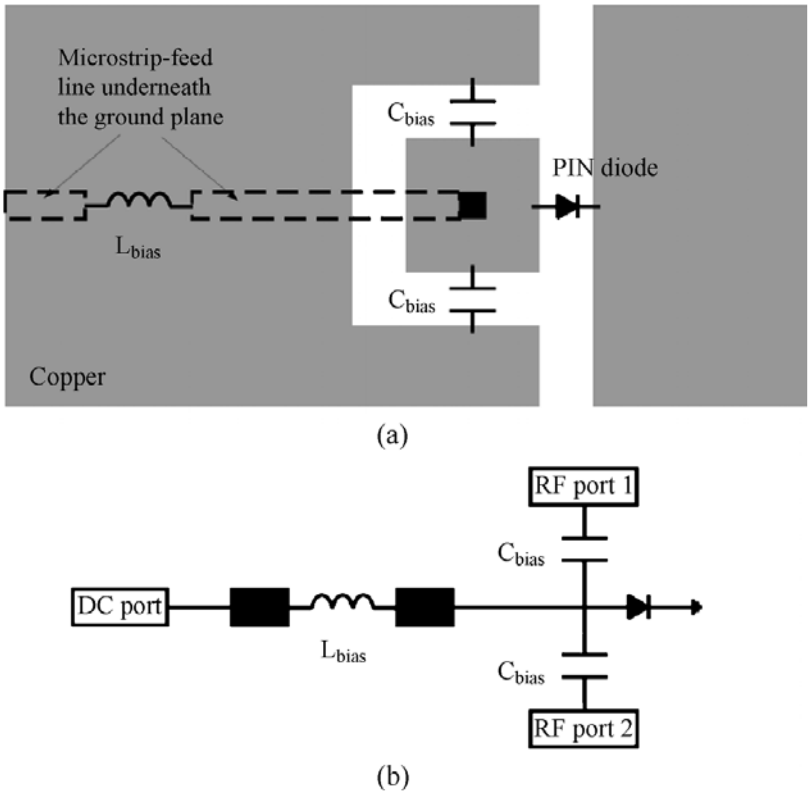

Figure 2.27. (a) Layout of PIN diode switch bias network and (b) RF equivalent circuit for bias network [78]

Another important aspect of reconfigurable antenna design is the compatibility of the antenna topology with the intended reconfiguration mechanism. In some cases, the only way to include a particular switch is to design the antenna around the switch. One such example is the hybrid folded slot/slot dipole antenna described in [79] and shown in Figure 2.28. This particular design was developed to accommodate a particular RF

MEMS switch layout to simplify the integrated fabrication and operation of the antenna.

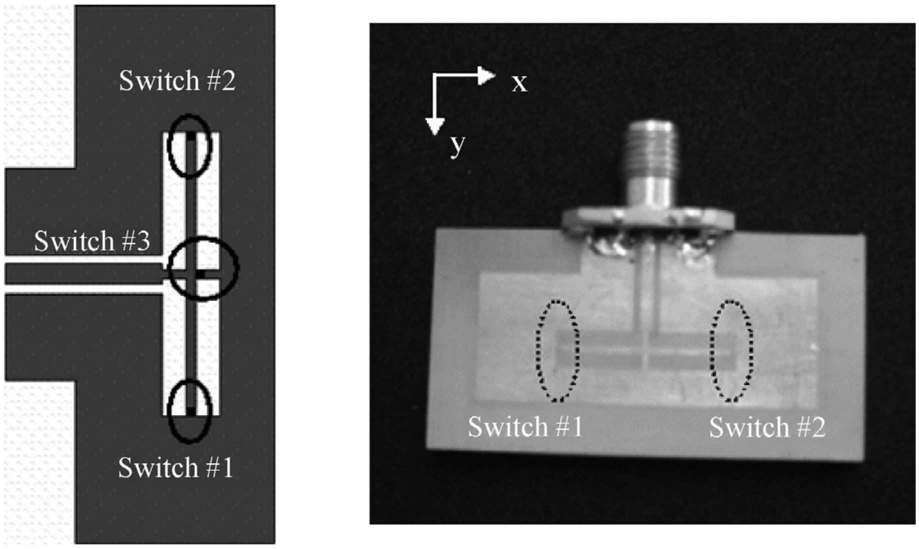

(a) **(b)**

Figure 2.28. Reconfigurable hybrid folded slot/slot dipole antenna: (a) antenna geometry including all three switches and (b) photograph of the fabricated antenna using only two of the three switches [79]

2.8.1.2. VARIABLE REACTIVE LOADING

The use of variable reactive loading is much in common with the previously discussed switch mechanism. The only real difference between the two is that, in this case, the change in effective antenna length is achieved with components that can change in a continuous range of values (typically capacitance) that allows smooth rather than discrete variation in the operating frequency band.

A one-wavelength slot antenna loaded with two one-port reactive FET components was tuned continuously in [80]. The reactances of the FETs were varied by changing the bias voltage, which in turn, changed the effective length of the slot and its operating band. The range of tuning was about 10%, centered around 10 GHz. The patterns were essentially unchanged for this relatively small tuning range. Similar reconfigurable slot antennas equipped with varactors have also been reported, which take advantage of higher order resonances to create tunable dual-band performance [81-82]. Recently, a microstrip patch antenna has been developed with integrated RF-MEMS capacitors [83]. As can be seen in figure 2.29, the capacitors are integrated on a CPW tuning stub and actuated with continuous DC bias voltages up to 12 V, which produce operating frequencies between 15.75 and 16.05 GHz. The unique monolithic approach benefits from removing the bias vias.

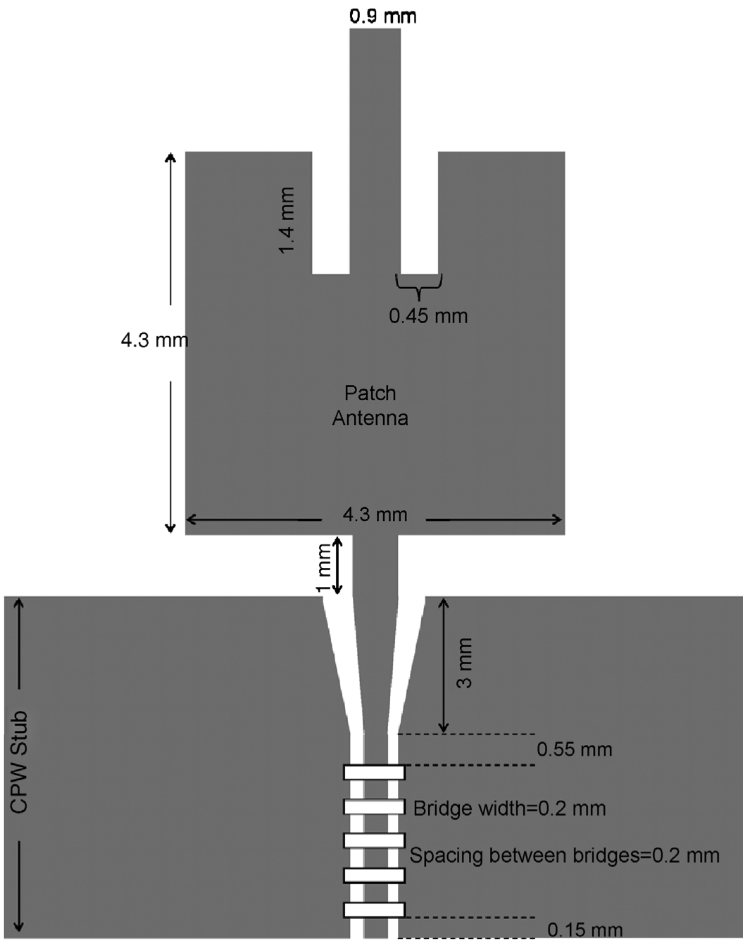

Figure 2.29. Frequency reconfigurable patch antenna with RF MEMS capacitors and CPW tuning stub. [83]

2.8.1.3. STRUCTURAL/MECHANICAL CHANGES

Mechanical rather than electrical changes in antenna structure can deliver larger frequency shifts. The main challenges lie in the physical design of the antenna, the actuation method, and the maintenance of other characteristics while significant structural changes. One example of a mechanically reconfigured antenna was demonstrated by using a piezoelectric actuator system to vary the spacing between a microstrip antenna and a parasitic radiator which leads to change of the operating band [84-86]. A picture of the antenna is shown in figure 2.30. This example illustrates the difficulty in achieving one kind of reconfigurability without incurring changes in other antenna characteristics. The bandwidth and gain of the antenna also change as a function of parasitic element spacing but cannot be individually selected.

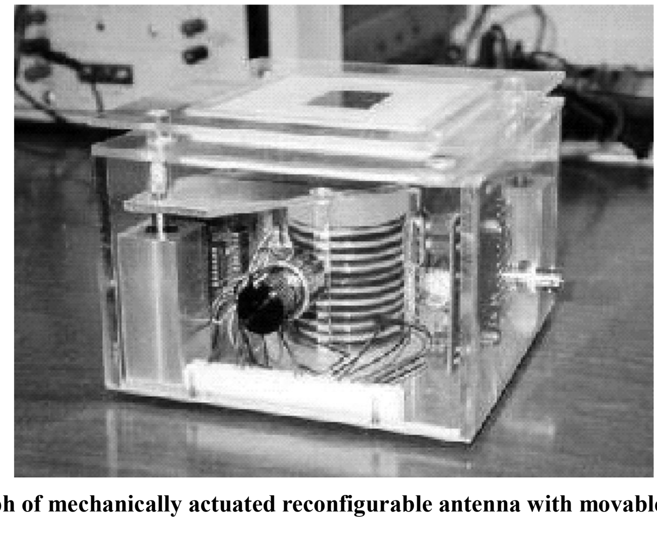

Figure 2.30. Photograph of mechanically actuated reconfigurable antenna with movable parasitic element [84]

Langer et al. designed a magnetically actuated microstrip antenna for operation around 26 GHz [87]. The antenna structure was covered with a thin layer of magnetic material and released from the substrate. Shown in figure 2.31, by applying an external magnetic field, plastic deformation effect can be triggered at the boundary point of antenna and the microstrip feeding line. This effect results in the antenna being positioned at an angle over the substrate. Small deformation of the antenna (small angle) results in changes in operating frequency that preserve radiation characteristics, whereas larger angles result in frequency shifts accompanied by significant changes in the antenna radiation pattern.

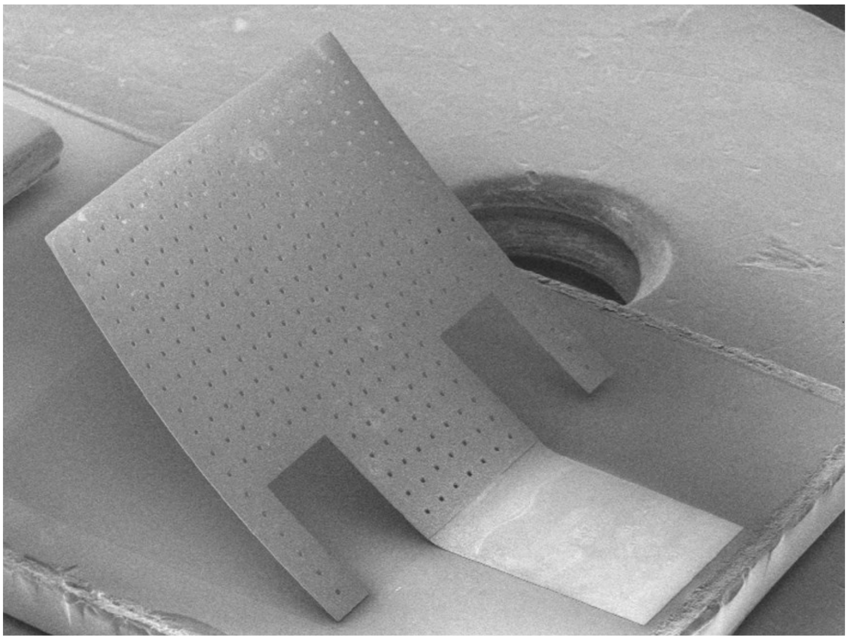

Figure 2.31. SEM photo of magnetically actuated reconfigurable patch antenna [87]

2.8.1.4. MATERIAL CHANGES

Changes in the material characteristics also promise the ability to tune antennas in frequency. In particular, an applied static electric field can be used to change the relative permittivity of a ferroelectric material, and an applied static magnetic field can be used to change the relative permeability of a ferrite. These changes in relative permittivity or permeability can then be used to change the effective electrical length of antennas, again resulting in shifts in operating frequency. One potential bonus is that these high relative permittivities and permeabilities substrate materials translating into greatly reduced antenna sizes. The main drawbacks to using ferroelectric and ferrite materials are their high conductivity compared to other substrates which will severely degrade the efficiency of the antenna.

Pozar and Sanchez proposed a frequency reconfigurable ferrite-based antenna in [88], which provided a 40% continuous tuning range with the variable static magnetic field in the plane of the substrate and perpendicular to the patch. However, the cross-polarization radiation performance of the design were significantly higher than those expected from a traditional rectangular microstrip antenna. Others have also investigated the properties of ferrite-based microstrip antennas [89-90], with results indicating that factors including non-uniform bias fields and the multiple modal field distributions excited in a ferrite substrate may preclude their use in practical applications.

Recently, several groups have developed ferroelectric materials in thin film to minimize the loss introduced into the circuit while still providing reconfigurability [91-93]. One thing need to be mentioned about those designs is that the tunable materials are used in the feed structure or parasitic elements rather than the antenna itself due to fabrication restriction of achievable uniformity of the films.

2.8.2. RADIATION PATTERN RECONFIGURABLE ANTENNAS

The distribution of currents, either electric or magnetic, on an antenna structure directly determines the spatial radiation pattern. This relationship between the source currents and the resulting radiation makes pattern reconfigurability without significant changes in operating frequency difficult, but not impossible to achieve. The reconfiguration mechanism can be categorized in following classes: Mechanical reconfiguration, electrical reconfiguration, parasitic tuning, and material reconfiguration.

2.8.2.1. MECHANICAL CHANGES

With the reflective surface physically removed and isolated from the primary feed, reflector antennas are a natural choice for applications that require radiation pattern reconfiguration independent of frequency. Clarricoats and Zhou demonstrated a radiation reconfigurable reflector antenna by actively changing the structure of a mesh reflector [94]. In its first prototype, the reflector contour was changed manually in certain regions, which resulted in changes in beam shape and direction. Later, computer controlled stepper motors were implemented to pull cables attached to specific points on the reflector mesh to support automatic pattern reconfiguration [95].

A closely related approach has also been used to develop a reconfigurable leaky-wave antenna using mechanical tuning [96]. A horizontally polarized antenna is utilized to couple energy into leaky transverse electric waves on a reconfigurable impedance surface (shown in figure 2.32). The waves propagate across the surface and radiate at an angle controlled by the surface resonance frequency with respect to the excitation frequency. The radiated beam from the surface can be steered in elevation up to 45°. Figure 2.33 shows a schematic layout of the surface, including the moveable top capacitance surface. The tuning layer is mechanically moved across the stationary high-impedance surface to vary the capacitance between the overlapping plates and tune the resonance frequency of the surface. An electronically tuned version of this antenna that employs varactors can produce reconfigurable backward as well as forward leaky-wave beams [97-98].

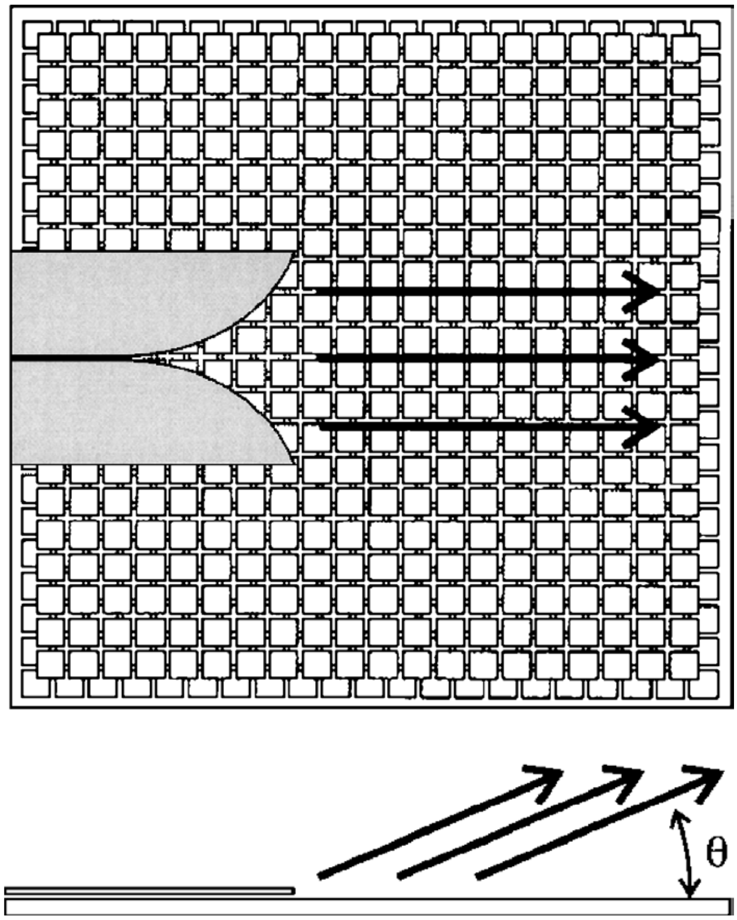

Figure 2.32. A horizontally polarized antenna couples energy into leaky modes on the tunable impedance surface. [96]

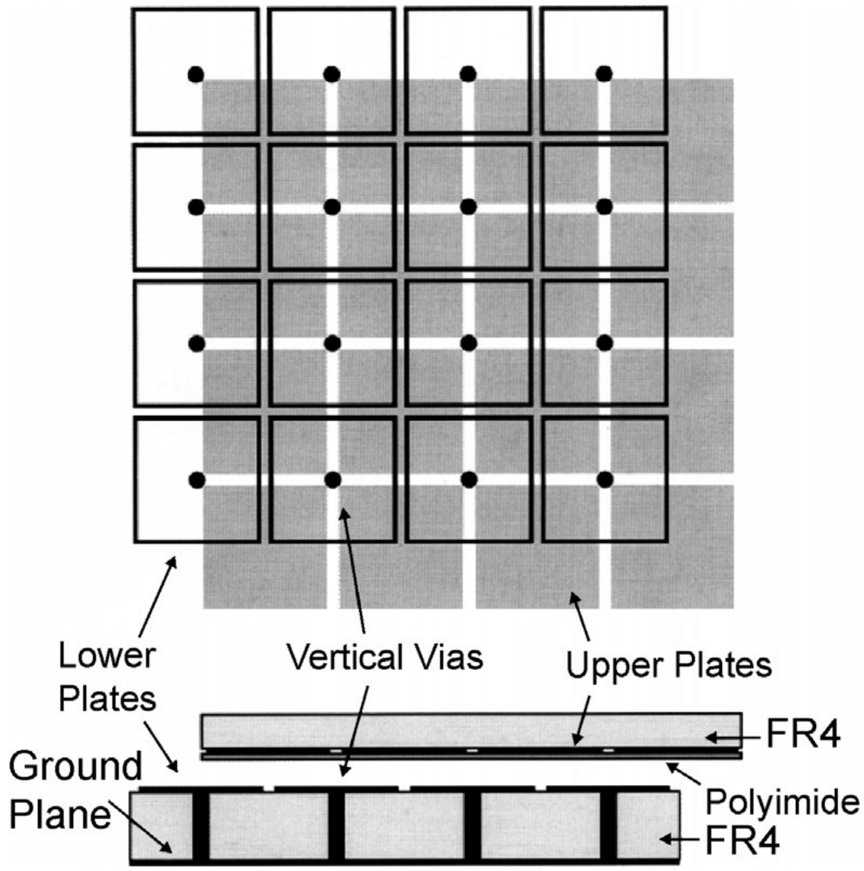

Figure 2.33. Schematic layout of mechanically reconfigurable impedance surface [96]

Chang et al. created pattern reconfigurability through enabling mechanical perturbation of propagation constants in a dielectric waveguide antenna operating at millimeter-wave frequency [99]. The propagation constant along a dielectric image line is gradually perturbed with a thin, moveable film placed on top of it (shown in figure 2.34). Different positions of the grating film present different grating spacing to the traveling wave and result in a scanned beam. Scan angles of up to 53° have been demonstrated with this design at 35 GHz. Scanned dual beam performance over a similar frequency range has been achieved with a related but more complex structure [100].

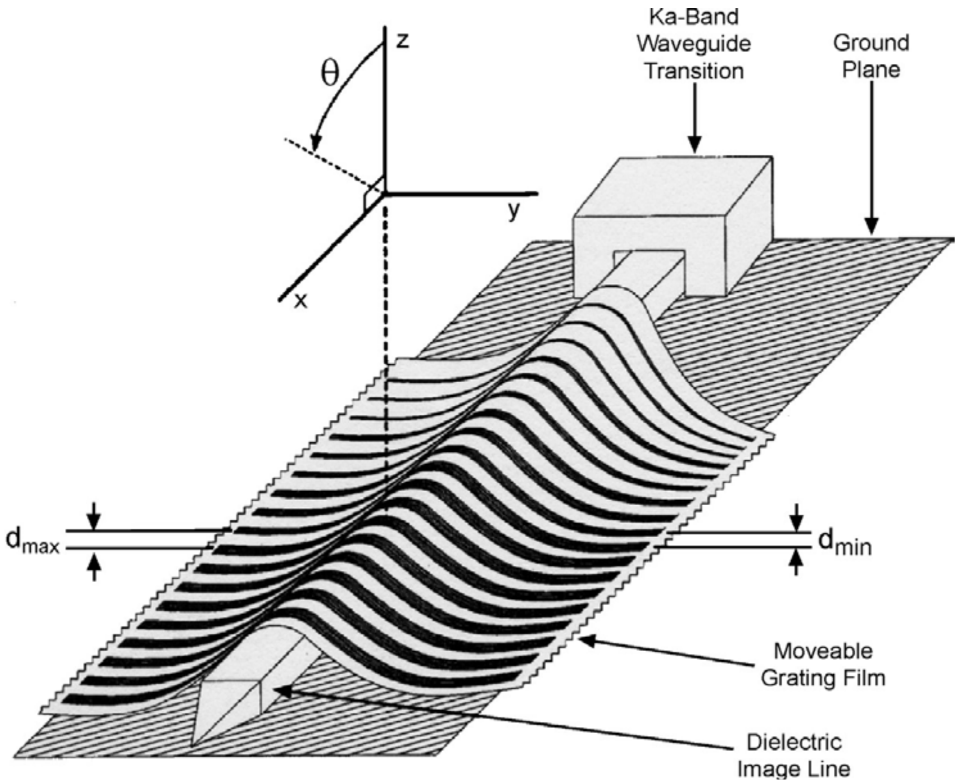

Figure 2.34. A traveling wave antenna based on moveable grating fed [100]

2.8.2.2. ELECTRICAL CHANGES

Generally electrical changes to a radiating structure usually result in changes in radiation characteristics. Nikolaou et al. designed an annular slot antenna for both frequency and pattern reconfigurability in [101]. Frequency reconfigurability for this antenna is supported through PIN diode switches that control input matching network, whereas the pattern reconfigurability is also done with PIN diode switches placed at locations around the slot to control the direction of a pattern null that is inherent to basic antenna operation [101].

2.8.2.3. PARASITIC TUNING

One of the most effective and widespread methods to change radiation patterns independently from frequency behavior is the use of electrically tuned or switched parasitic elements.

One good example is a microstrip based reconfigurable antenna using switched parasitic elements that developed by Zhang et al. [102]. Shown in figure 2.35, the antenna is composed of a single linear driven element with two spaced parasitic elements positioned on each side parallel to it. Parasitic element lengths can be changed with PIN diode switches, which, in turn, alter the magnitudes and phases of the currents on the parasitic elements relative to the driven element.

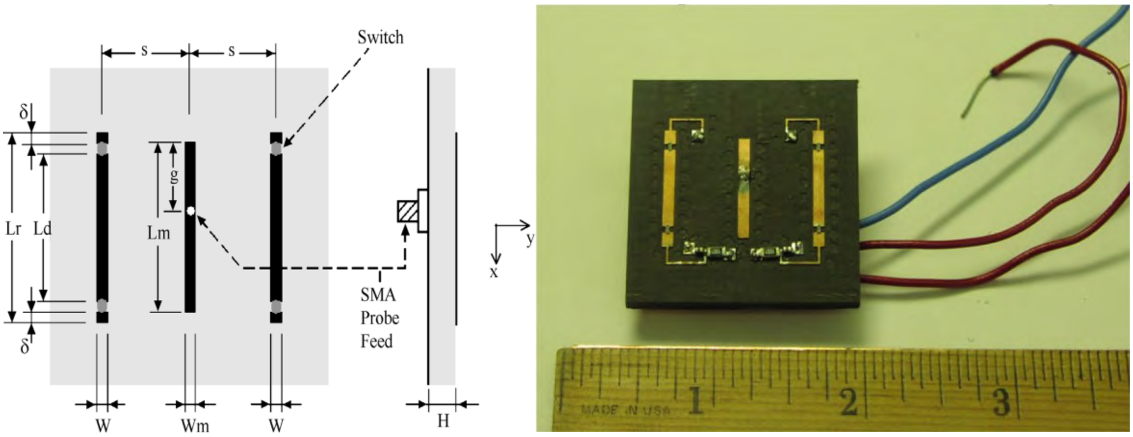

(a) (b)

Figure 2.35. Reconfigurable microstrip parasitic array (a) schematic layout and (b) photograph [102]

Note the careful design of the switch bias network in figure 2.35 (b) that minimizes the radiation from DC bias lines [103]. The operating spectrum and impedance bandwidth are not affected due to the driven element is isolated from the reconfigured sections of the structure. Other examples of small reactively steered planar arrays based on standard microstrip patches are provided by Dinger [104-105]. Search and optimization algorithms can be utilized to decide the tuning reactance necessary on each parasitic element to produce a beam or null at a prescribed angle [104-106].

2.8.2.4. MATERIAL TUNING

Ferrites and ferroelectric materials, although typically applied in frequency reconfigurable antenna, can also be used to reconfigure radiation patterns. The changes in material characteristics can be used to change the current distributions on conductors resulting in radiation pattern shifts, or they can be used to alter propagation speeds in traveling/leaky-wave antennas that result in beam steering.

The variable permittivity of a ferroelectric superstrate is used to achieve frequency fixed beam steering with a two-dimensional grid array of resonant slot antennas [107]. The complete structure consists of a grounded nonmagnetic substrate with a tunable ferroelectric superstrate, which is then covered with a conducting plate that supports a two-dimensional array of radiating slots (figure 2.36). When the applied voltage changes between the conducting plate and the ground plane, the permittivity of the ferroelectric shifts and the beam direction of the structure changes [107].

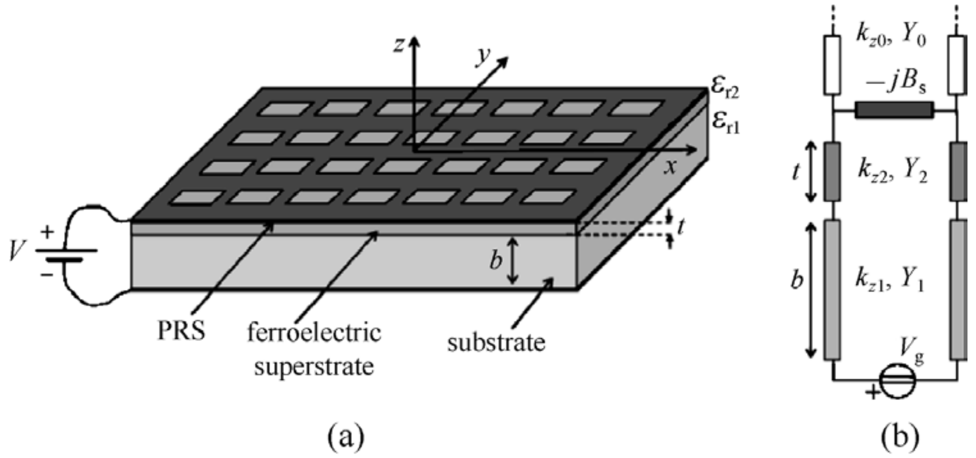

Figure 2.36. Schematic layout of the ferroelectric reconfigurable leaky-wave antenna [107]

Other reconfigurable leaky-wave antennas that include tunable ferroelectric materials in planar configurations have also been reported [108-109].

A two-dimensional beam steering phased array antenna based on a combination of ferroelectric material adjustment and the continuous transverse stub topology has been reported in [110]. Similar to other reconfigurable leaky-wave antennas that employ integrated phase shifting, ferroelectric material integrated into the feeding waveguide is tuned to deliver desired phase shifts between radiating stubs that then results in beam steering up to 60° from broadside. As shown in figure 2.37, the height of the waveguide is varied across the array simple to preserve good impedance matching. The electrical distance between the radiating stubs changes as the permittivity of the ferroelectric loading material is varied with applied voltages, so the phase on each stub can be controlled to generate different radiation patterns (figure 2.38). An antenna based on similar concepts but using individually biased ferrite rods between radiating slots in a waveguide is discussed in [111].

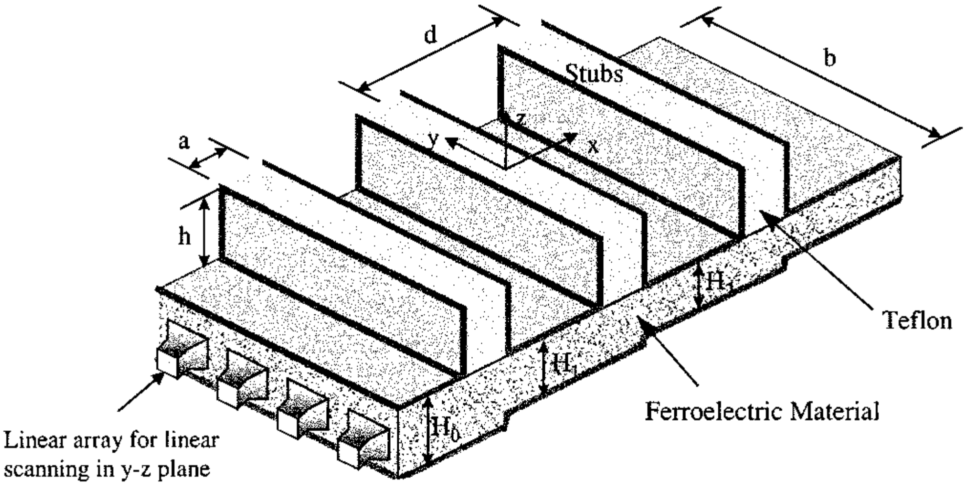

Figure 2.37. Continuous transverse stub design with ferroelectric material fill for beam scanning in the X-Z plane. [110]

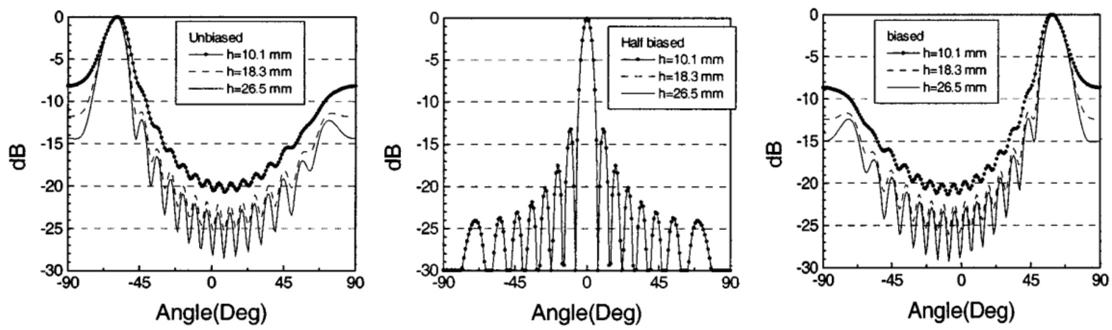

(a) **(b)** **(c)**

Figure 2.38. Radiation patterns for three different bias voltages: (a) unbiased (b) half biased (c) full biased [110]

CHAPTER 3

PHASE SHIFTER AND SLOW WAVE STRUCTURES

In this chapter, a phase shifter is presented first. It is based on radio frequency Nano-Electro-Mechanical Systems (NEMS) switch fabricated at our lab in the University of New South Wales. To further reduce the chip size of the delay line phase shifter, two slow wave structures are then demonstrated.

3.1. PHASE SHIFTER

3.1.1. INTRODUCTION

Nano-Electro-Mechanical Systems (NEMS) are devices and systems that have been studied and designed with dimensions of the order of nanometer. Compared to MEMS, NEMS are about a thousand times smaller and have a great number of potential applications such as random access memory, NEMS switch matrices and nano-tweezers [112-114]. MEMS technology has been deployed to operate ordinary tasks in present day and had significant impact on automobile, wireless communications, medical and aerospace areas. Today, numerous companies are making MEMS devices for a wide range of clients. With the semiconductor technology approaching deep into the submicron range, a flood of ideas of developing much smaller NEMS structures have been reported [115].

A raft of NEMS switch designs have been carried out based on carbon nano-tubes. Carbon nano-tubes are promising for developing NEMS structures due to their extraordinary electrical and mechanical attributes. At present, the studies of NEMS switch are mostly focusing on their applications in random access memory systems and they have not been able yet to make considerable progress for the communication systems [116].

Microwave phase shifter is an important component in phased array antennas for wireless communications and radar applications. They are currently employing ferrite materials, PIN diodes, or FET switches [117]. RF MEMS switches based phase shifter designs result in lower loss at most frequency bands, especially at high frequency band. RF MEMS switches exhibit very small open switch coupling capacitance and close switch resistance. They provide better RF performance and usually wider bandwidth than similar designs using solid-state devices. RF MEMS shifters also consume considerably less DC power compared to the PIN or FET switch based phase shifters. There are several types of MEMS phase shifters have been explored based on different techniques such as reflection-line, switched delay-line, loaded-line, varactor and switched capacitor-bank [118]. In this work, the switched delay-line technology is employed to design the 3-bit phase shifter.

The terahertz band (lies from 0.1 to 10 THz range) has become an emerging area of research due to constraint on lower frequency band. The antennas that designed to work at 600 GHz have been reported [119-121]. High frequency band and broad bandwidth can offer large capacity for wireless communication applications.

In this section, a phase shifter was designed and simulated. It is based on radio frequency NEMS switch fabricated at the University of New South Wales in [122], additional work needs to be done to optimize the fabrication processes. The NEMS switch is fabricated with surface micromachining technique and the dimension including the CPW ground plane is 1.7 μm × 3.0 μm. The length of cantilever is 1.4 μm and the actuation gap is 170 nm. This phase shifter was designed to operate at 600 GHz and the simulated frequency band is from 550 GHz to 650 GHz.

3.1.2. DESIGN OF 3-BIT PHASE SHIFTER

3.1.2.1. CIRCUIT DESIGN

To achieve a 3-bit phase shifter, three individual bits are designed. The cascade layout of the whole structure is shown in figure 3.1. Each bit phase shifter has two sets of NEMS series switches located next to the T-junctions. They share the same reference transmission line length and their delay lines are designed to offer phase shift of 22.5º, 45º and 90º respectively. There are eight different states ranging from 0º to 157.5º with 22.5º steps. To minimize the coupling between adjacent transmission lines, three shifters are arranged in an interlacing way as shown in figure 3.1.

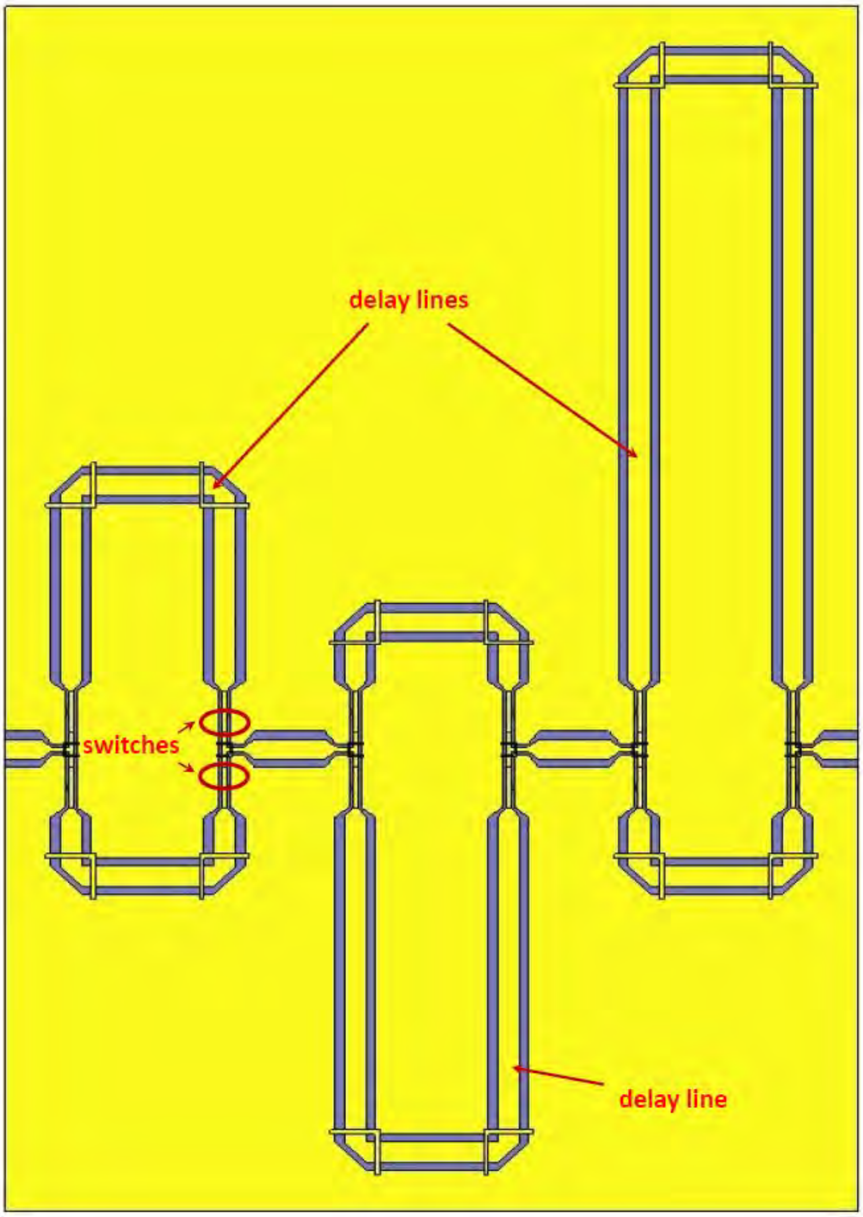

Figure 3.1. Layout of 3-bit phase shifter

The phase shifter is designed with coplanar waveguide structure built on an Alumina substrate with 254 μm thickness. The alumina substrate has a lot of features make it a preferable option for phase shifter and RF NEMS switches compared to silicon substrate. These advantages includes availability, losses and low tangent. The RF NEMS switch has a 40 nm thick chromium electrode fabricated under the cantilever beam and covered with a silicon nitride layer. This thin dielectric layer of 190 μm thickness is deposited using

Plasma Enhanced Chemical Vapor Deposition (PECVD) to prevent direct contact between metal cantilever and the lower electrode. The CPW structure is constructed on the top of silicon nitride layer using gold for conductor material with a thickness of 100 μm.

3.1.2.2. BUILDING BLOCKS

The 1-bit phase shifter can be broken down into four segments: the RF NEMS cantilever switch, the 180° Turn, the transmission delay line and the T-junction.

1) *RF NEMS Cantilever Switch*: The NEMS switch is an essential component of phase shifter performance. When the switch is in up-state position, it should provide high isolation between the cantilever tip and the transmission line. While the switch is actuated, the signal will course through the switch without suffering high insertion loss or being reflected back. The CPW signal line width is 200 nm and the gap between the center line and the ground plane is 150 nm resulting a characteristic impedance of 50 Ω (figure 3.2 (a)). As presented in figure 3.2 (b), it can be observed that the switch could achieve an isolation better than 39 dB at 600 GHz. When the beam is in down-state, the return loss and insertion loss are 30 dB and 0.16 dB respectively.

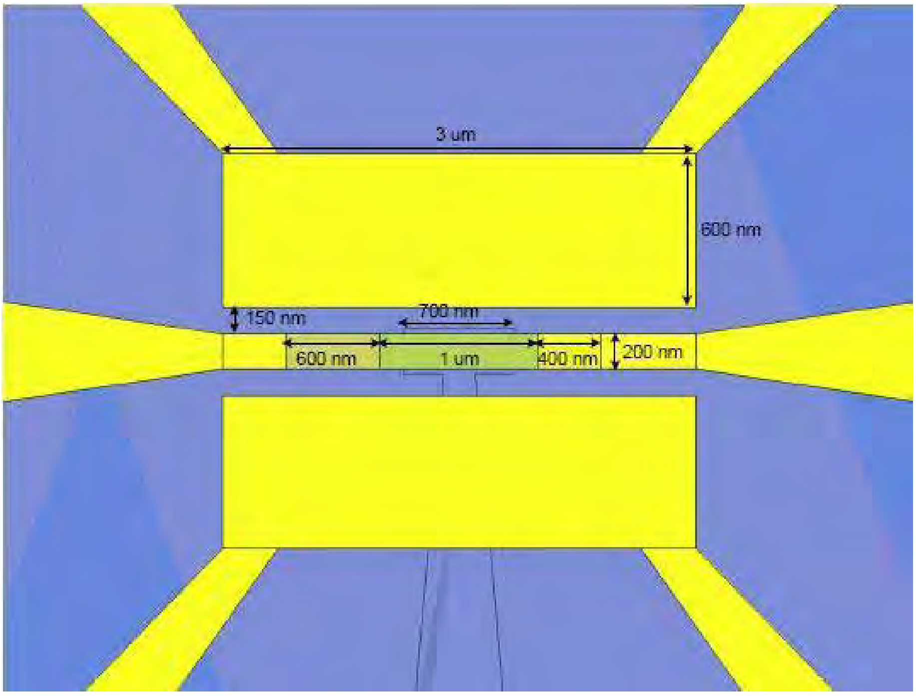

(a)

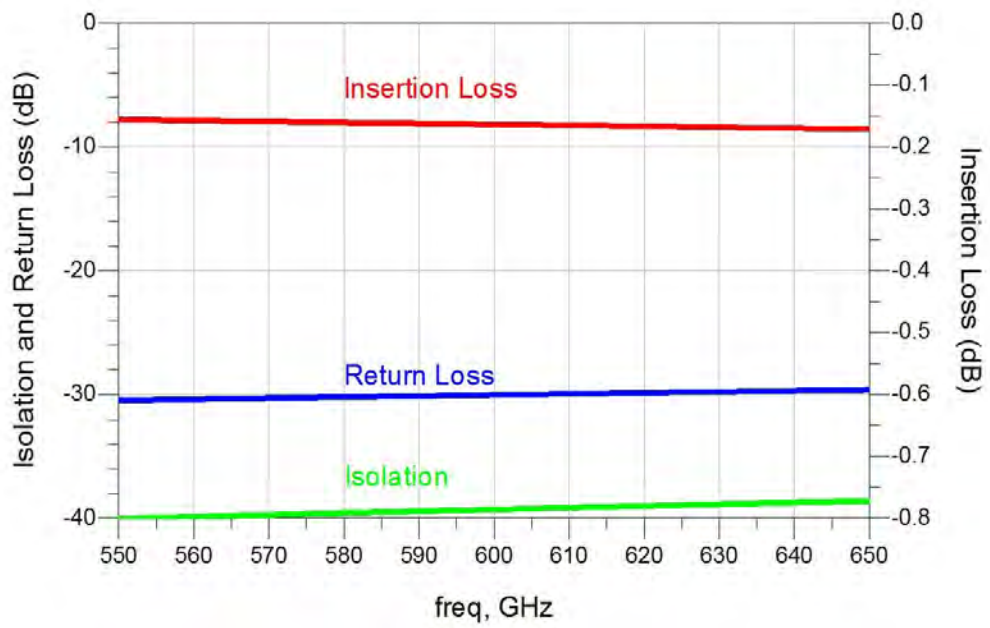

(b)

Figure 3.2. RF NEMS switch (a) physical layout and (b) simulation results

2) *180° Turn*: The turn structure is shown in figure 3.3. Air bridges are employed to connect the two ground planes in order to reduce the parasitic coupled slot line mode and maintain a constant phase shift throughout the CPW turn structure [123]. However, the air bridges add parasitic capacitance to the bend and degrade its performance. In addition

the bend reactance is also responsible for performance degradation. Chamfering the corners provides a simple method to compensate for both parasitic capacitance as well as bend reactance. Air bridges are fabricated using similar process to the NEMS switches. They are anchored on both ends instead of keeping one end open.

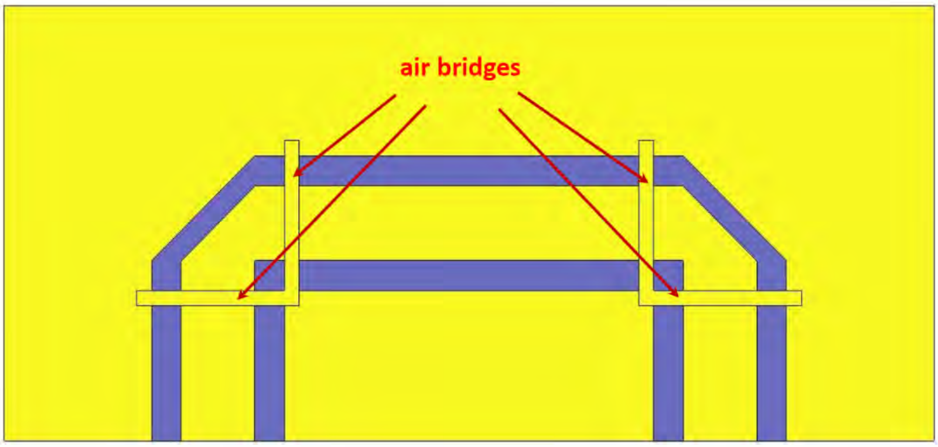

Figure 3.3. Proposed 180° Turn

As can be seen from figure 3.4, the return loss of the proposed turn is 23.6 dB at the required frequency, which indicates fairly good impedance match at 600 GHz.

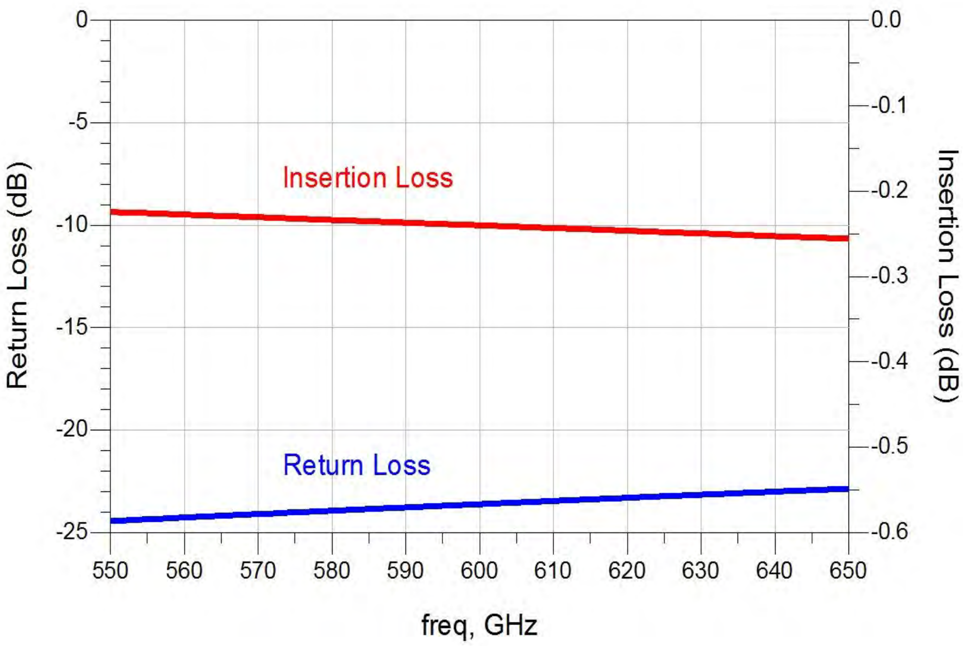

Figure 3.4. Simulated results of 180° Turn

3) *Transmission delay line*: The delay line phase shifter uses the length of the transmission delay lines in each 1-bit shifter cell to vary the phase angle. For the high operating frequency and the dimension of the switch, a suitable dimension of transmission line has to be selected so that an acceptable insertion loss could be obtained without degradation of the whole device's performance. The transmission line uses as the delay line has a wider center conductor and slot width compared to the original dimension of the RF NEMS switch. The delay line dimensions are presented in figure 3.5.

Figure 3.5. Proposed transmission delay line with dimension

Figure 3.6 shows a comparison of the performance of the transmission line with different dimensions for a 45° phase angle shift. As can be observed from the diagram, the insertion loss and the return loss could have up to 0.75 dB and 10.19 dB differences respectively at 600 GHz. Although the losses are still not ideal, the selected delay line provides a significant improvement in performance. At the same time it maintains the compactness of the overall dimension.

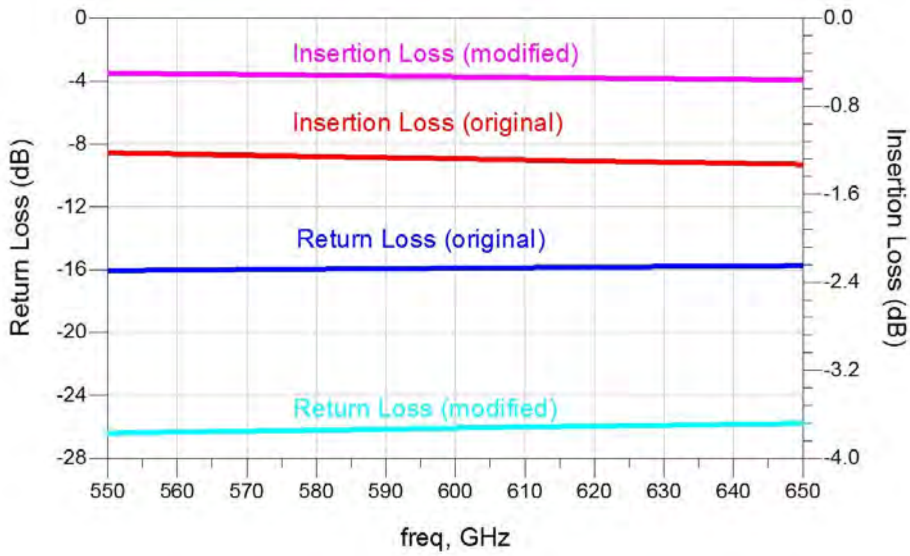

Figure 3.6. Comparison of original and selected transmission line

As the size of the transmission line is increasing, a designated connector should be used for connecting the delay line with the cantilever beam switch to overcome the phase and amplitude errors caused by discontinuity [123]. A miter step connector is designed to minimize the effect of parasitic reactance by compensating the discontinuity directly.

4) *T-junction*: T-junction is a key element that determines the operating bandwidth of the 3-bit phase shifter. A 3-D model of T-junction with two NEMS switches located symmetrically adjacent is demonstrated in figure 3.7. The two switch openings are designed to face towards the T-junction in order to reduce the transmission line length between them for minimizing the capacitance load. Air bridges are used to reduce parasitic modes and the dimensions used are the same as in the 180° turn subsection. In the operation of a 1-bit phase shifter, each set of the cantilever switches always has one switch in up-state and the other in down-state as signal either goes into the reference

transmission line or the designated delay line.

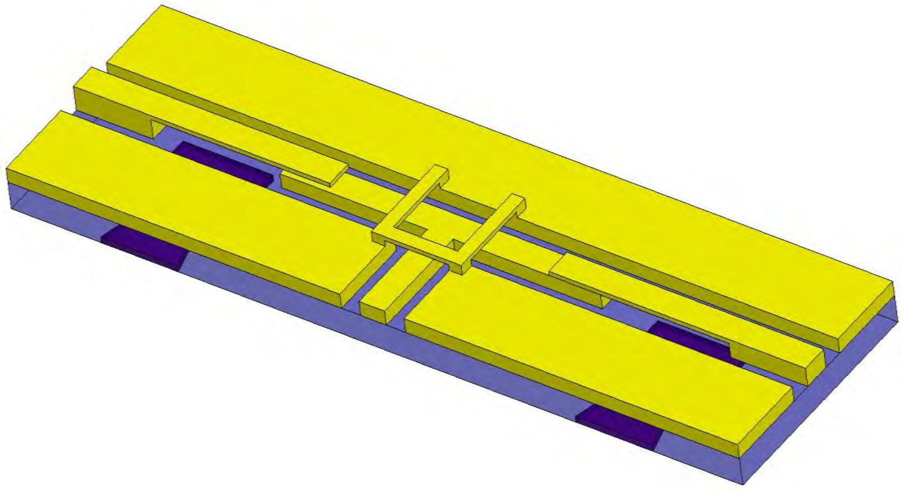

Figure 3.7. Proposed T-junction with switches

It is critical to satisfy the characteristic impedance matching condition in order to achieve good return loss. The T-junction together with the NEMS switches has been optimized and the simulated results are illustrated in figure 3.8. As it can be seen, the return loss is better than 32 dB while the insertion loss is 0.19 dB at 600 GHz. Please note that contact resistance is not included in the simulation due to the difficulty in estimating the value at nano-scale and also it is difficult to include in the simulation.

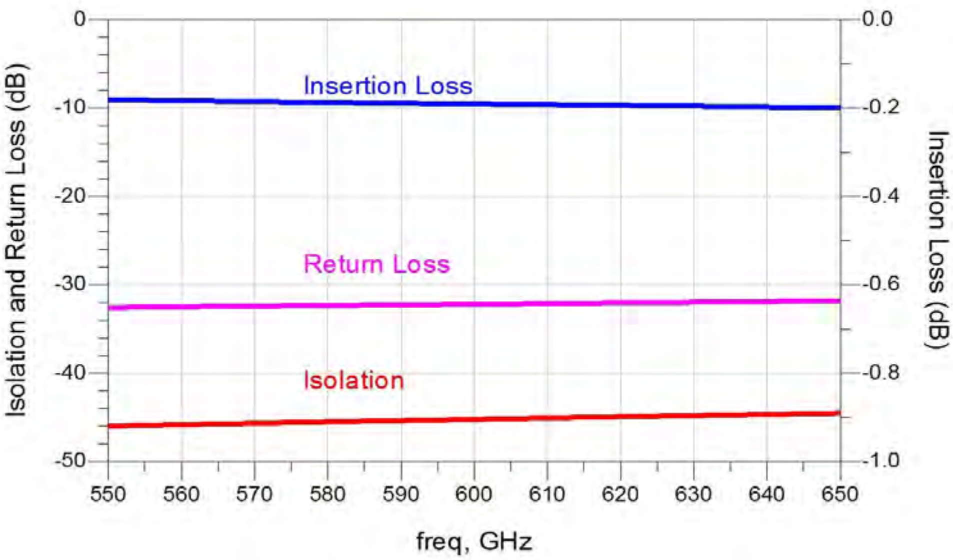

Figure 3.8. Simulated results of T-junction with switches

3.1.2.3. 3-BIT PHASE SHIFTER SIMULATION

The 3-bit phase shifter has been constructed using the proposed blocks. The simulation results for 3-bit phase shifter are summarized in table 3.1 and all bit combinations are plotted in figure 3.9.

Table 3.1. Simulation results for 3-bit phase shifter at 600GHz

Expected Phase	Phase Shift	Phase Error	Insertion Loss (dB)	Return Loss (dB)
0°	0°	0°	2.312	23.588
22.5°	21.619°	0.881°	2.55	25.977
45°	43.548°	1.452°	2.778	33.817
67.5°	65.708°	1.792°	3.033	28.182
90°	88.155°	1.845°	3.266	20.773
112.5°	109.894°	2.606°	3.527	22.06
135°	131.646°	3.354°	3.777	22.178
157.5°	154.893°	2.607°	4.091	23.827

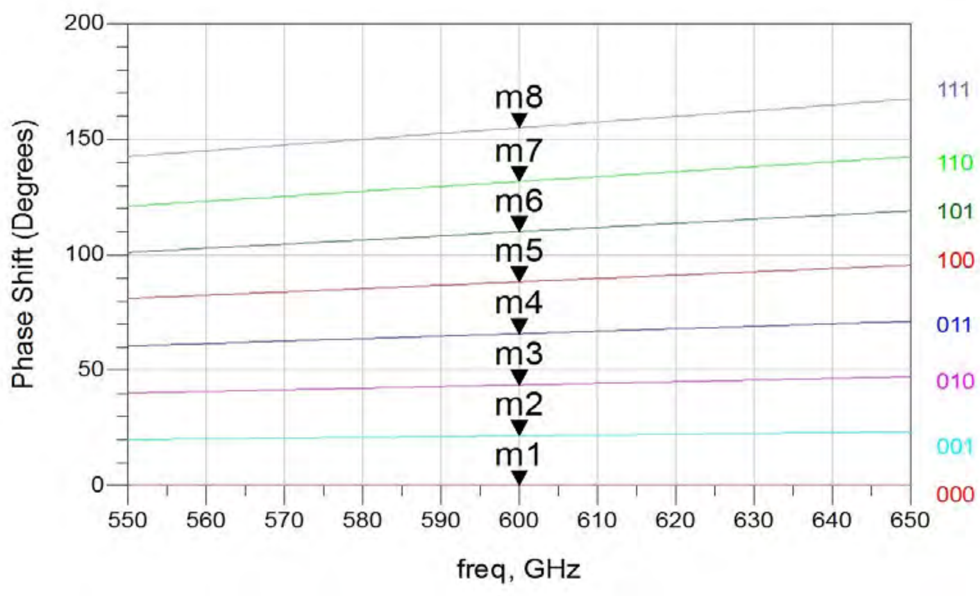

Figure 3.9. Phase shift for all bit combinations

Both the phase error and return loss have excellent values. From the simulated data in Table 3.1 and figure 3.9, it can be seen that the 3-bit phase shifter achieved phase error of ±5% and the maximum phase error of 3.91% occurs at 22.5°. The return loss of all states is better than 20 dB. The shifter has a maximum insertion loss at 157.5° and the insertion loss is 4.091 dB. Given that this device is operating at 600 GHz and the whole structure is integrated into a 59.3 μm × 37.8 μm chip, it can be predicted that the transmission signal will obtain high attenuation from CPW conductor loss and substrate loss. However, to achieve high integration ability and nanometer scale device, this tradeoff is necessary.

3.1.3. CONCLUSION

An operating 3-bit NEMS delay lines phase shifter has been designed, and optimized. Problems like high insertion loss of the transmission line, CPW bend phase error and impedance mismatch of the T-junction were encountered during the design. The enlarged delay line, air bridges and a miter step connector were employed to the design to overcome these drawbacks.

3.2. SLOW WAVE STRUCURES

In this section, two slow wave branch-line couplers based on microstrip line are presented. As can be seen from previous phase shifter design, the major component that take up space on the substrate is the transmission delay line. To further reduce the length of delay line, the microstrip based slow wave structure is a promising solution; especially for the applications operating at lower spectrums such as 2.4 GHz band or 5 GHz band. This work was a collaboration with undergraduate student Vicki Zhu. We designed and optimized the structures; and Ms. Zhu was working under my supervision.

3.2.1. INTRODUCTION

A microstrip line plays a vital role in microwave circuits since it can be easily fabricated by photolithographic processes and integrated with passive and active devices. The length of the conventional microstrip line is dominated by the dielectric constant [124] so the phase velocity in these circuits cannot be further reduced to less than the free-space light velocity. Therefore, the circuit may occupy a large area, which results in high cost and problems for miniaturization.

Slow-wave guiding structures have been extensively studied to reduce the circuit size [125-143]. The mechanism behind the slow-wave propagation is to store the electric and magnetic energies separately as much as possible in the guided-wave media. The microstrip type slow-wave structures can be constructed in multilayer substrates [129-131]. However, to simplify the fabrication process and to maintain the low cost, the slow-wave structures with only a single-layer substrate are more preferable [132-143]. One option is to create a periodic dielectric constant on a single-layer wafer [132]; other options includes building structures to form the periodic perturbations on the signal and ground planes [133-143].

3.2.2. DESIGN OF SLOW WAVE BRANCH-LINE COUPLER

The designs are intended to be fabricated utilizing a commercial ink-jet printer so multi-layers 2D printed structure are used. Polyester substrate is selected over normal paper substrate for its significantly lower attenuation. The structure will be printed with silver nano ink which is commercially available [144]. The silver nano ink and cleaning ink cartridges are shown in figure 3.10, and the coated printing paper and polyester substrate are illustrated in figure 3.11.

(a) **(b)**

Figure 3.10. Methode (a) silver nano ink and (b) cleaning ink cartridges

Figure 3.11. From left to right: coating paper, opaque polyester, transparent polyester

3.2.2.1. CIRCUIT DESIGN

Two slow wave branch-line couplers were designed and optimized. The configurations are shown in figure 3.12. The branch-line coupler consists of four λ/4 line sections, two of which have the characteristic impedance of 35.36 Ω and the other two have the characteristic impedance of 50 Ω. The proposed branch-line couplers replace these four microstrip transmission lines with slow-wave structures. The designed branch-line couplers utilize spectrum centered at 940MHz. This spectrum is chosen to maintain the smallest features because the resolution of our commercial printer is limited.

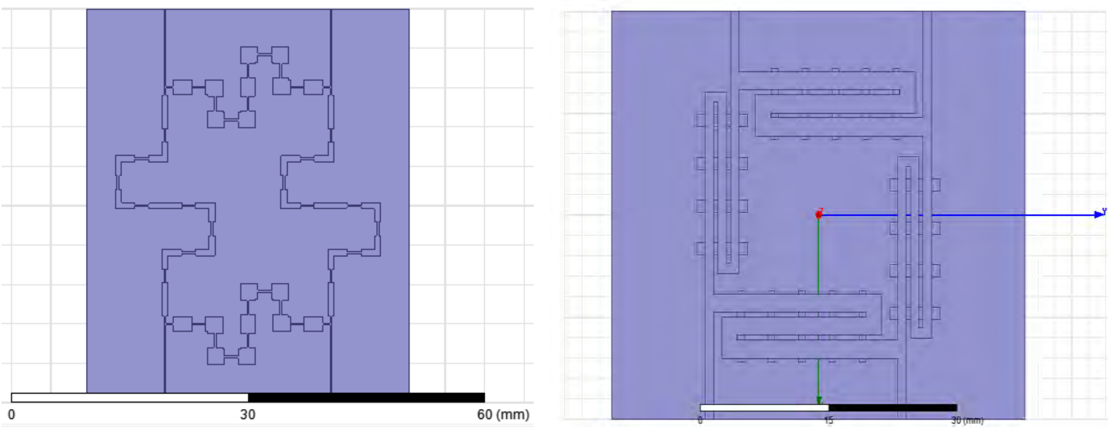

(a) **(b)**

Figure 3.12. Schematic layouts of slow wave branchline couplers (a) type A and (b) type B

3.2.2.2. BUILDING BLOCKS

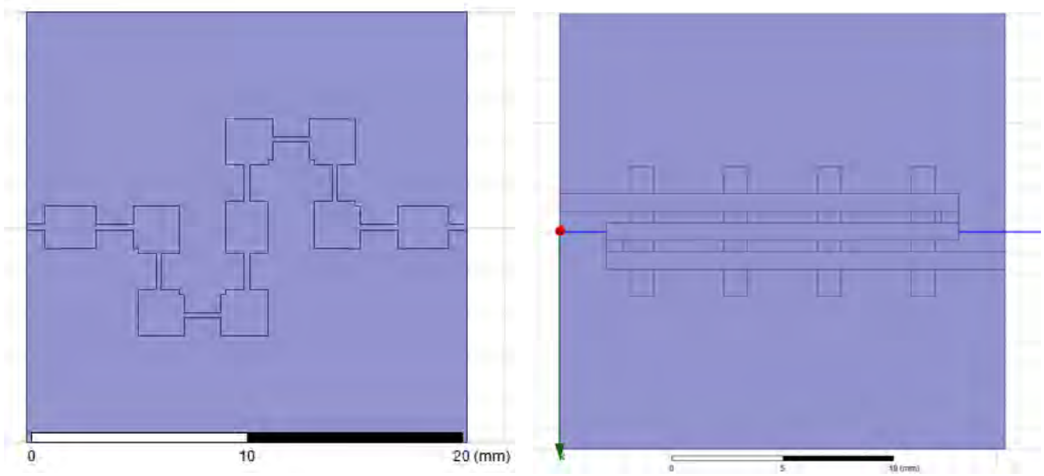

(a) (b)

Figure 3.13. Schematic layouts of slow wave unit cell (a) type A and (b) type B

The unit cell of proposed slow wave structure are shown in figure 3.13. These structures are inspired by the step impedance filter design. The cascaded high impedance and low impedance transmission lines can be translated into series inductors and shunt capacitors. The equivalent circuits of the unit cells are illustrated in figure 3.14. The series inductors and shunt capacitors can store the magnetic and electric energies separately. Therefore the phase velocity can be reduce and the wavelength $\lambda = \frac{v}{f}$ becomes smaller as well as the total device size for certain wavelength.

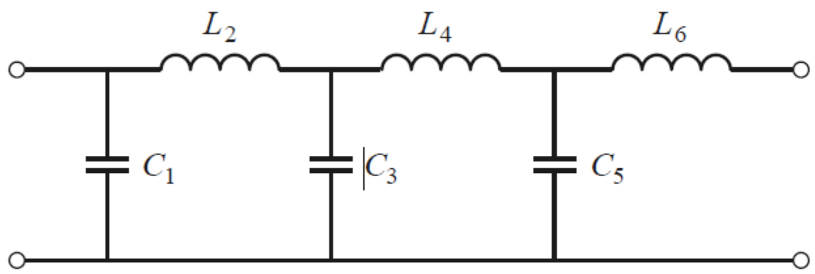

Figure 3.14. Equivalent circuit for proposed slow wave structure

The meander line structure is also adopted to further reduce the size of transmission line. Type A unit cell is connected different width line to form high or low impedance lines. Type B adds conductive load under the conventional transmission line to form the slow wave structure. Type B branch-line coupler will be simple to fabricate by utilizing the ink-jet printing technology. The structure can be printed on separated polyester papers and then align and heat bind them together.

3.2.2.3. SLOW WAVE BRANCH-LINE COUPLER SIMULATION

As can be seen from the figure 3.15, Both type A and type B branch-line coupler's S11 and S41 show desirable results of low return losses. The insertion losses of the type A branchline coupler (S21 and S31) give values of roughly -3.6 dB at the resonance frequency, while the type B branch-line coupler has S21 and S31 closed to -4.3 dB. These values are lower than the ideal -3dB, the additional losses are introduced by the metal and dielectric losses.

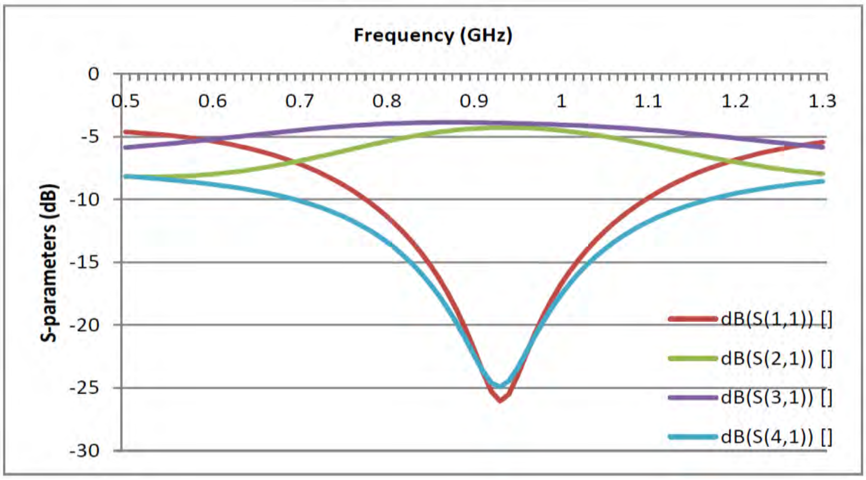

(a)

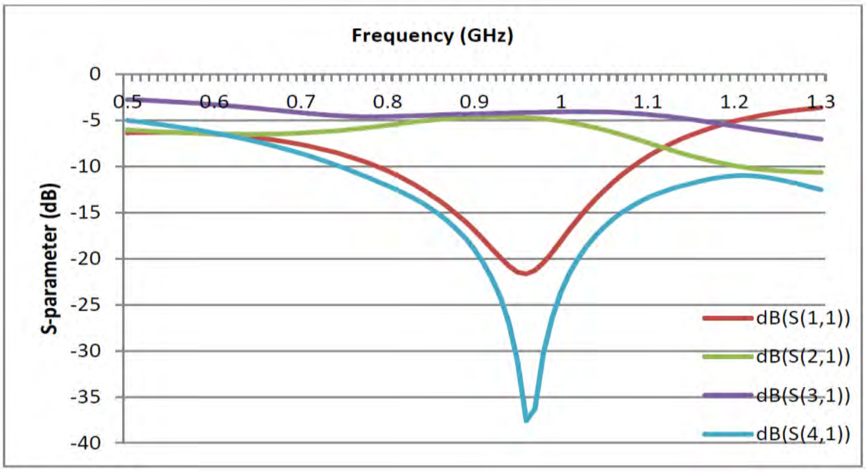

(b)

Figure 3.15. Simulation results of branch-line couplers (a) type A and (b) type B

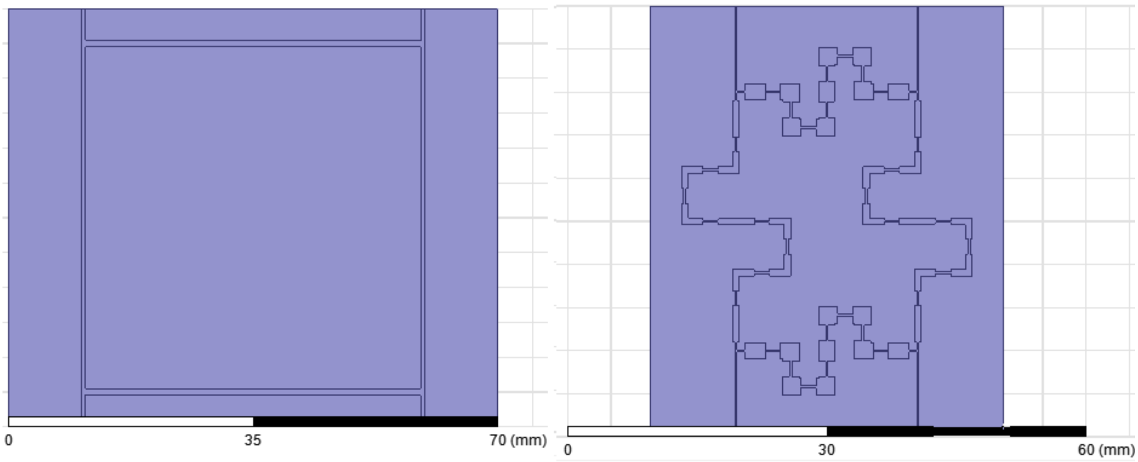

Figure 3.16. Size compare between conventional microstrip and slow wave branch-line couplers

When compared to the conventional microstrip branch-line coupler, the total chip sizes can be reduced to 28% and 39% for type A and type B branch-line coupler, respectively.

3.2.3. CONCLUSION

In this section, two types of slow wave structures are proposed and simulated. The advantages of proposed slow wave structures are low fabrication cost (due to they only need single layer printing, no via-hole and no ground plane patterning), compact size and easy to integrate with the existing MMIC circuits.

CHAPTER 4

FREQUENCY RECONFIGURABLE ANTENNAS

In this chapter, new millimeter-wave frequency reconfigurable quasi-Yagi and folded dipole Yagi antennas are presented. The antennas are printed on a quartz substrate integrated with RF MEMS switches. By controlling the actuation of the RF MEMS loaded on the driven and director dipole elements, the antenna operation frequency is switchable in the wireless personal area network (WPAN) band (57-66 GHz) and E-band (71-86 GHz). The end-fire patterns of the Yagi antennas are maintained in both two-bands.

4.1. MEMS-LOADED MILLIMETER WAVE FREQUENCY RECONFIGURABLE QUASI-YAGI DIPOLE ANTENNA

4.1.1. INTRODUCTION

In commercial communications systems, there is a continuous demand toward smaller and more adaptive communications platforms that possess multiple functionalities. Meanwhile, the unlicensed 60 GHz spectrum (57 - 66 GHz) and the light licensed E-band spectrum (71 – 86 GHz) have become available in many countries. The wide channel bandwidth attracted tremendous research and commercial interests to develop 1 Gb/s or even higher wireless transmission, catching up their optical fiber counterpart, in the millimeter-wave spectrum range [145]. In the millimeter-wave spectrum, RF MEMS devices exhibit attractive characteristics in terms of high isolation, low insertion loss, low dc power consumption, and excellent linearity [146]. A comprehensive comparison between semiconductor and RF MEMS switches reveals that the latter is more suitable for millimeter wave applications [147]. RF MEMS switch has been widely employed in the designs of reconfigurable filters for multi-standard radio front end [148], phase shifters [149], switch matrix [150], and reconfigurable antennas [151-152]. It is expected the RF MEMS will be commercially employed in future software defined radio and cognitive radios. As an important component of the future radio system, a millimeter-wave frequency reconfigurable antenna allows one antenna being shared for multiple high data-rate wireless services. Wideband printed Yagi antenna with 44% frequency bandwidth has been reported in X-band with moderate gain [153]. Wideband operation of Yagi antennas in E-band has also been demonstrated with a compact design of using folded dipole driven element [154]. However, very little research work has been reported on the design of millimeter-wave frequency reconfigurable antenna. In this section, we propose a new design of a RF MEMS integrated millimeter-wave frequency reconfigurable quasi-Yagi dipole antenna. The aims of our research are two-fold: (1) to realize a frequency switching in two millimeter wave frequency spectrums, which are the 60 GHz band from 57 to 66 GHz and the whole E-band from 71 to 86 GHz; (2) to demonstrate a RF MEMS integrated quasi-Yagi antenna incorporating practically feasible biasing configurations.

4.1.2. ANTENNA DESIGN

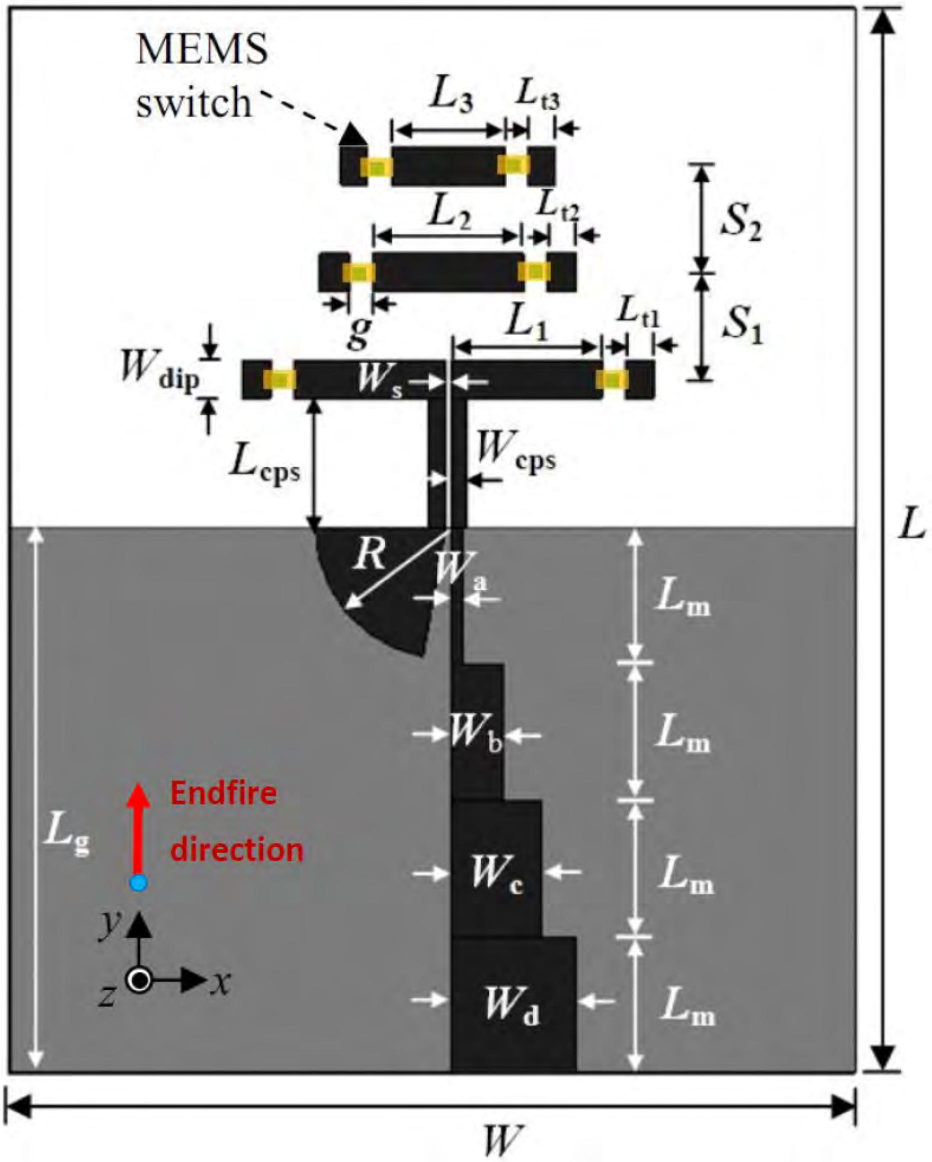

Figure 4.1. Schematic layout of the MEMS-loaded millimeter-wave frequency reconfigurable quasi-Yagi dipole antenna

Table 4.1. Antenna dimension parameters (unit: µm)

L	W	L_g	L_m	L_1	L_2	W_a	W_b
5000	4000	2300	575	535	570	45	190
L_3	L_{t1}	L_{t2}	L_{t3}	S_1	S_2	W_c	W_d
430	215	155	145	470	530	380	530
R	g	L_{cps}	W_{cps}	W_{dip}	W_s		
550	120	520	70	180	18		

The configuration of the proposed reconfigurable antenna is shown in figure 4.1 and its dimensions are listed in table 4.1. The dipole elements and feeding structures are printed on a low-loss quartz substrate (ε_r = 3.75, thickness h = 0.254mm, tanδ = 0.0004), on which the RF MEMS switches are integrated. The top metallization consists of a driven dipole element, two parasitic director elements, a CPS line and a broadband microstrip-to-CPS transition. The bottom truncated ground plane serves as a reflector element. The combination of the reflector, driven dipole and parasitic directors forms a four-element quasi-Yagi array which results in an end-fire radiation (figure 4.1). Six RF MEMS switches are embedded in gaps on the driven and director elements as shown in figure 4.1. By controlling the biasing voltages applied on the beams and the electrodes of the RF MEMS switches, the effective lengths of the dipole elements are changed so that the resonant frequency of the antenna is altered.

The cantilever RF MEMS switch is employed and the layout of the switch is shown in figure 4.2. The RF MEMS switches are integrated on the same quartz substrate as the antenna structure. Biasing lines are defined by evaporating 0.04 μm layer of silicon chromium [155] and then patterned by one mask. Next a 0.7 μm height electrode is fabricated under the cantilever beam and covered by a 0.15 μm thick layer of silicon nitride. The thin dielectric layer is deposited to prevent direct contact between the metal cantilever and the lower electrode. The antenna structure and the matching network are defined by RF sputtering of 0.04/1.0 μm layer of Cr/Au. Chromium can be used as an adhesion layer between the gold and substrate. The length of the cantilever is 130 μm and the actuation gap is 2.5 μm.

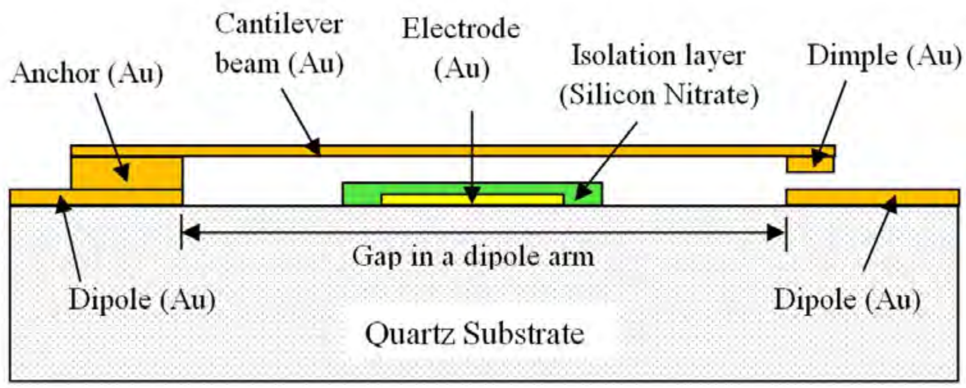

Figure 4.2. Schematic layout of the cantilever beam based MEMS switch.

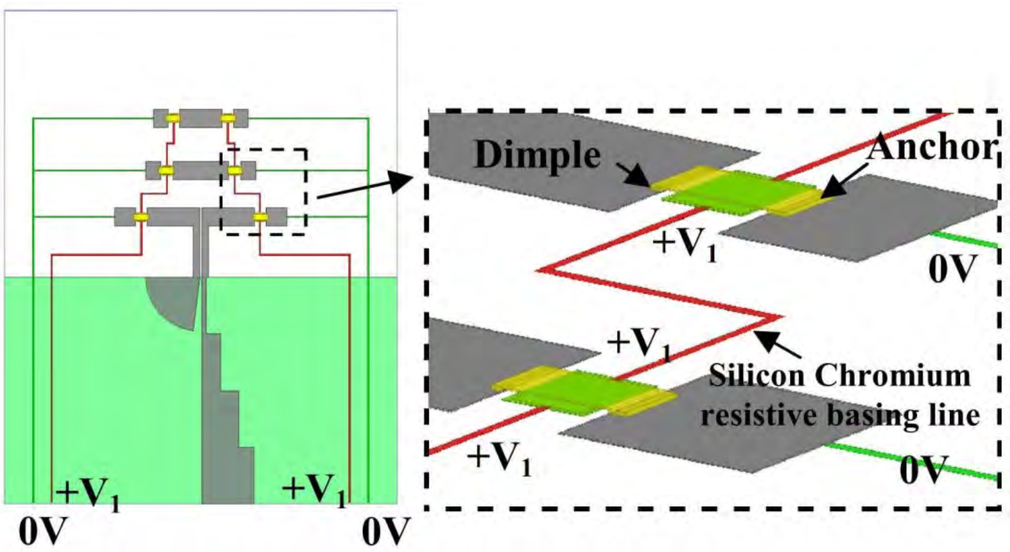

Figure 4.3. Resistive biasing configuration for the proposed reconfigurable antenna. Zoomed-in diagram shows the detail of the biasing line and the orientation of the RF MEMS switches.

In this work, a high resistive silicon chromium biasing network is proposed as shown in figure 4.3. The dimple of the cantilever beam is facing inwards and the anchor is placed on the far-end side of the dipole elements. To simplify the biasing network, the electrodes of the each three RF MEMS switches on one side are connected together as a group. The biasing lines in red color are extended and positive voltage is applied (+V1) to control the switch actuation. The anchors of the RF MEMS switches are located at the far end of the dipole connected to a reference dc ground. It is noted that there is almost no current between the cantilever beams and electrodes while the switches are actuated. This feature guarantees that the cascaded electrodes (inter-connected each other) will share the same biasing voltage +V1 as shown in the zoomed-in plot of the biasing lines in figure 4.3. When the biasing voltage is applied to the electrode, the dimples of the six RF MEMS switches will be pulled down touching the gold dipole arm (ON state). Therefore, the gap is bridged to form longer dipoles (L_n + g + L_{tn}) and the antenna operates in the lower band. Conversely, the quasi-Yagi array operates in the higher band with the shorter dipole lengths (L_n) when no voltage is applied (OFF state). The pull-down voltage is decided mainly upon the width and length of the cantilever beam as well as the actuation gap. This voltage is calculated to be 38 V by MEMS mechanical simulator — CoventorWare.

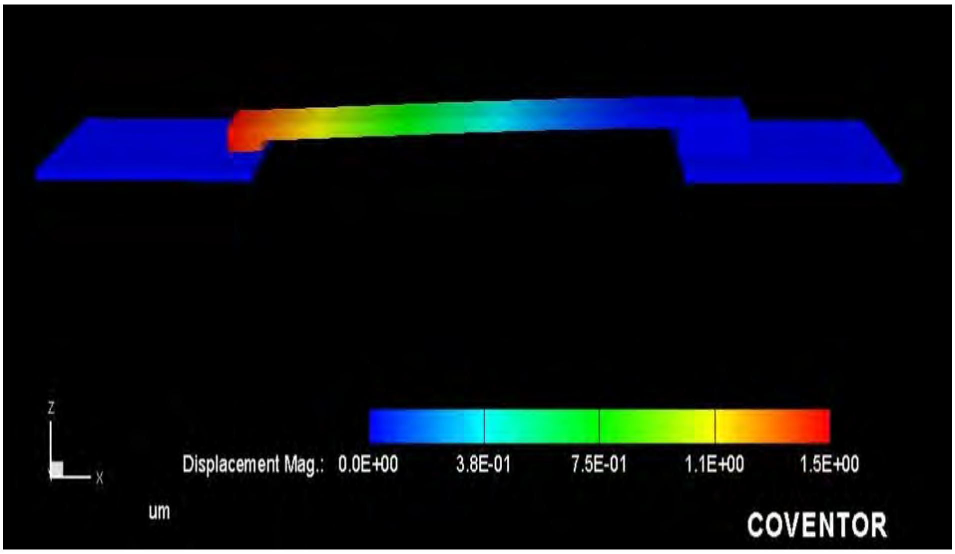

Figure 4.4. Design of MEMS switch in CoventorWare

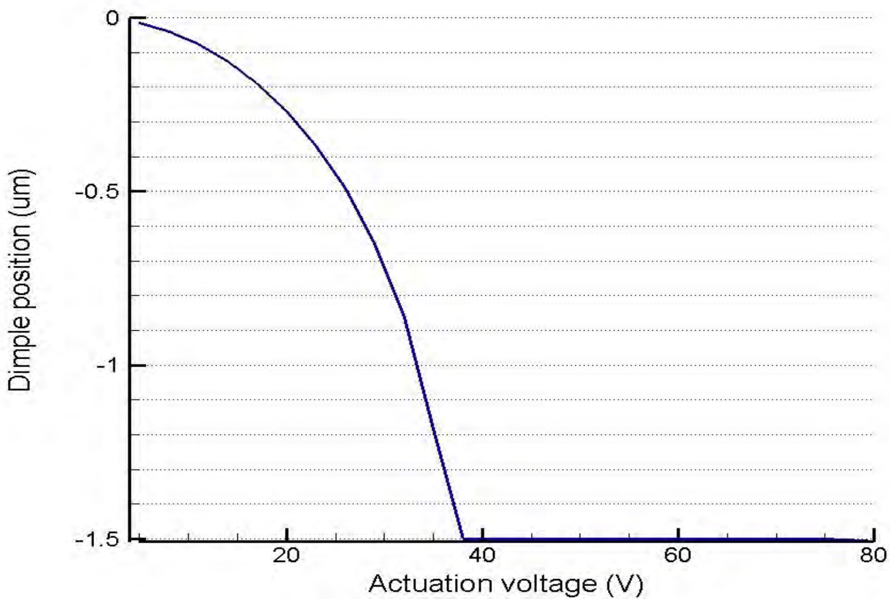

Figure 4.5. Simulated actuation voltage of RF MEMS switch by CoventorWare

The broadband microstrip-to-CPS transition [156] is employed to feed the printed dipole antenna as well as provide a solution to dc biasing. The transition performs field rotation and impedance matching (shown in figure 4.6). This radial stub behaves as an open circuit at the peripheral of its arc portion. This introduces a virtual short at the junction of the microstrip-to-CPS transition. The even-mode electric field under the microstrip line couples to the virtual short and experiences a 90 rotation. The odd-mode field of the CPS is then established after the ground plane truncation. In addition, three microstrip impedance transformation sections are used to match the impedance of the microstrip line and CPS line.

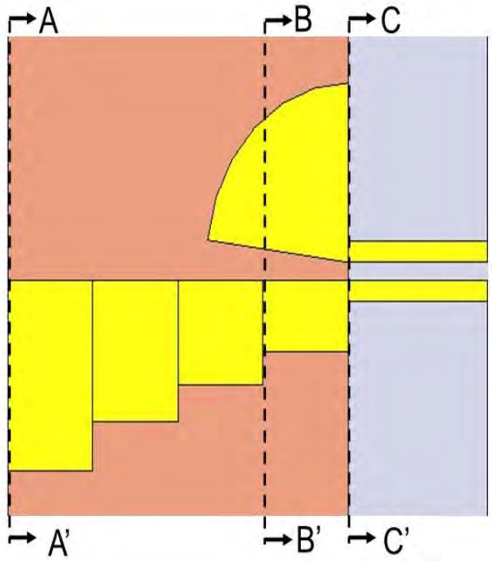

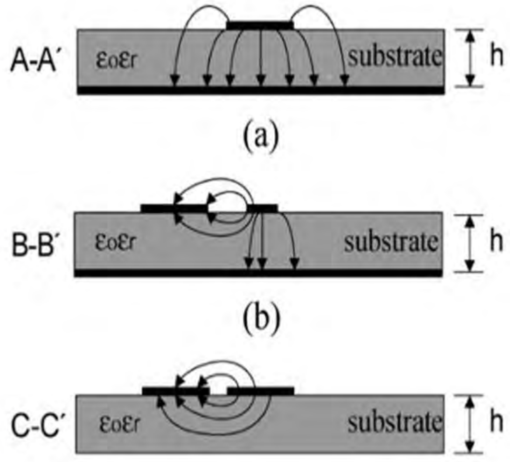

(a) **(b)**

Figure 4.6. (a) Configuration of the microstrip-to-CPS transition and (b) cross-sectional view of the electric field distribution

4.1.3. RESULTS

The antenna was analyzed using Ansys HFSS [157], which is based on the frequency-domain finite element method. Figure 4.7 presents the antenna reflection coefficients when all the six RF MEMS switches are in the 'ON' or 'OFF' state. Frequency switching is clearly observed. In each band, the bandwidth with good impedance matching ($|S11| \leqslant -10$ dB) is sufficiently large to cover the 60 GHz band and E-band. In the same figure, the results with the biasing line are also shown. It is observed that the operating frequency in the lower band is slightly shifted towards lower frequency by the presence of the biasing line. This is due to the fact that the RF current can flow up to the far end of the dipole when the RF MEMS switches bridge the gap ('ON' state). Due to the non-perfect RF chocking capability provided by the silicon chromium biasing lines, a small part of the current will be induced on the biasing lines and make the dipole longer. In the 'OFF' state, however, the RF current is blocked due to the perfect isolation provided by the RF MEMS switches.

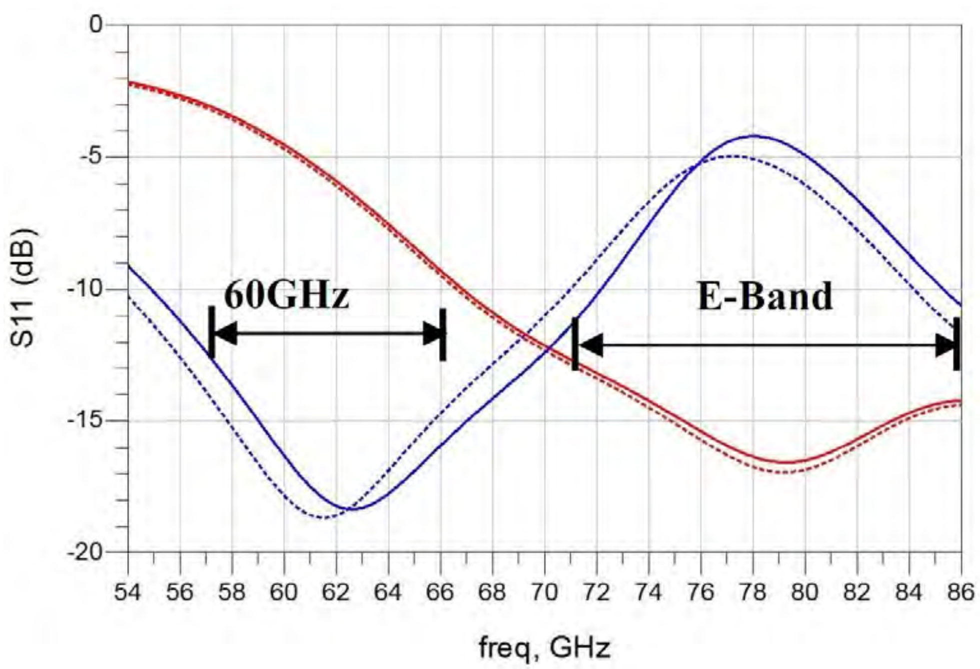

Figure 4.7. Comparison of the antenna reflection coefficient in lower band (blue curves) and higher band (red curves). Solid line: without resistive biasing line. Dashed line: with the resistive biasing line.

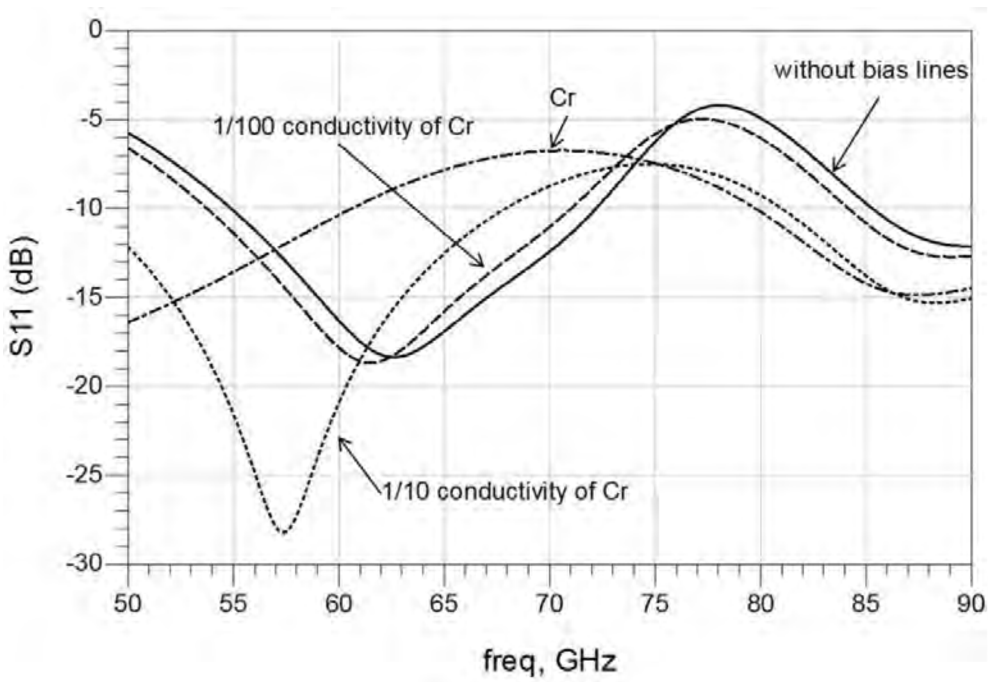

Figure 4.8. Effect of the biasing line material conductivity on the antenna reflection coefficient.

The effect of biasing line on the antenna reflection coefficient is studied by choosing different resistivity values of the lines. It is shown in figure 4.8 that when the conventional chromium is used for the biasing line material, the antenna reflection coefficient is dramatically affected. This effect becomes smaller when the resistivity is increased by 100 times than that of chromium (sheet resistance of 13.16 ohm/square). And the reflection coefficient will get closer and closer to the desired result as the resistivity get larger and larger. Thus, the silicon chromium [158] high resistive material is proposed for the biasing line material for the antenna.

In figure 4.9, the antenna radiation patterns in the two principle planes (E-plane: y-x plane and H-plane: y-z plane in figure 4.1) are shown at the central frequency of lower band (60 GHz) and two frequencies (73 and 83 GHz) in the higher band. Clearly, end-fire pattern is obtained. The main-beam deviation from the boresight direction in E-plane can be reduced by changing the ground plane size. In figure 4.10, the antenna realized gain is presented in the lower and higher bands. The antenna exhibits small gain variations from 5.5 to 6.7 dB in the lower band and from 6.5 to 8.1 dB in the higher band. These results are obtained by using gold as the material for the antenna metallization and RF MEMS switch fabrication. Extra losses may be introduced in the RF MEMS fabrication processes and affect the antenna gain performance.

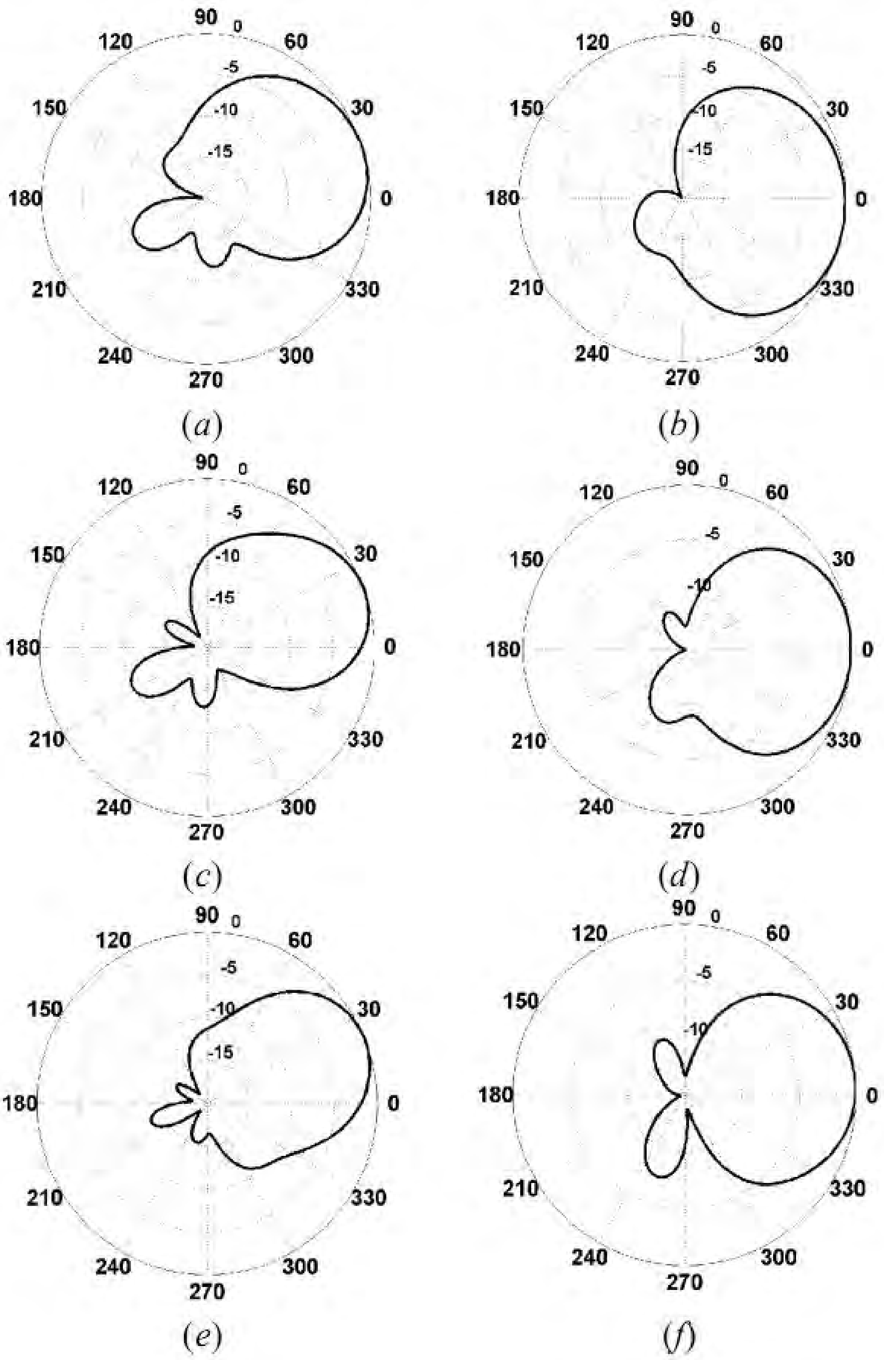

Figure 4.9. Antenna radiation patterns: (a) E-plane at 60 GHz. (b) H-plane at 60 GHz. (c) E-plane at 73 GHz. (d) H-plane at 73 GHz. (e) E-plane at 83 GHz. (f) H-plane at 83 GHz.

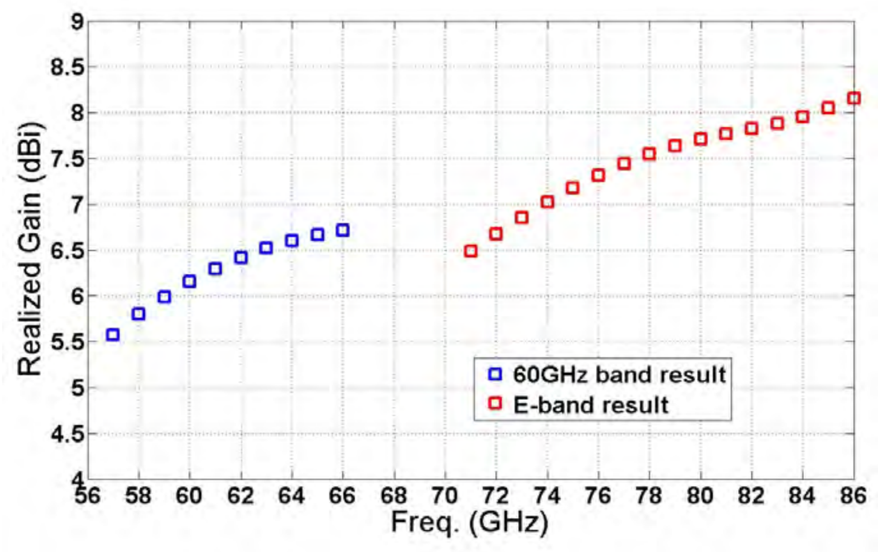

Figure 4.10. Antenna realized gain in the lower and higher frequency bands for the design including the biasing network.

4.1.4. CONCLUSION

A new RF MEMS-integrated millimeter-wave frequency reconfigurable quasi-Yagi antenna is proposed. The operation frequency of the antenna is switchable between the millimeter wave 60 GHz WPAN band (57-66 GHz) and E-band (71-86 GHz) by actuating of the RF MEMS switches employed on the driven and director dipole elements. The end-fire radiation pattern of the Yagi antenna is maintained in both two-bands. The antenna shows a small gain variation from 5.5 to 6.7 dB in the lower band and from 6.5 to 8.1 dB in the higher band. A resistive biasing configuration using silicon-chromium thin film is proposed. Simulation results have shown that it has small effect on the antenna reflection coefficient when the surface resistance is greater than 13.16 ohm/square. In view of the mechanical nature of the switch component, the antenna is expected to have a high IIP3 value, which is desirable for reconfigurable antennas.

4.2. RF MEMS-INTEGRATED FREQUENCY RECONFIGURABLE QUASI-YAGI FOLDED DIPOLE ANTENNA

A RF MEMS integrated frequency reconfigurable quasi-Yagi folded dipole antenna is presented in this section. The operating frequencies of the antenna are interchangeable between the millimeter wave WPAN band (57 - 66 GHz) and E-band (71 - 86 GHz). The operation principle is very similar to the antenna demonstrated in last section. The tuning is achieved by electronically adjusting the effective electrical length of the folded dipole driver and the director element by employing RF MEMS switches. This work was a collaboration with postgraduate student Eugene Siew. We designed and optimized the antenna structure.

4.2.1. INTRODUCTION

In the today's communications systems, it is very much desirable for antennas to operate between the unlicensed WPAN spectrum (57-66 GHz) and the light licensed E-band spectrum (71-86 GHz). One reason for its increasing popularity is due to its shorter wavelengths, these bands permit the use of smaller size antennas to achieve the same high directivity and high gain when compare to antennas that operate in the lower bands. To be able to fully utilize both the WPAN and E-Band spectrum in a single wireless platform, the antennas need to cover multiple frequency bands. While multiband and wideband antennas are potential candidates to achieve this, frequency reconfigurable antennas [159-160] are usually employed due to their better noise rejection capability which greatly reduces the filter requirements of the front-end circuits.

Printed quasi-Yagi antennas have received considerable attention due to their low cost, high radiation efficiency, modest gain [161-162], ease of fabrication and integration with MMICs. So far they have been mostly realized on high dielectric constant substrates with moderate thickness in order to excite the TE_0 surface wave along the dielectric substrate. The printed quasi-Yagi antenna realized using a high dielectric constant substrate is compact and is suitable for scanning arrays requiring an inter-element spacing of 0.5 λ_0. However, when fabricated on a low dielectric constant substrate, the length of the driver of a conventional quasi-Yagi antenna is increased, and it is difficult to achieve 0.5 λ_0 spacing between the elements required for scanning arrays. The research group in CSIRO Australia have proposed a compact, broadband design of a quasi-Yagi antenna suitable for fabrication on low dielectric constant substrates [154]. In the new antenna element, the half wavelength dipole driver of the standard quasi-Yagi antenna is replaced by a folded dipole. The folded dipole has better bandwidth characteristics than a single half wavelength dipole. Also, the length of the folded dipole is reduced compared to the conventional dipole and the new element is more suitable for applications requiring arrays of closely spaced quasi-Yagi antennas on low dielectric constant substrates. RF MEMS switch with multiple design merits [163-165] has been chosen to use in this structure.

4.2.2. ANTENNA DESIGN

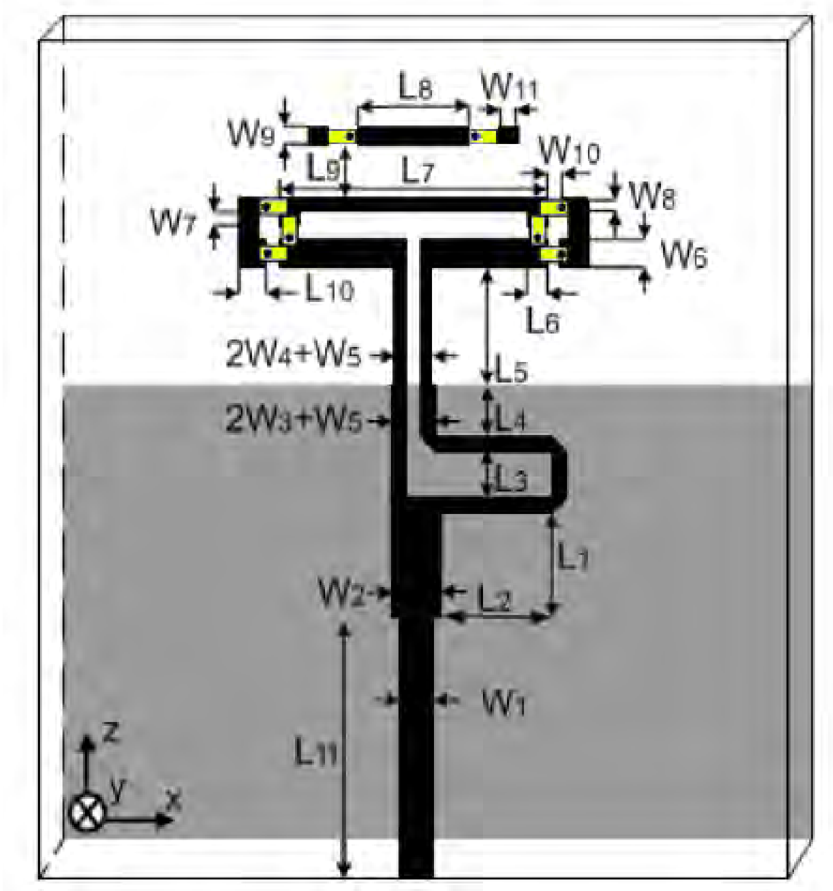

Figure 4.11. Schematic layout of the RF MEMS integrated frequency reconfigurable quasi-Yagi folded dipole antenna

Table 4.2. Antenna dimension parameters

Parameters	Value (μm)	Parameters	Value (μm)
W_1	180	L_1	540
W_2	260	L_2	600
W_3	80	L_3	240
W_4	60	L_4	260
W_5	80	L_5	600
W_6	147	L_6	105
W_7	70	L_7	1030
W_8	60	L_8	770
W_9	100	L_9	270
W_{10}	70	L_{10}	1065
W_{11}	105	L_{11}	1200

The layout of the proposed reconfigurable antenna is shown in figure 4.11 followed by its dimensions in table 4.2. The antenna element is printed on a low-loss Quartz substrate (ε_r =3.75, thickness h = 0.254 mm, tanδ = 0.0004), on which the RF MEMS switches are integrated. The top side of the substrate consists of a microstrip feeding line, a broad-band microstrip-to-CPS balun, a folded dipole driven element and a parasitic dipole element as a director. The bottom side is a truncated ground plane, which serves as a reflector element for the antenna. The combination of the parasitic director, the driven element and the reflector direct the radiation of the antenna toward the end-fire direction. It is shown in the parametric sweep that the length of the folded dipole driver L_7, the length of the director L_8, and the ratio of the upper strip and lower strip width W_6 / W_8 are important design parameters of the quasi-Yagi folded dipole antennas.

A total of eight RF MEMS switches (6 horizontal and 2 vertical) are used in this antenna. When all vertical switches are closed and all horizontal switches are opened, the length of the folded dipole is about 2×($L_7 + W_7$) and the length of the director is L_8. Both the folded dipole and director are shorter in length, thus the antenna resonates at a higher operating frequency band (denoted as State I). When all horizontal switches are closed and all vertical switches are opened, longer folded dipole element and director element are obtained. The length of the folded dipole is 2×($L_7 + L_{10} + W_{10} + W_7$) and the length of the director is L_8 + 2×($W_{10} + W_{11}$), which causes the antenna to resonate at a lower operating frequency (denoted as State II).

4.2.3. RESULTS

The antenna performance was analyzed using the frequency domain finite element method in Ansys HFSS. By controlling the RF MEMS switches, the resonant frequency is switched between WPAN band to the E-band. To understand our proposed RF MEMS reconfigurable antenna and the effect of RF MEMS switches, two non-reconfigurable antennas one operates at WPAN band and the other operates at E-bands are designed. They are used as benchmarks for the proposed reconfigurable antenna. Figure 4.12 presents the reflection coefficient of the reconfigurable antenna in State I and State II and the two benchmark antennas.

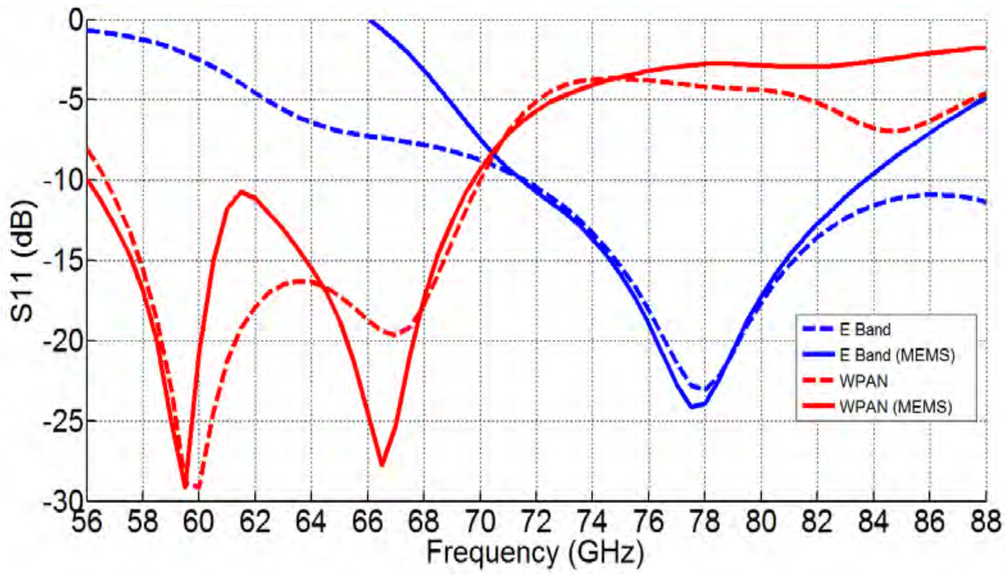

Figure 4.12. Comparison of the antenna reflection coefficient in upper band (blue curves) and lower band (red curves). Solid line: quasi-Yagi folded dipole antenna with RF MEMS switches integrated. Dashed line: quasi-Yagi folded dipole antenna without RF MEMS switches.

The simulation shows that the reconfigurable antenna achieves similar bandwidth in each band compared with the corresponding benchmark antennas. In both states, good impedance matching were achieved (|S11| < -10dB). It could be noticed that the introduction of RF MEMS switches to the reconfigurable antenna has only worsen the in-band reflection coefficient while enhancing the out-of-band rejection in both states.

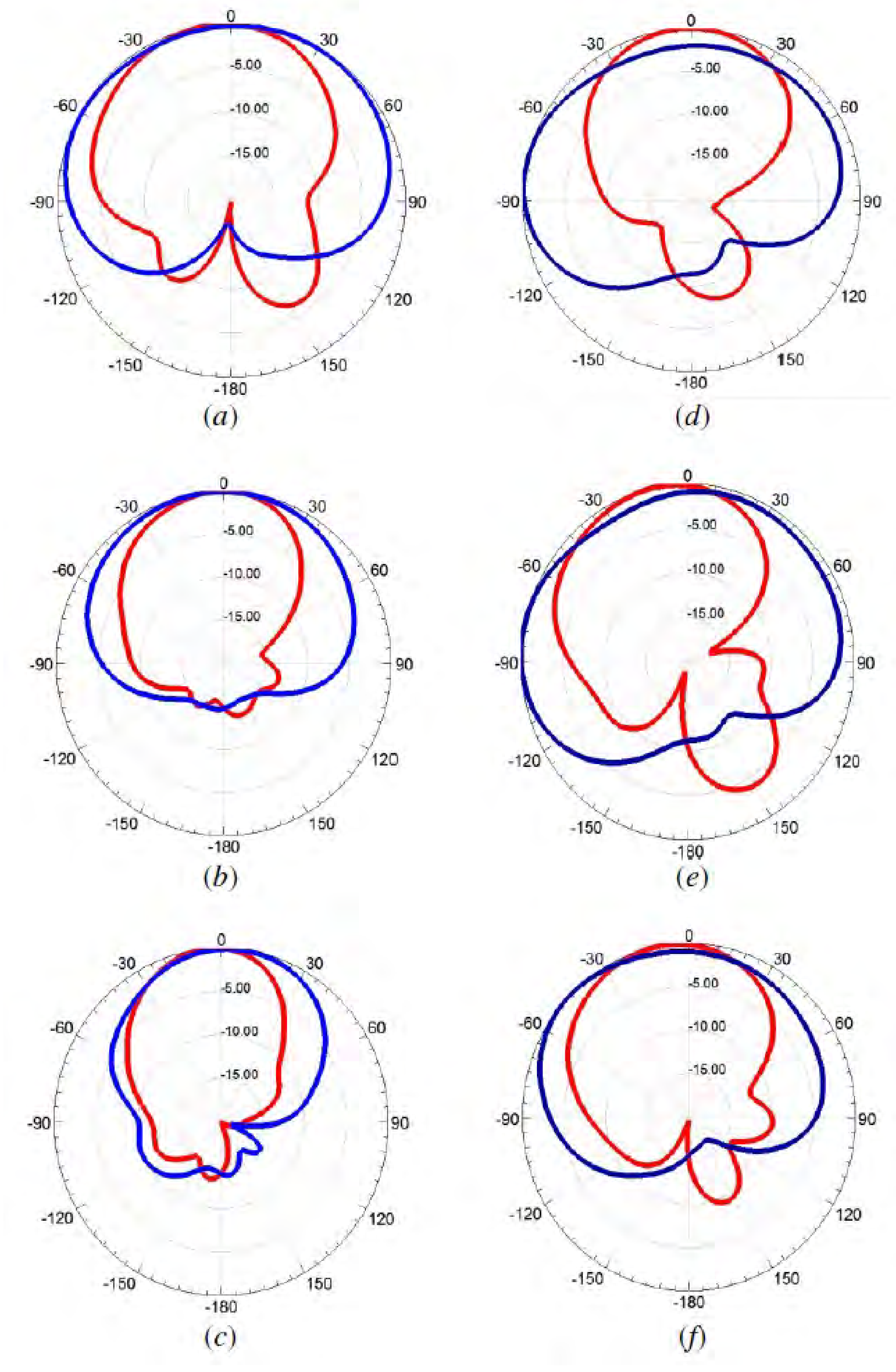

Figure 4.13. Antenna radiation patterns in both E-plane (red) and H-plane (blue): (a)71GHz (b)78.5GHz (c)86GHz (d)57GHz (e)61.5GHz (f)66GHz.

Figure 4.13 shows the normalized radiation patterns in E-plane and H-plane of the reconfigurable antenna. For State I, the radiation plots are as follows: Fig. 4 (a), (b) and (c) show the radiation pattern at 71, 78.5, and 86 GHz respectively. For State II, the radiation patterns are presented in Fig. 4 (d), (e), (f) at the frequencies 57, 61.5, and 66 GHz, respectively. Clearly, the desired end-fire pattern is obtained.

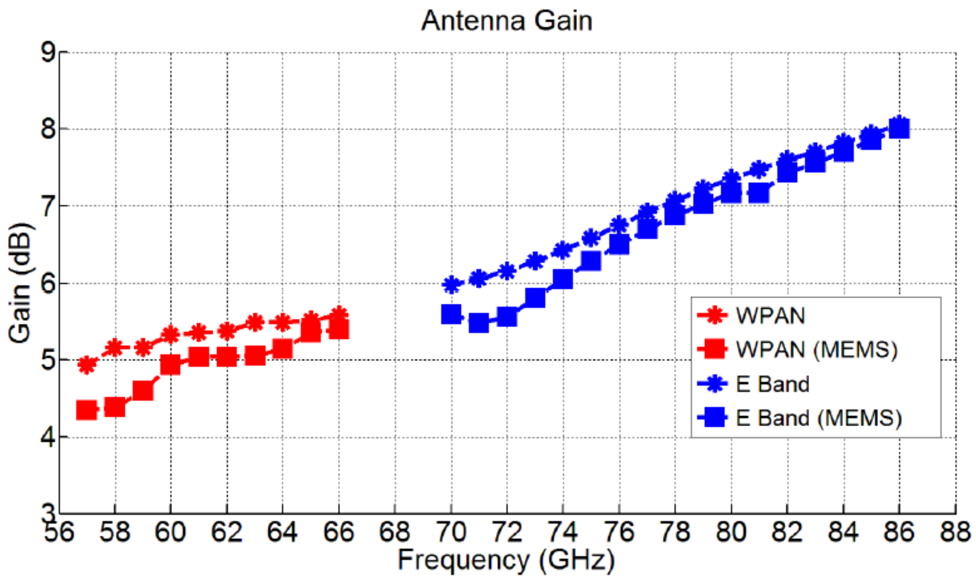

Figure 4.14. Antenna realized gain in the WPAN band and E-band.

The realized gain of the proposed antenna is presented in figure 4.14 for both lower and upper bands and is compared with the benchmark antennas. The antenna gain variation is from 5.5 to 8.0 dB in the upper band and from 4.3 to 5.2 dB in the lower band. It only exhibits maximum 0.5 dB less gain compared with the benchmark antennas. However, the presented results did not include losses due to RF MEMS contact resistance which arises from several factors such as the size of the contact area, the mechanical force applied, and the quality of the metal to metal contact [166]. These extra losses introduced are likely to affect the realized gain of the antenna.

4.2.4. CONCLUSION

In this section, a MEMS integrated frequency reconfigurable quasi-Yagi folded dipole antenna is reported. In this design, RF MEMS contact type switches are used. Two separated frequency bands, WPAN band (57 - 66 GHz) and E-band (71 - 76 GHz), are achieved with this reconfigurable antenna. Two individual folded dipole Yagi antennas were also designed for comparison. Simulation results show that our RF MEMS integrated reconfigurable antenna only exhibits maximum 0.5 dB gain loss in comparison. The gain variation is from 4.3 to 5.2 dB in the WPAN band and from 5.5 to 8 dB in the E-band, respectively. End-fire radiation patterns are realized at different frequencies across the two frequency bands.

CHAPTER 5

PATTERN RECONFIGURABLE ANTENNAS

In this chapter, a comparison between different microstrip-to-CPS transitions is presented first. It not only demonstrated some types of microstrip-to-CPS transition are not suitable for balanced applications such as dipole or Yagi antenna, but also proposed a new testing standard for this type of transition design. The inspiration drawn from this comparison has led to a novel pattern reconfigurable quasi-Yagi antenna design. The details are provided in the following section. Then a pattern reconfigurable spiral antenna design is illustrated.

5.1. COMPARISON OF 60 GHZ QUASI-YAGI ANTENNAS USING DIFFERENT MICROSTRIP-TO-CPS TRANSITIONS

5.1.1. INTRODUCTION

The coplanar stripline (CPS) is a balanced uniplanar transmission line with the advantages of compact size, ease of mounting lumped components in series or shunt configuration, and low discontinuity parasitics. The uniplanar characteristics of the CPS also eliminate the need for a via-hole that introduces parasitic effects. Based on the above advantages, the CPS has found many applications in microwave circuits such as filters, mixers, phase shifters, and dipole antennas. On the other hand, since the microstrip line is still one of the most popular transmission lines, the microstrip-to-CPS transition with wide bandwidth, low loss, and simple structure is required in order to fully take advantage of these two transmission lines.

Several microstrip-to-CPS transitions have been reported. The transition based on the mode conversion has shown a 3 dB back-to-back insertion loss bandwidth of 59% [167]. As an improved design of [167], a 3 dB back-to-back insertion loss bandwidth of 68% is achieved [168]. In addition, the transition using the coupling method shows a 2.4 dB back-to-back insertion loss bandwidth of 18% [169]. The above transitions, however, are only suitable for narrow-band applications. Furthermore, they are all built on high dielectric-constant substrates (ε_r >10) for a low characteristic impedance of the CPS, and easy matching to a 50 Ω microstrip line. Since the high dielectric-constant substrates are suitable for circuit design instead of the antenna design, using such transitions to feed antennas will degrade the antenna performance. Recently, the microstrip-to-CPS transitions on low dielectric constant substrates have been reported with a 3 dB back-to-back insertion loss bandwidth covering from 1.3 to 13.3 GHz (1:10.2) [170] and an 1 dB back-to-back insertion loss covering from 6.5 to 13.8 GHz [171].

In this section, microstrip-fed quasi-Yagi antennas with two different microstrip-to-CPS baluns [172-173] were designed, simulated and compared in 60 GHz band. This research is an important supplement of our preceding work [174] to demonstrate that the phase tuning performance of the balun can severely affect the antenna directivity in frequency band as high as 60 GHz spectrum. Furthermore, a new practical testing method is proposed along with back-to-back insertion loss as a basic standard for any type transmission line to CPS transition.

5.1.2. ANTENNA DESIGN

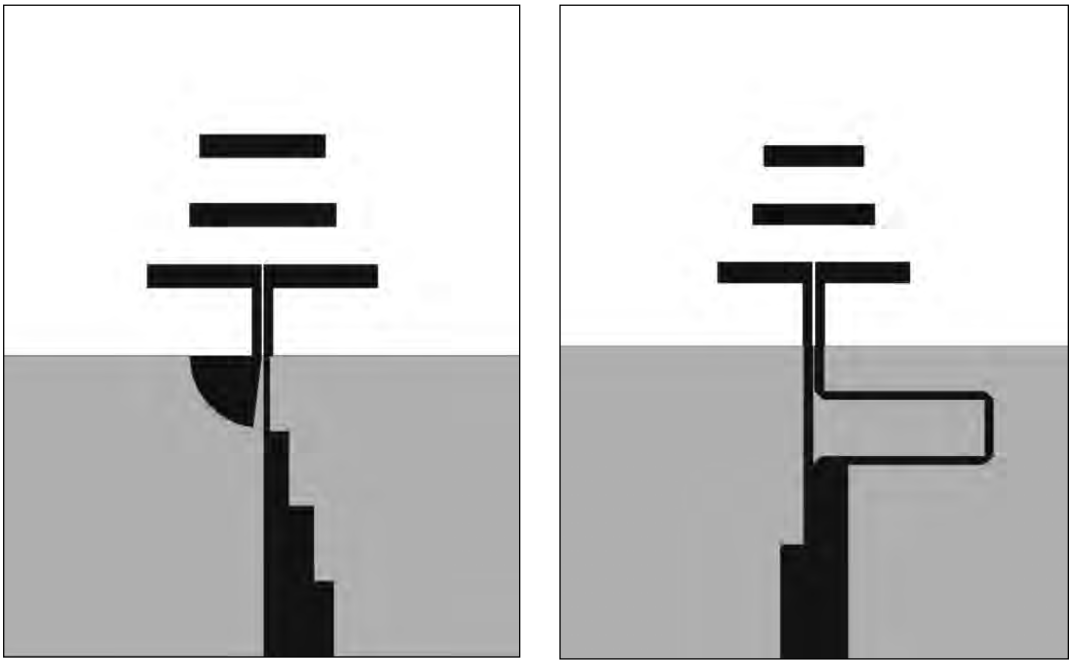

(a) (b)

Figure 5.1. Schematic layouts of the quasi-Yagi (a) antenna I and (b) antenna II

The configurations of the designed antennas are presented in figure 5.1. The antennas and feeding structures are built on low-loss quartz substrates (ε_r = 3.75, tanδ = 0.0004, thickness = 0.254 mm). Both of designs have the top metallization consisting of two parasitic director elements, a dipole component and a microstrip-to-CPS transition. The reflector elements are substituted by truncated ground planes printed on the back side of the substrate. Antenna I employed the radial stub based transition while the delay line type balun is used in the antenna II. In radial stub transition (figure 5.1 (a)), the electric field in the microstrip line is perpendicular to the electric field in the CPS, so an electric-field rotation of 90° is needed. A radial stub or a quarter-wavelength rectangular open stub can be used for the field rotation. Ideally, the signal on two striplines should have a phase difference of 180° after rotation. To match the impedances of microstrip line and coplanar striplines, a Chebyshev three-section transformer is used. In delay line transition (figure 5.1(b)), a delay line is employed for a phase shift of 180° so the electric field can be rotated 90° after the truncated ground plane disappear.

5.1.3. SIMULATION RESULTS

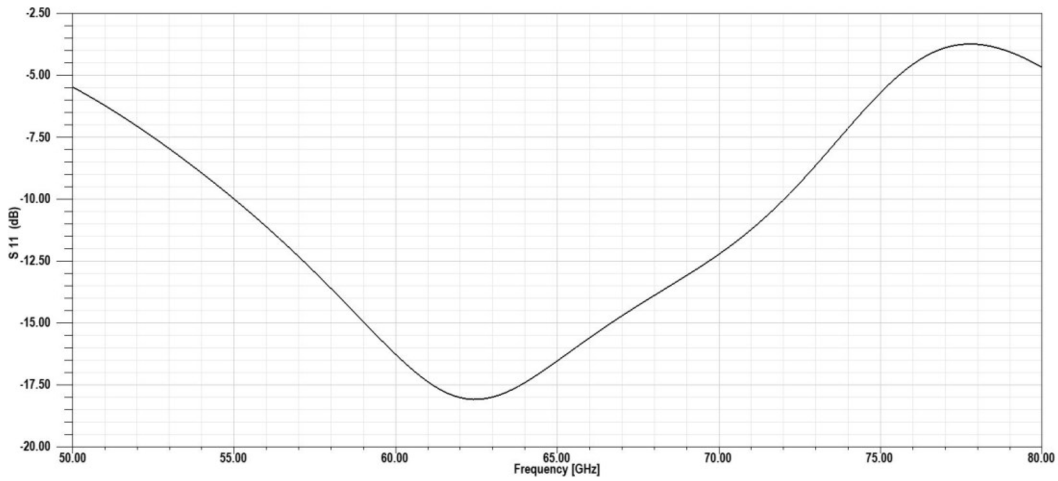

(a)

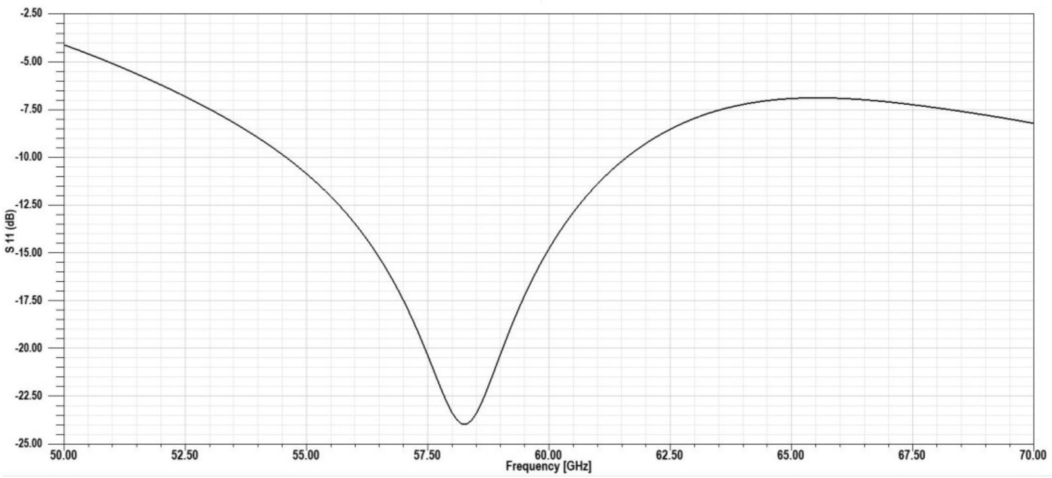

(b)

Figure 5.2. Antenna reflection coefficient in 60 GHz spectrum for (a) antenna I and (b) antenna II

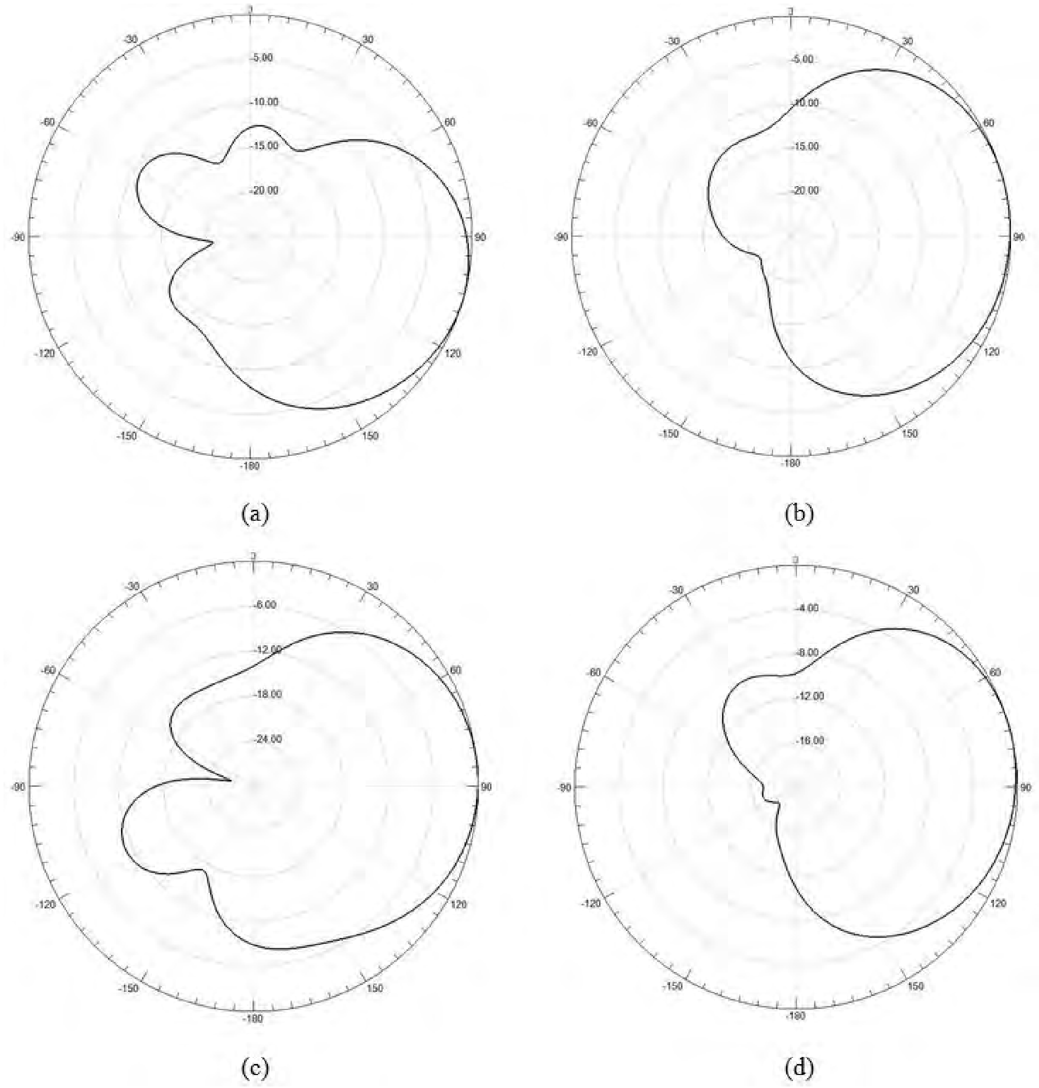

Figure 5.3. Antenna radiation patterns: (a) E-plane at 60 GHz for antenna I. (b) H-plane at 60 GHz for antenna I. (c) E-plane at 60 GHz for antenna II. (d) H-plane at 60 GHz for antenna II.

The two antennas were analyzed using ANSYS HFSS software. The reflection coefficient S11 for antenna I and antenna II are illustrated in figure 5.2 (a) and (b). As can be seen antenna I has much broader bandwidth when compared to antenna II. This is due to the fact that the delay line balun can only target at one single frequency to obtain a precise 180 degrees shift of the signal phase to excite the odd mode transmission on coplanar striplines. In figure 5.3, the antenna radiation patterns in the two principle planes are shown at 60 GHz. End-fire radiation pattern is clearly observed for antennas II. The directivity of antenna I is shifted in E-plane due to fact that the radial stub balun cannot provide 180 degree phase change at 60 GHz band. The parametric sweep has been done and the 180 degree phase change cannot be achieved because of the intrinsic discontinuity. Therefore it is not suitable for loads that require balanced CPS input such as dipole or quasi-Yagi antenna.

5.1.4. CONCLUSION

This research has demonstrated that the radial stub based microstrip-to-CPS transition can affect the directivity of printed quasi-Yagi antenna operated in 60 GHz due to it cannot provide 180 degree phase change. Many new microstrip-to-CPS transitions utilize discontinuous structures. One problem of these structures is that the phase delay between two coplanar striplines cannot be precisely controlled. And these papers all emphasize the insertion loss they achieved but there are no demonstration of stripline phase balance. So a new testing method is proposed in this paper which uses Yagi antenna connected directly to the transition to test the phase balance. If the radiation pattern shift from the desired end-fire direction, the structure under test should not be used for applications require balanced input. The directivity problem unveiled in this section shed light on the possibility of using phase unbalanced transition to control the directivity of Yagi antenna forming pattern reconfigurable antenna.

5.2. PROOF FOR PATTERN RECONFIGURABILITY OF 60 GHz QUASI-YAGI ANTENNA

This section demonstrates the possibility of designing pattern reconfigurable quasi-Yagi antenna. Adjusting the length of dipole arms and delay line, the E-plane radiation direction can be steered from -20° to +20°, without compromising the realized radiation gain or shifting the operating spectrum at 60GHz band. In this part, nine individual Yagi antennas with different beam directions are designed. They all have bands centered at 60GHz, with wide bandwidths covered from 57 GHz to 66 GHz. And five of them are fabricated and measured. The experimental results match well the predicted ones and demonstrate that the radiation beam direction of quasi-Yagi antenna can be freely shifted.

5.2.1. INTRODUCTION

Printed antennas such as the quasi-Yagi antenna are attracting a lot of attention for their potentials in applications demanded of broadband. They offer compact size and serve as end-fire directional antennas. Quasi-Yagi planar antenna have been extensively used in the wireless communications due to its outstanding features including: light weight, low cost and ease of fabrication [154].

Nowadays, enormous multimedia applications call for wireless transmission at gigabit-per-second, or even a faster rate over a short distance. For example, the wireless gigabit Ethernet standard requires 1.25 Gb/s, wireless high speed download and high definition video streaming needs 2-20 Gb/s to satisfy their customers. These data rates are usually hard to be accommodated in the traditional frequency bands. However, the wide unlicensed frequency band around 60 GHz enables short-range communications with such high data rates [175-176]. A good candidate for the 60 GHz spectrum applications is Wireless Personal Area Network (WPAN) which provide short range (< 10 m), very high speed (> 2 Gb/s) multi-media data services to computer terminals and consumer appliances located in office area, rooms, hot spots and kiosks [177]. Another interesting concept for the 60 GHz band is the millimeter-wave identification (MMID) that can read batteryless wireless mass memories in a few seconds with high data rate [178].

Antenna reconfigurability provides the means to adapt antenna frequency, pattern and polarization to specific propagation environments in real time, leveraging antenna parameters to increase system performance [179-181]. In particular, pattern reconfigurable antennas can maneuver away from the noisy environment, improve security and save the power, all by pointing the radiation beam towards the specific customers [182]. These hallmarks used to be achieved with phased antenna arrays, which consume more surface area on substrate and are more complex to employ [183]. However, recent studies of reconfigurable antennas led to new solutions for this task [184-185].

In following section, nine individual antennas were designed with different dipole and microstrip-to-CPS transition delay line to operate in the same spectrum (57 GHz – 66 GHz WPAN band), while the beam direction in E-plane sweeping from -20° to +20° in 5° steps. Five of these antennas have been fabricated and measured to discover the real world performances. All designs use the same quarter wavelength matching network. Successful demonstration of reconfigurability will lead to the future integration of RF MEMS on a single device, to build pattern reconfigurable antenna (which can replace phased antenna arrays) to save space on the substrate, and to achieve lower energy consumption.

5.2.2. ANTENNA DESIGN

The configuration of proposed quasi-Yagi antenna is shown in figure 5.4, while its parameters are listed in table 5.1. The antennas' top metallization consists of a driven dipole, two parasitic directors and a microstrip-to-CPS transition. The backside truncated ground plane acts as a reflector element. The combination of the directors, driven dipole and the reflector forms a four element quasi-Yagi array which has an end-fire radiation pattern. These components are deposited and patterned with gold using surface micromachining technology. The elements and feeding structures are created on a low-loss quartz substrate with a thickness of 0.25mm and the relative permittivity of ε_r =3.75. The quartz substrate is chosen because it has a whole set of well-established fabrication processes to construct MEMS loaded pattern reconfigurable antenna in the future.

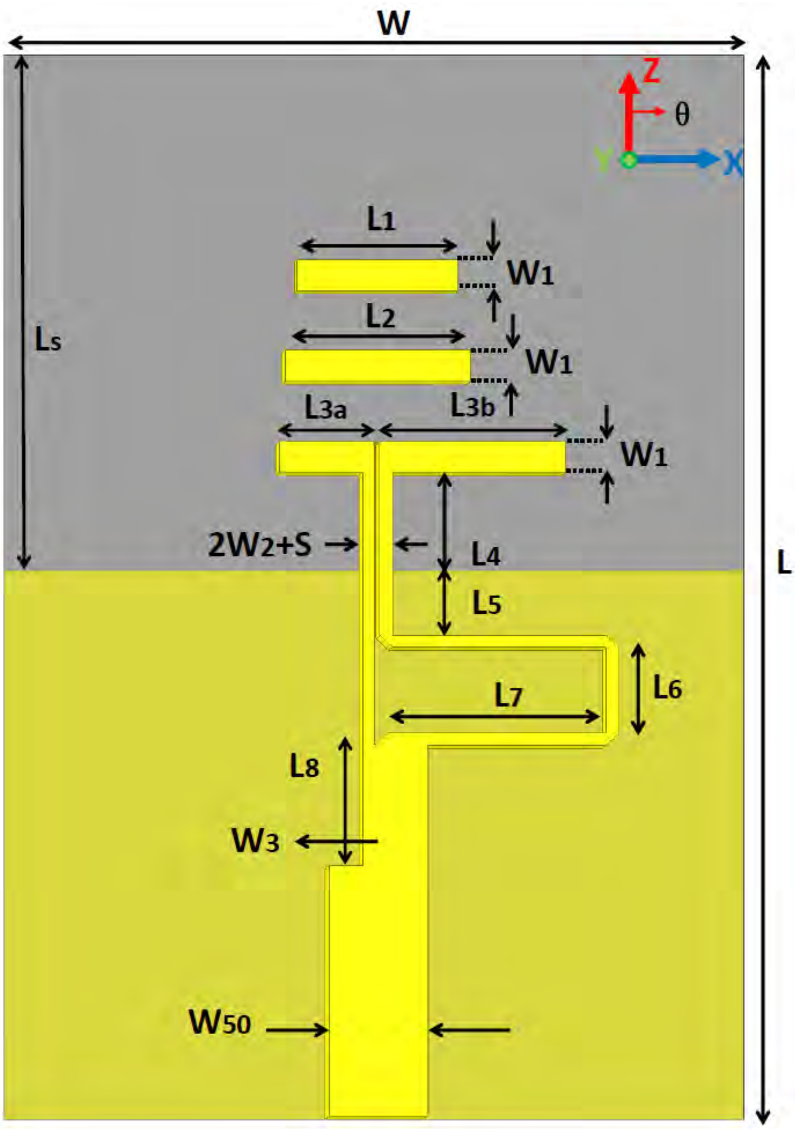

Figure 5.4. Schematic layout of the 60 GHz quasi-Yagi antenna

Table 5.1. Antenna dimension parameters (unit: µm)

L	W	L1	L2	L4
5740	4000	860	1000	550
L5	L6	L7	L8	Ls
400	500	1230	700	3000
W1	W2	W3	W50	S
180	70	350	530	24

The innovation of this design is to make dipole driven arms unsymmetrical. After many attempts, an important discovery has been made that when two driven dipole arms are fed out of phase (not exactly 180 degree), the radiation pattern will shift towards the arm on which that signal is delayed. By precisely tuning the length of two driven dipole arms L3a and L3b, and the microstrip-to-CPS transition delay line length L7, the radiation beam can be easily pointed toward the direction that system requires. Based on the simulation results, it has been found that when solely increase the left dipole arm L3a or the delay line L7, the radiation pattern will shift toward the left (figure 5.4) and the operating frequency will move to lower band; and when shorten the L3a or L7 the trend reverses. The results of varying the length of right arm L3b are quite different from the former two parameters; they only change the center frequency, but not the radiation direction. This is considered to cause by the coupling between the delay line and the right arm.

Based on the observations provided above, we can steer the beam at different directions respect to the end-fire direction in E-plane (z-x plane in figure 5.4) by changing the balun and left arm length, then compensate the frequency shifting by adjusting the right arm length. This is an innovative way to create pattern reconfigurable antenna: modifying the physical length of only two or all of these three parameters with RF MEMS switches, while maintaining the good impedance match and the directional radiation pattern. The H-plane (z-x plane in figure 5.4) radiation pattern will not be affected by the changes.

Nine antennas have been designed and simulated, to verify the ability of continuous sweep main beam direction θ from -20° to +20° (figure 5.4) in 5° increments, maintaining good frequency response at 60GHz band by adjusting only these three parameters. The details of the antennas are listed in the table below.

Table 5.2. Nine antennas' parameters

Angle (°)	-20	-15	-10	-5	0	+5	+10	+15	+20
L7 (μm)	1340	1230	1230	1230	1230	1230	1235	1150	1070
L3a (μm)	1070	1020	950	880	810	775	740	690	630
L3b (μm)	520	540	580	650	810	780	780	900	1020

5.2.3. SIMULATION RESULTS

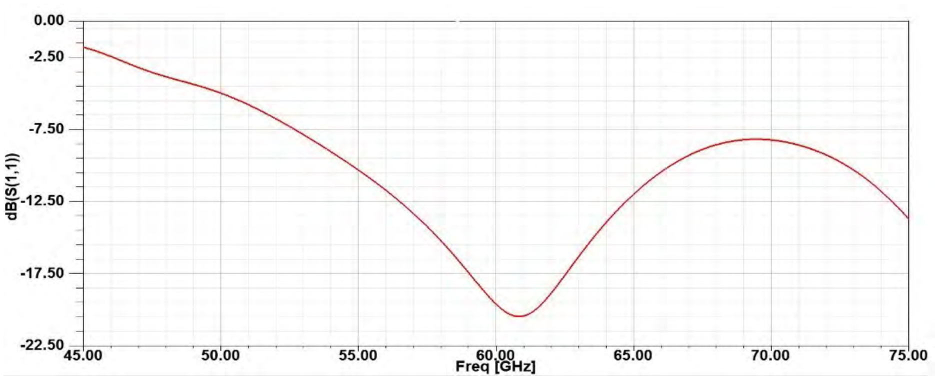

(1)

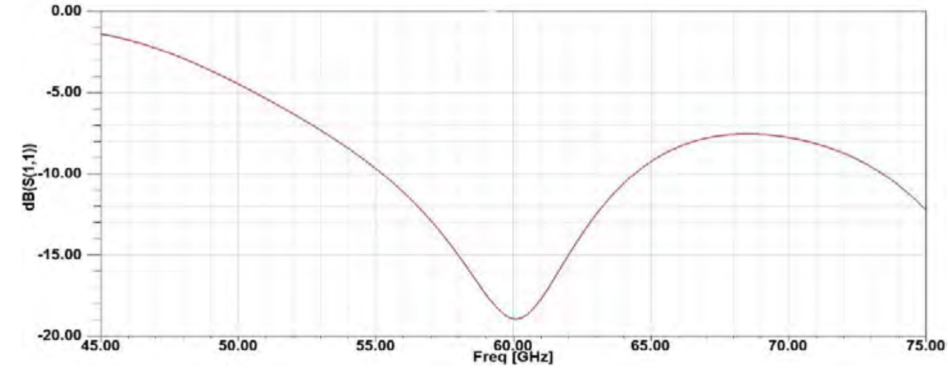
0.00
-5.00
-10.00
-15.00
-20.00
dB(S(1,1))
45.00
50.00
55.00
60.00
65.00
70.00
75.00
Freq [GHz]

(2)

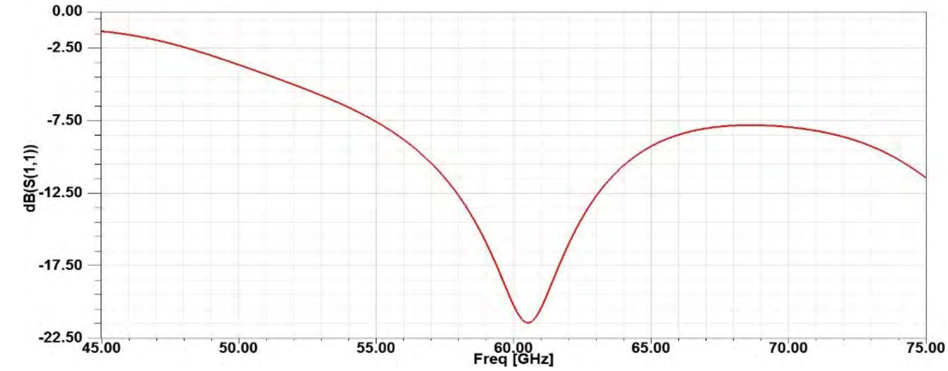
0.00
-2.50
-7.50
-12.50
-17.50
-22.50
dB(S(1,1))
45.00
50.00
55.00
60.00
65.00
70.00
75.00
Freq [GHz]

(3)

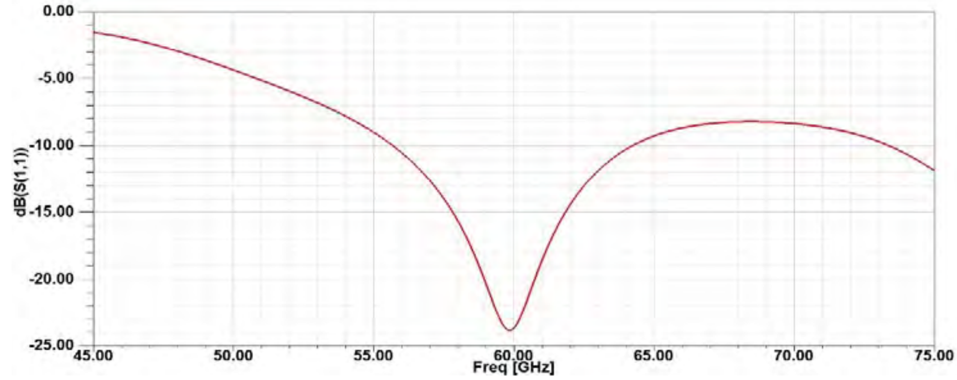
0.00
-5.00
-10.00
-15.00
-20.00
-25.00
dB(S(1,1))
45.00
50.00
55.00
60.00
65.00
70.00
75.00
Freq [GHz]

(4)

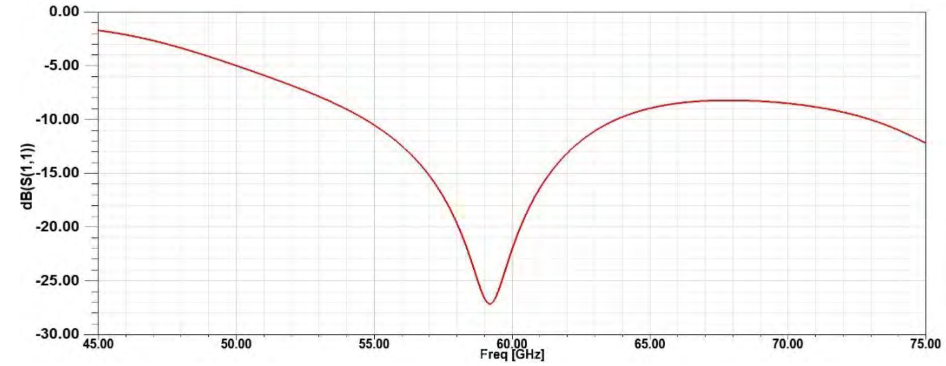
0.00
-5.00
-10.00
-15.00
-20.00
-25.00
-30.00
dB(S(1,1))
45.00
50.00
55.00
60.00
65.00
70.00
75.00
Freq [GHz]

(5)

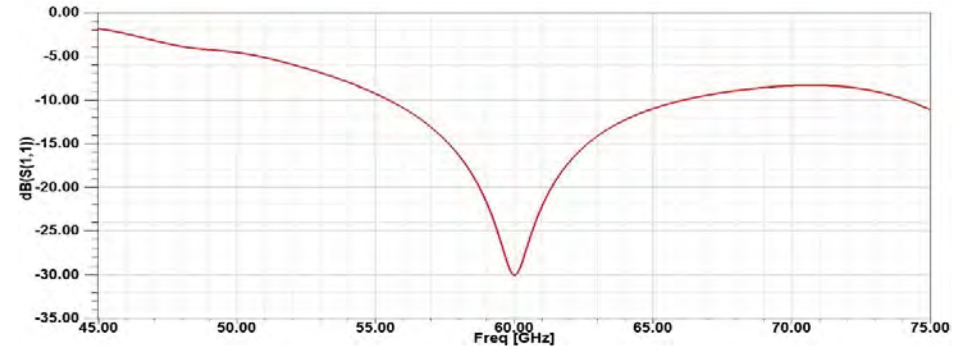

(6)

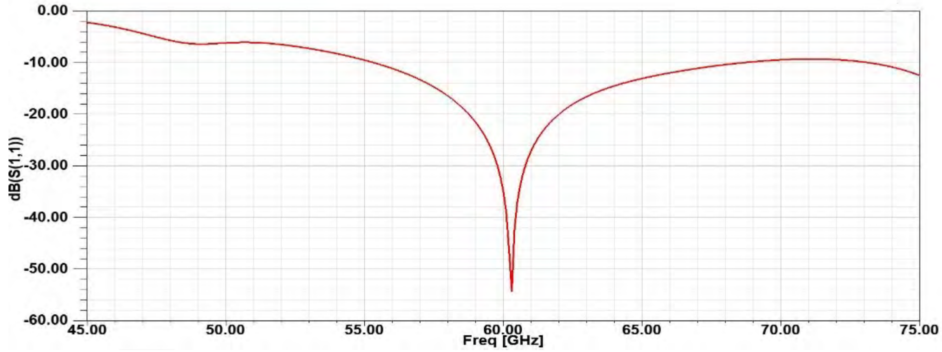

(7)

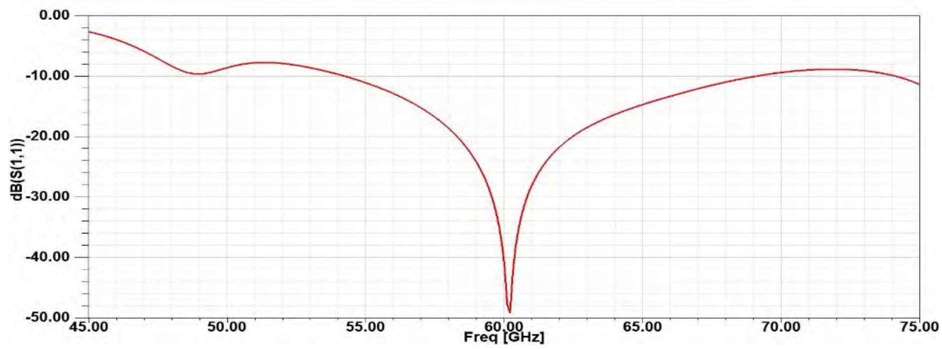

(8)

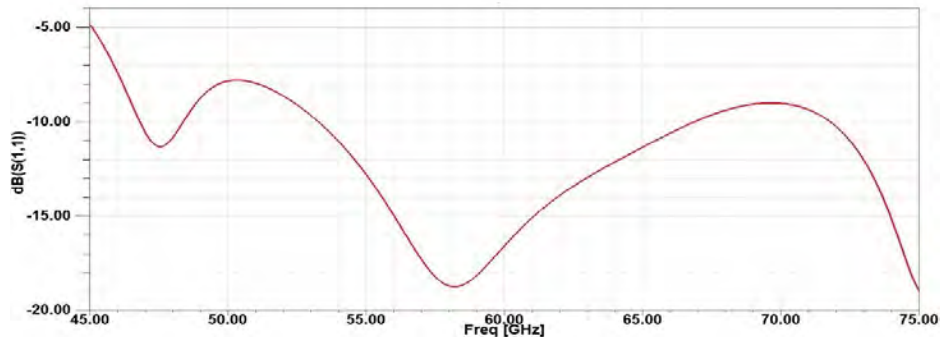

(9)

Figure 5.5. Simulated reflection coefficient vs. frequency (45GHz-75GHz) for nine antennas with radiation beam shift of: (1) -20°; (2) -15°; (3) -10°; (4) -5°; (5) 0°; (6) +5°; (7) +10°; (8) +15°; (9) +20°

Table 5.3. Simulated antenna center frequency

Angle (°)	-20	-15	-10	-5	0
Centre Freq. (GHz)	60.8	60.1	60.5	59.8	59.2
S11 (dB)	-20.45	-18.93	-21.42	-23.82	-27.13
Angle (°)	+5	+10	+15	+20	
Centre Freq. (GHz)	60.0	60.3	60.2	58.2	
S11 (dB)	-30.02	-54.28	-49.13	-18.73	

The antennas were analyzed using ANSYS HFSS. As can be seen in figure 5.5, all the antennas with the same director components and quarter wavelength matching network demonstrate good impedance matching with S11 < -18dB at the center frequencies of 60GHz, while the operating band covers from 57 GHz to 66 GHz.

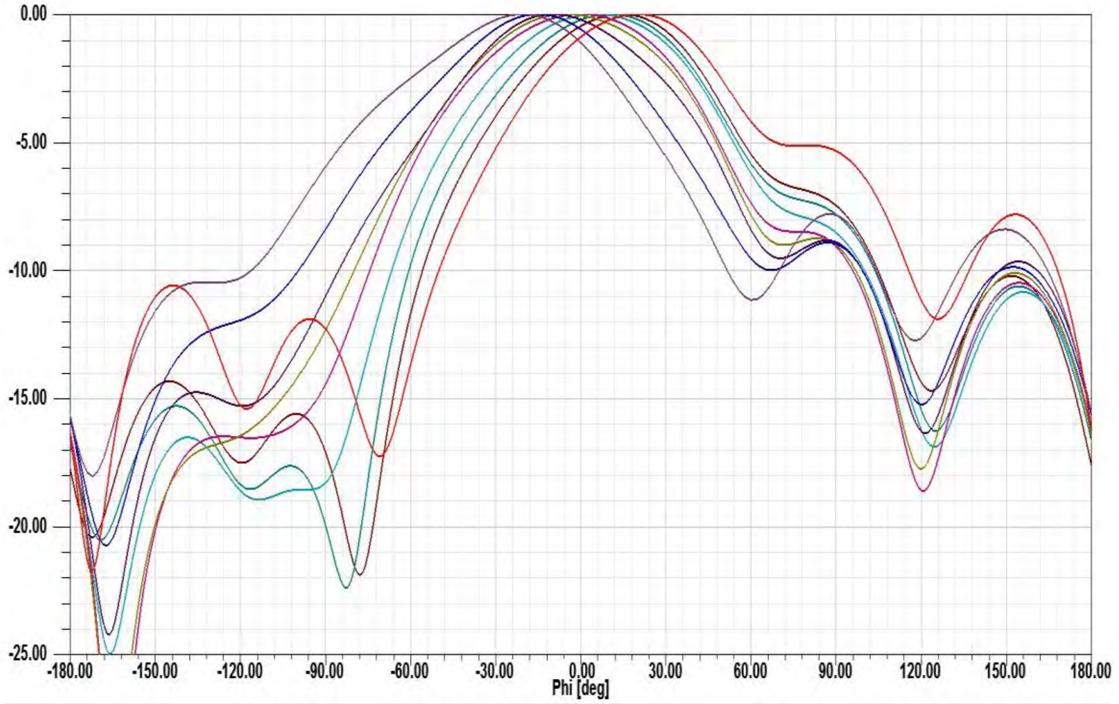

Figure 5.6. Simulated antenna E-plane radiation patterns, maximum beam direction steered from -20° to +20° at 5° steps (normalized gain)

Table 5.4. Simulated antenna realized gain

Angle (°)	-20	-15	-10	-5	0
Gain (dB)	5.82	6.21	6.36	6.359	6.417
Angle (°)	+5	+10	+15	+20	
Gain (dB)	6.57	6.762	6.821	6.529	

Figure 5.6 shows that the simulation results of E-plane radiation patterns are distributed exactly as we intended, the maximum radiation directions of nine quasi-Yagi antenna has been tune to -20° to +20° at 5° steps. The realized antenna gain is presented in the table 5.4. All the antennas achieve good radiation performance; the table exhibits small gain variations from 5.82 to 6.821 dB.

5.2.4. FABRICATION

Five antennas with radiation beam shift from -20° to +20° at 10° steps have been fabricated in Australian National Fabrication Facility (ANFF) lab in UNSW. Four pieces of wafer were fabricated, each contains nine antenna structures (for redundancy) and one back-to-back structure. Fabrication processes started with backside photolithography, where negative photoresist 2035 was used to pattern the truncated ground plane structure. Then 1μm of gold layer was deposited using Lesker thermal evaporator and lift-off the unwanted gold (figure 5.7). After that front side mask need to be aligned with the backside pattern and another photolithography was done to pattern the front side antenna and feed line structures. 1μm of gold film was deposited and lift-off to form the front side structure (figure 5.8). The wafer then need to be dice by DAD 3240 dicing saw with diamond blade specialized in cutting silica substrate. Finally the pin structure was diced using femtosecond laser cutting machine (figure 5.9).

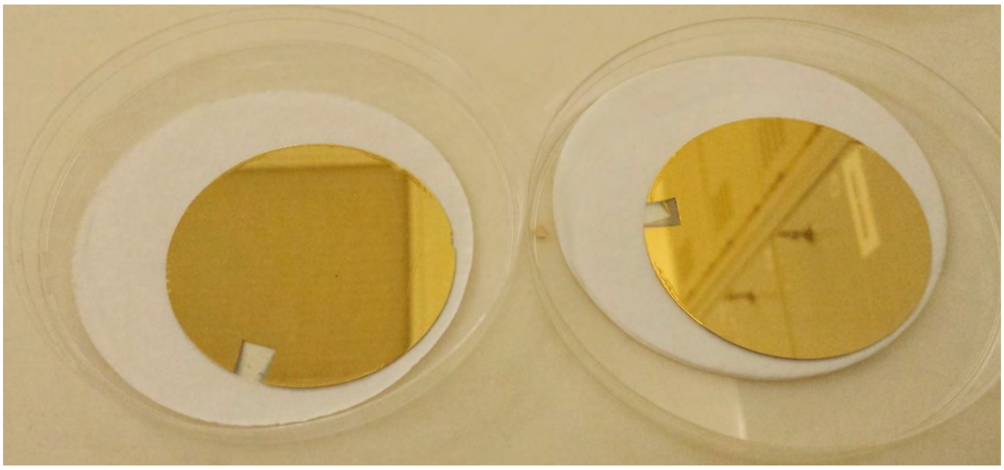

(a)

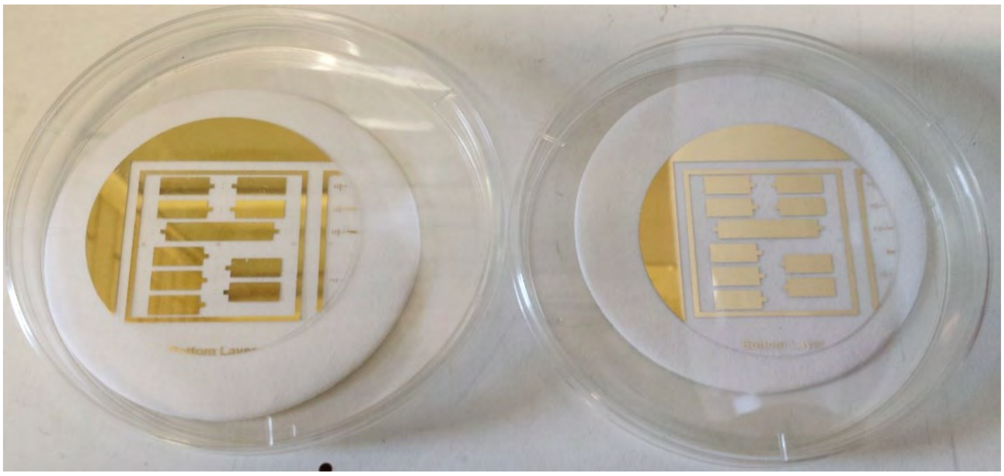

(b)

Figure 5.7. (a) Substrate with deposited gold layer and (b) backside gold pattern after lift-off

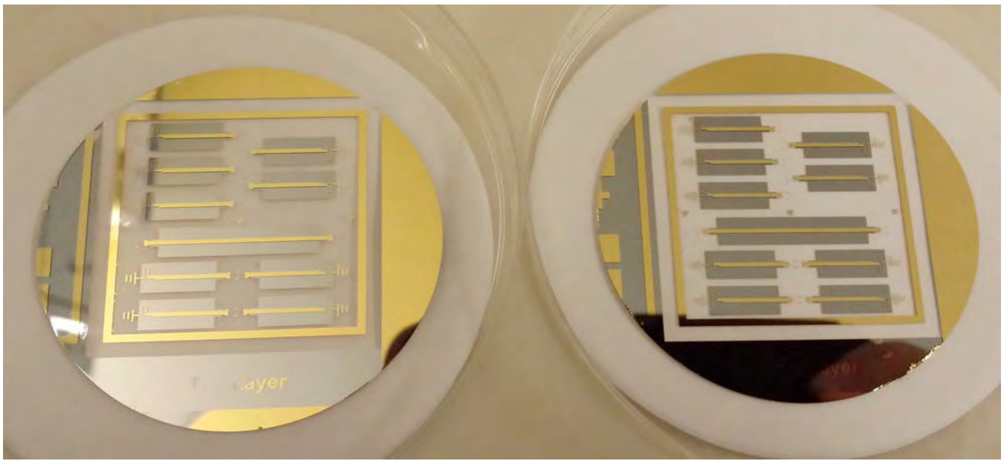

Figure 5.8. Substrate with two sides gold patterns

Figure 5.9. Backside of the structure after dicing

The antennas need to be bond to a microstrip-to-waveguide transition block then mounted on the positioner in the anechoic chamber in The Commonwealth Scientific and Industrial Research Organization (CSIRO) ICT Center. Epoxy was used for bonding the structures. Epoxy is best known as a type of durable glue that provides a high level of bonding properties that are far superior to most ordinary paste style glues. The antennas were assembled in CSIRO lab where the Epoxy was cured at 120°C to form a strong adhesion layer between gold ground plane and the brass transition block (figure 5.10).

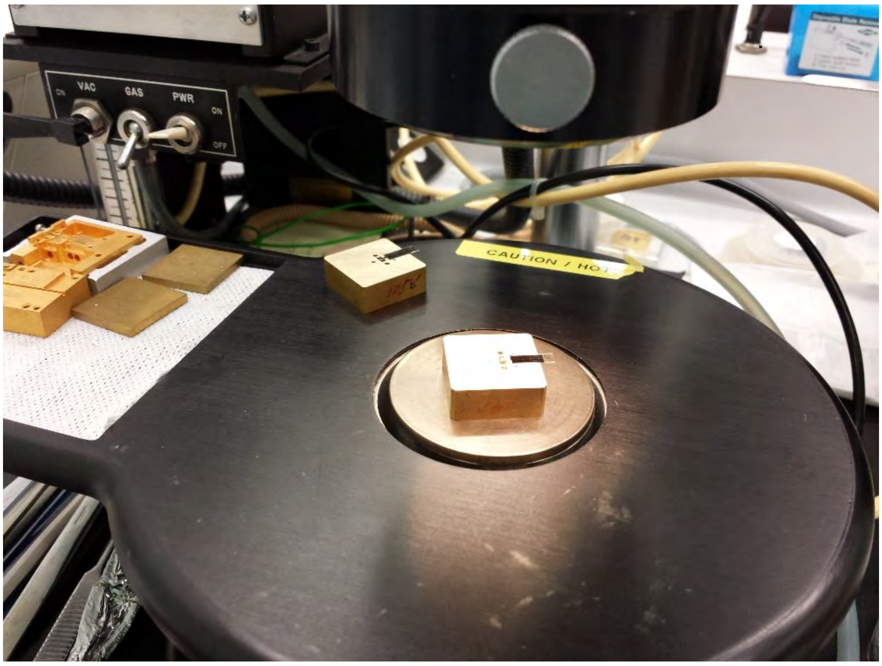

Figure 5.10. Antenna and transition block assembled on heating platform under microscope

5.2.5. MEASUREMENT

To measure the reflection coefficient and radiation patterns of devices, a well-designed microstrip-to-waveguide transition based on the standard WR-15 rectangular waveguide was optimized and built. Figure 5.11 shows the schematic design of the transition, the distance d (figure 5.11(a)) between the inserting pin on substrate and waveguide shorted top is a critical parameter for the performance. The CAD files are provided in figure 5.12, the transition block is mechanically machined out of brass. The waveguide (figure 5.12(a)) and the back short (figure 5.12(b)) were aligned with two screws and an alignment pin.

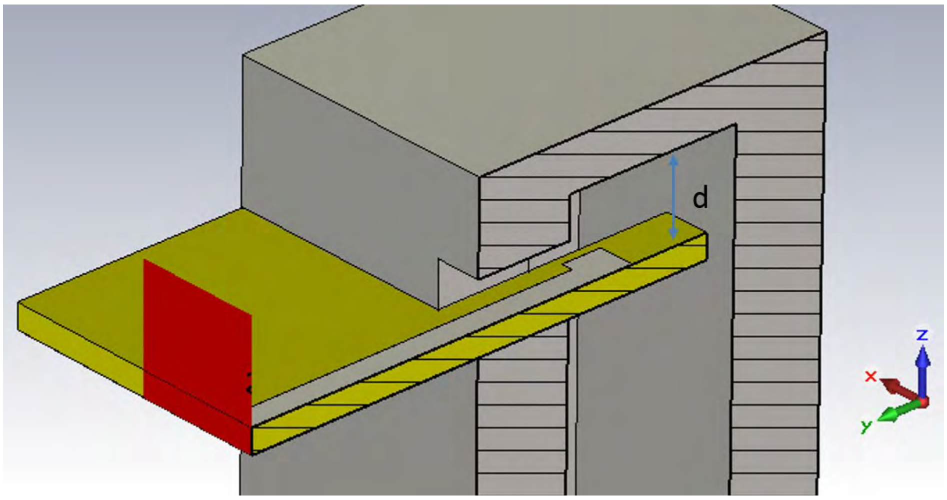

(a)

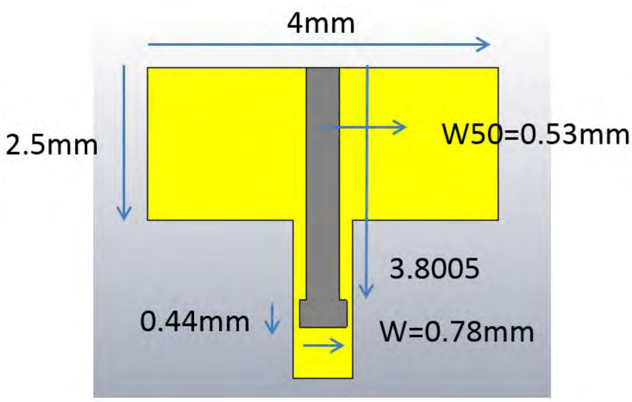

(b)

Figure 5.11. Schematic design of the microstrip-to-waveguide transition

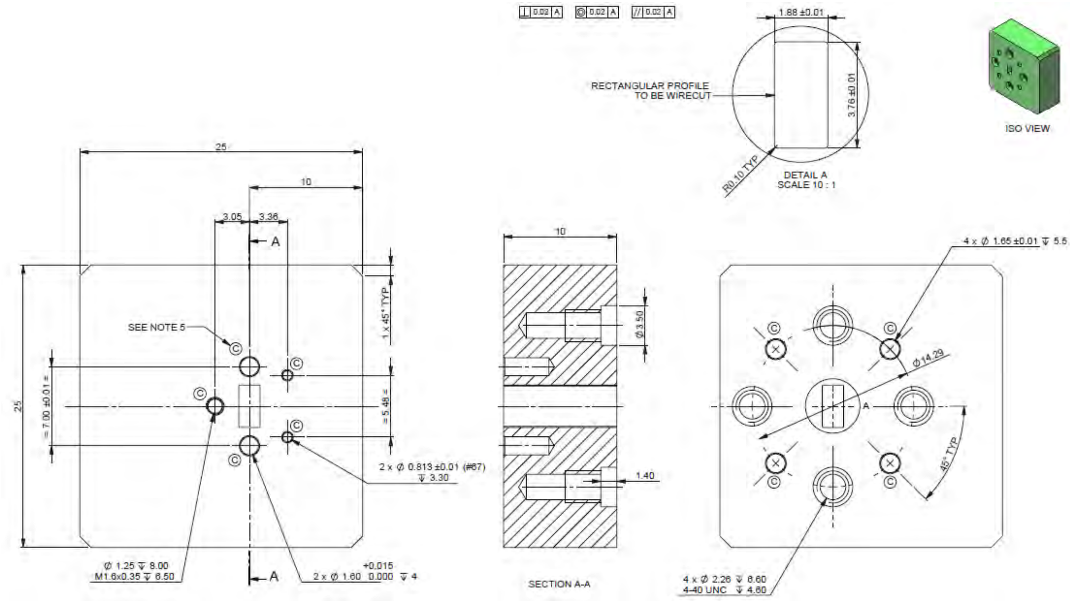

(a)

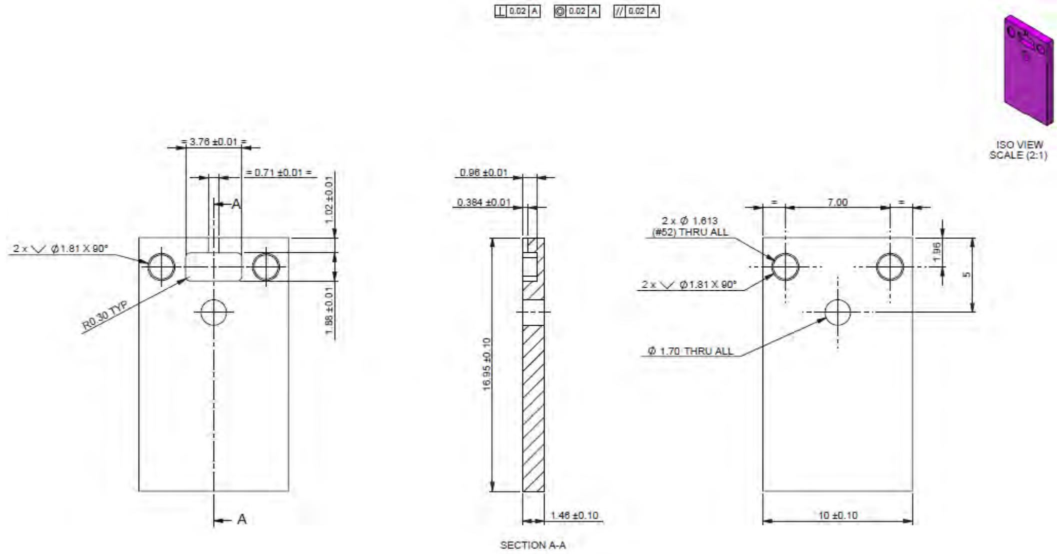

(b)

Figure 5.12. AutoCAD design of the (a) waveguide and (b) back short

Unlike the high precision surface micromachining, the mechanical manufacturing has its limitations when come to small devices that intended to work at 60 GHz. The tolerances and errors of mechanical fabrication introduce certain degradation in performance of the transition. Figure 5.13 shows the relatively rough edges of the waveguide and the errors in waveguide dimensions.

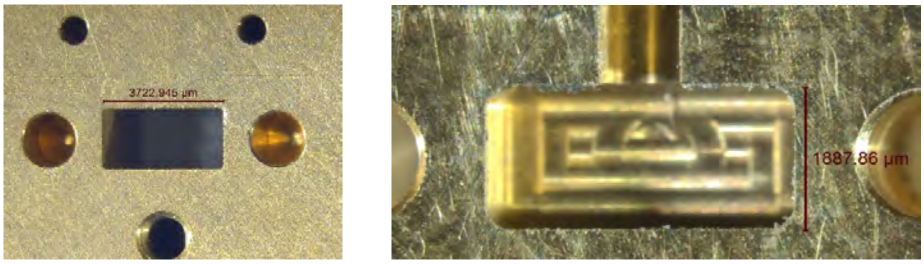

Figure 5.13. Photographs of the waveguide (left) and top back short (right)

The measured back-to-back transmission loss is shown in figure 5.14. The insertion loss of the back-to-back transition block is less than 0.6 dB and the return loss is better than 20 dB across the interested bandwidth.

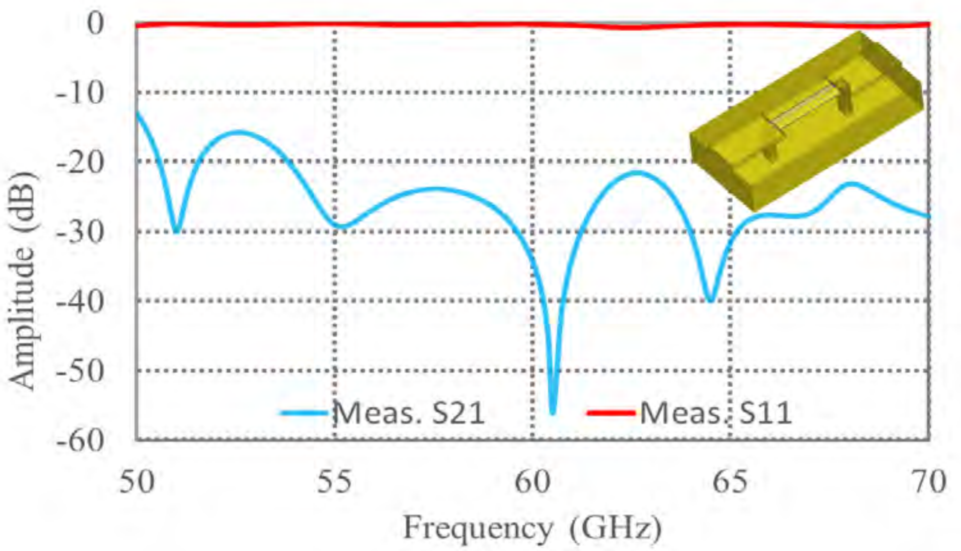

Figure 5.14. The measured back-to-back insertion loss S21 and return loss S11

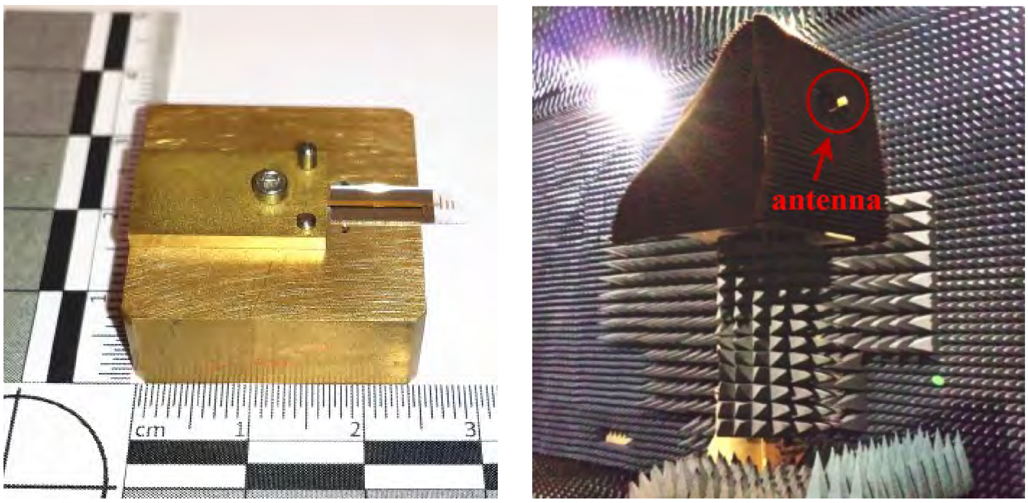

Figure 5.15. Photographs of the quasi-Yagi antenna bonded on the microstrip-to-waveguide transition (left) and antenna mounted on testing positioner in anechoic chamber.

Figure 5.15 shows the photographs of quasi-Yagi antenna integrated with the transition block and the CSIRO antenna measurement chamber.

The simulated and measured reflection coefficients (S11) of five antennas are shown in figure 5.16. All the antennas with the same director elements and matching network exhibit good impedance matching with S11 < -15 dB at 60 GHz, while their operating bandwidth covered 57 GHz - 66 GHz.

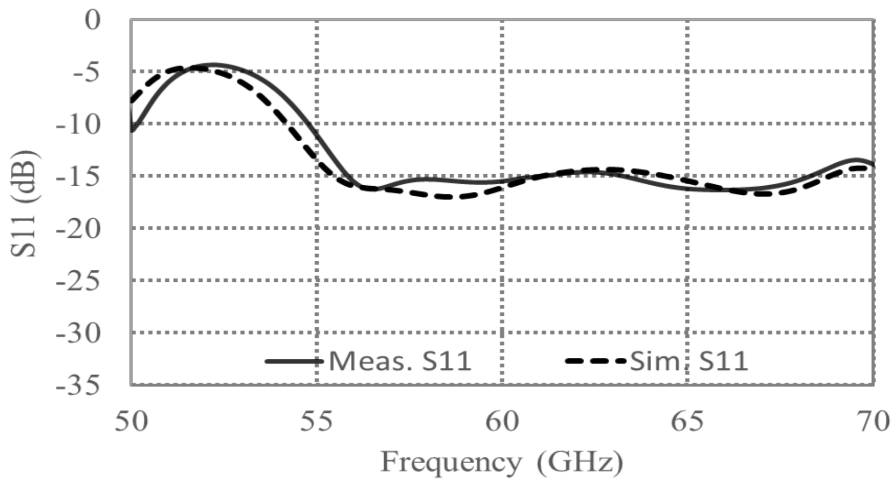

(a)

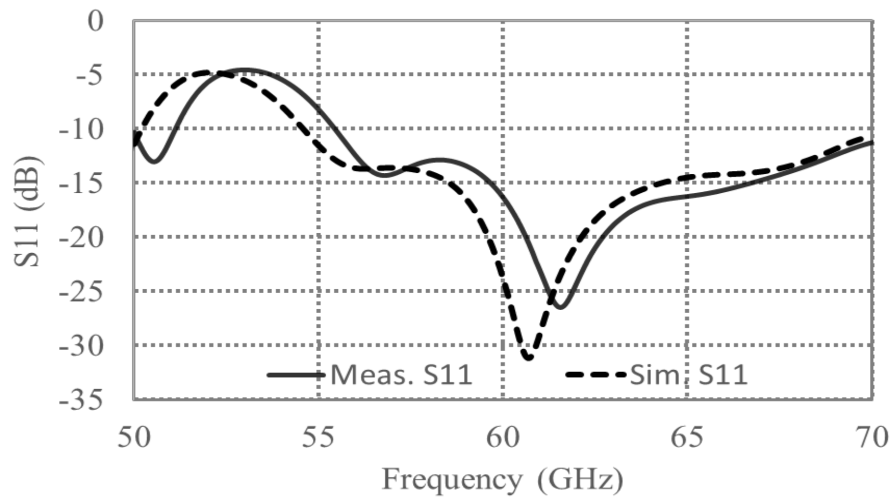

(b)

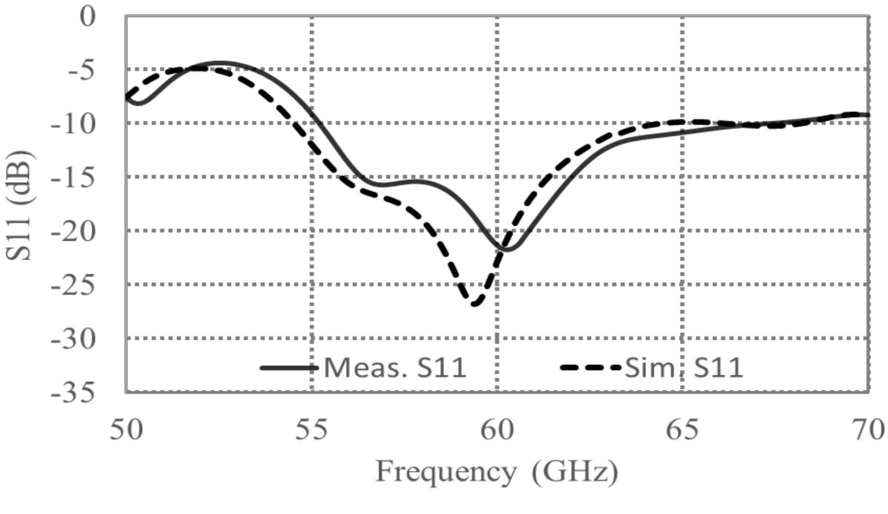

(c)

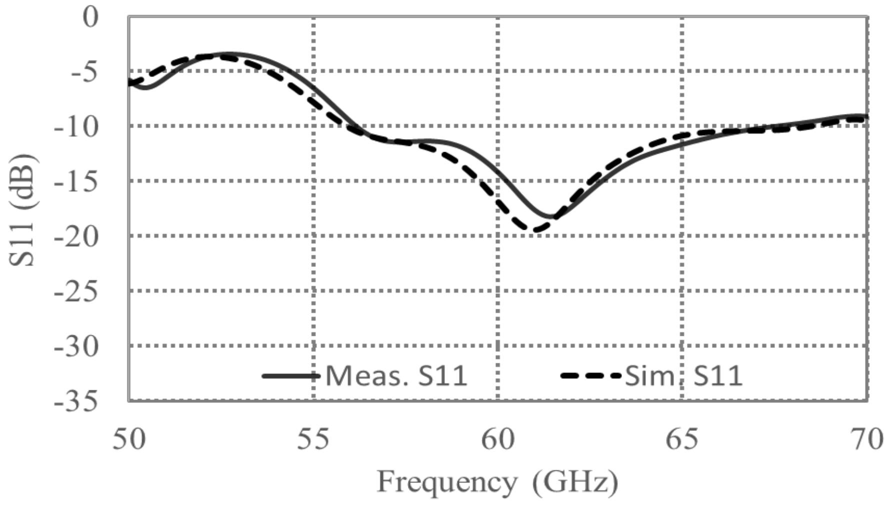

(d)

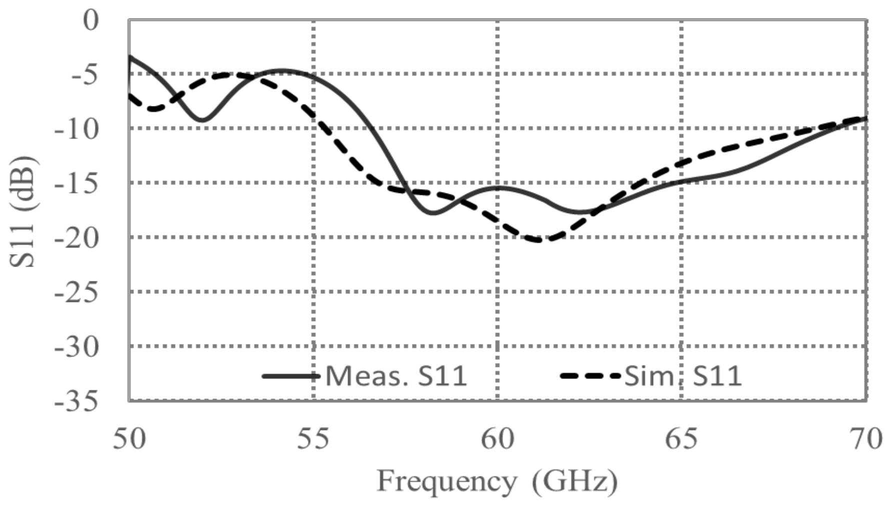

(e)

Figure 5.16. Simulated and measured S11 for antennas with beam shift of: (a) -20° (b) -10° (c) 0° (d) 10° (e) 20°

There are some slight frequency shifts between the simulated and measured results (figure 5.16). These shifts may have been introduced by the tolerances in fabricated dimensions of the transition block and the antennas, and the packaging errors. The packaging was done by hand, using conductive epoxy to bond the quartz substrates to the WR-15 transition blocks under the microscope. It is possible that the thickness of epoxy layer caused a discrepancy in performance of antennas.

The bulky transition block made of brass degrades the performance of quasi-Yagi antennas in terms of the frequency responses and radiation patterns, when compared the simulation results of antennas with and without transitions (figure 5.5).

The far-field radiation patterns were measured in an anechoic chamber; the results for the co- and cross-polar radiation patterns at 60 GHz are compared in following figure 5.17.

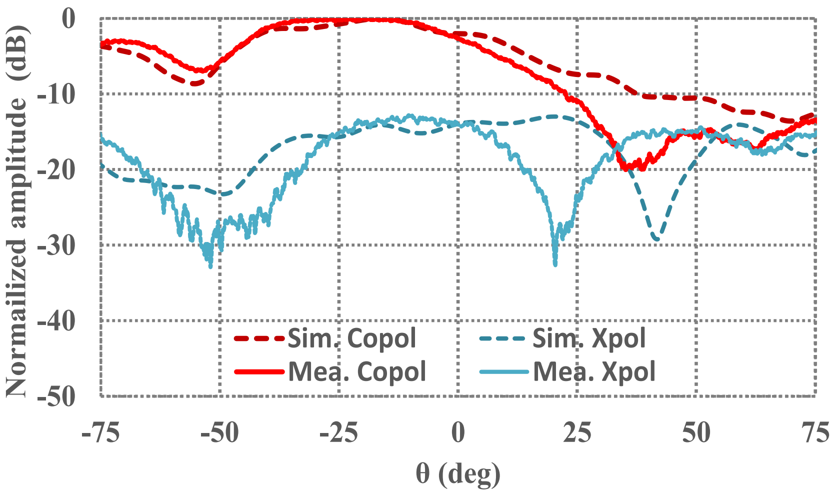

(a)

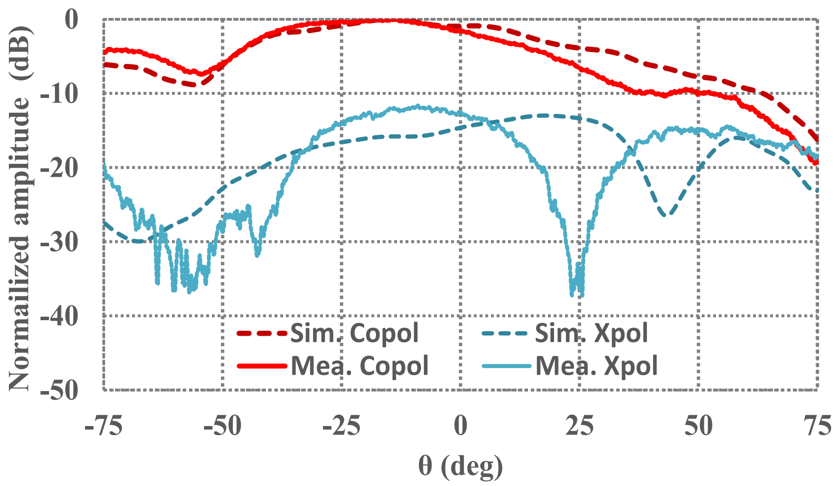
Normalized amplitude (dB)
0
-10
-20
-30
-40
-50
-75
-50
-25
0
25
50
75
θ (deg)
Sim. Copol
Mea. Copol
Sim. Xpol
Mea. Xpol

(b)

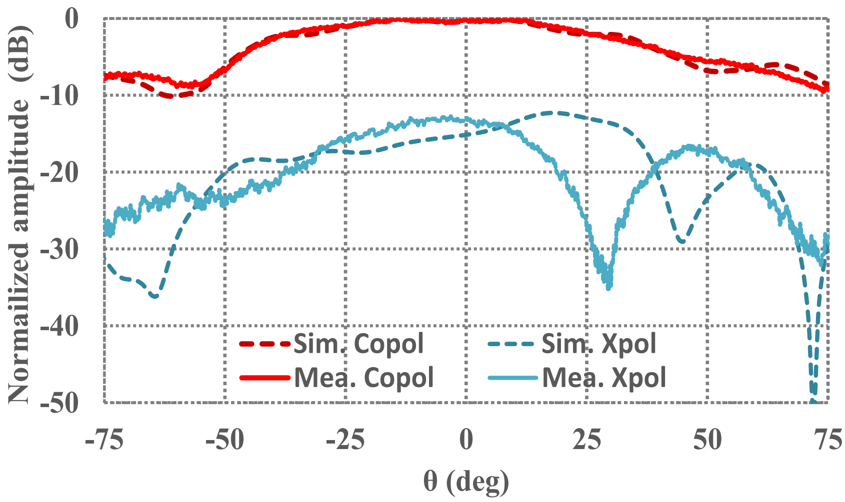
Normalized amplitude (dB)
0
-10
-20
-30
-40
-50
-75
-50
-25
0
25
50
75
θ (deg)
Sim. Copol
Mea. Copol
Sim. Xpol
Mea. Xpol

(c)

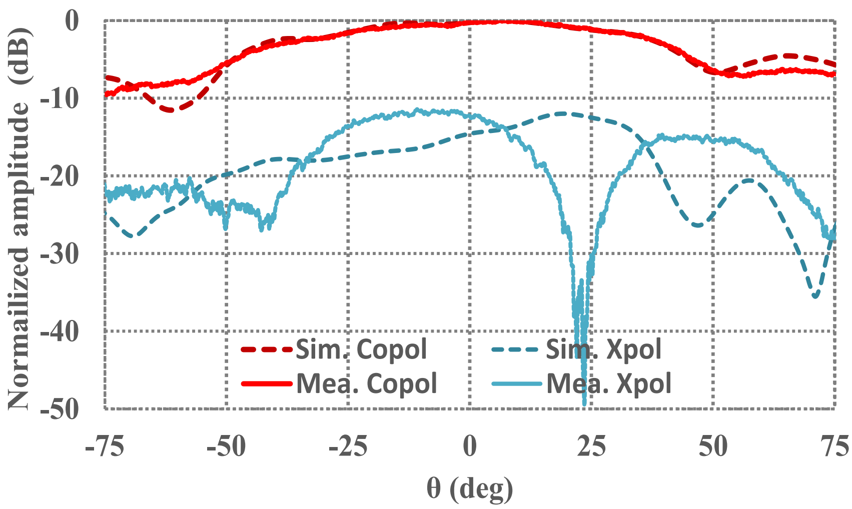
Normalized amplitude (dB)
0
-10
-20
-30
-40
-50
-75
-50
-25
0
25
50
75
θ (deg)
Sim. Copol
Mea. Copol
Sim. Xpol
Mea. Xpol

(d)

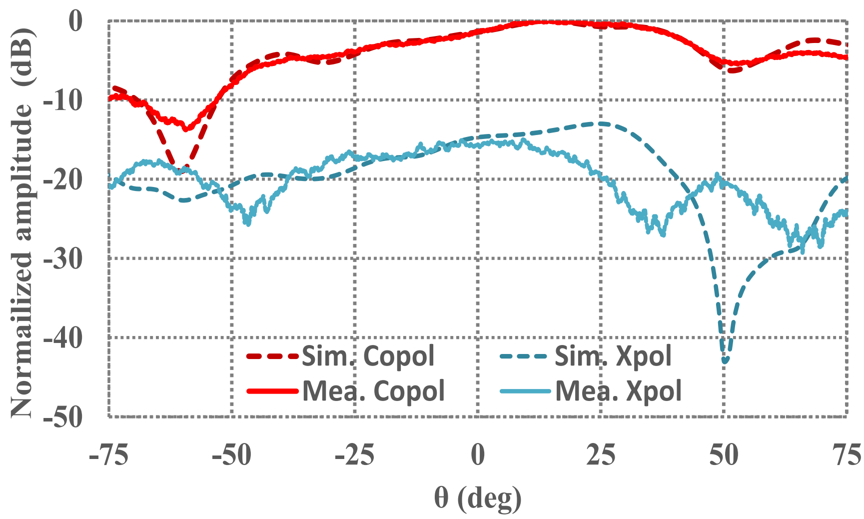

(e)

Figure 5.17. Simulated and measured E-plane co- and cross-polar radiation patterns at 60 GHz for five antennas with radiation beam shift of: (a) -20°; (b) -10°; (c) 0°; (d) 10°; (e) 20°

Due to the bulky waveguide transition structure and antenna positioner, the radiation patterns were only measured for the angles from -75° to 75° (figure 5.15). As can be seen from figure 5.17, a good agreement between the simulated and measured results is achieved for co-polarization; distortions of the cross-polar radiation patterns are because of the mechanical fabrication precision of waveguide structure is limited, so the distance between truncated ground plane edge and transition block is varied from the simulation condition. Beam shifts of quasi-Yagi antennas are clearly observed and maximum beam direction has been tuned to -20° to +20° in 10° steps as we intended. In other words, pattern reconfigurability of designed quasi-Yagi antenna has been successfully proved.

Judging by the results, the H-plane radiation patterns are not affected by the changes of dipole driven arms or the balun dimensions.

Gains of the antennas were measured using the gain comparison method [186], where the received power of the antenna under test is compared with a standard horn antenna of known gain. The realized maximum gains are listed in table 5.5. All antennas achieve good radiation performance and efficiency. Variation between the predicted and measured gain is within 0.8 dB, and this is considered to cause by additional losses in the microstrip-to-waveguide transition. The estimated uncertainty in the gain measurements is ±0.5 dB.

Table 5.5. Realized maximum gain of five antennas

Angle (°)	-20	-10	0	+10	+20
Gain (dB)	6.91	6.72	6.35	6.28	6.33

5.2.6. CONCLUSION

This section proposed an innovative design method of pattern reconfigurable quasi-Yagi antenna and the experimental results have proved the feasibility of this methodology. Measurements shows that the E-plane radiation pattern of quasi-Yagi antenna can be controlled by tuning the lengths of driven dipole arms and the microstrip-to-CPS transition delay line without change of the operating frequency band. Five quasi-Yagi antennas using same elements but different dimensions of dipole arms and delay line have been successfully designed, fabricated and assembled to point their maximum radiation direction from -20° to +20° with 10° spacing. The working spectrum covers WPAN band. This work provides a solution suitable for future pattern reconfigurable antenna design, in which a single antenna can sweep its beam in E-plane by employing the RF MEMS switches, to alter the electrical lengths of its dipole arms and the balun.

5.3. RF MEMS INTEGRATED PATTERN RECONFIGURABLE QUASI-YAGI ANTENNA

Based on the discovery detailed in last section, a 60 GHz MEMS integrated pattern reconfigurable antenna was designed. The E-plane radiation beam of the monolithic antenna can be point at -15°, 0° and 15° while maintain a decent realized gain and operating frequency band of WPAN band.

5.3.1. ANTENNA DESIGN

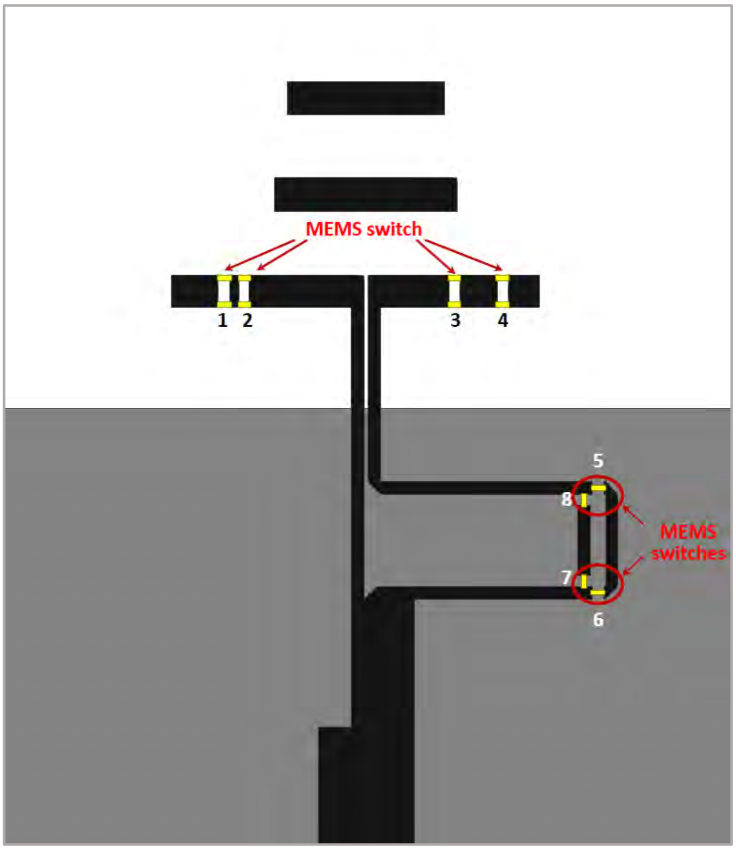

Figure 5.18. Schematic layout of pattern reconfigurable antenna

The configuration of the proposed reconfigurable antenna is shown in figure 5.18. The dipole elements and feeding structures are deposited on the quartz substrate (ε_r=3.75

thickness h = 0.254mm, tanδ = 0.0004), on which the RF MEMS switches are fabricated. Twelve RF MEMS switches are embedded in gaps on the driven dipole and microstrip-to-CPS transition as in figure 5.18. Each dipole gap has two switches (form a group) located at the edges of the dipole because the edges have strongest surface current distribution. Switches are numbered from 1 to 8, the grouped switches that bridging the same dipole gap have the same number because they will be actuated at the same time. By controlling the biasing voltages applied on the beams and the electrodes of the RF MEMS switches, the effective lengths of the dipole driven arms and transition delay line are changed so that the radiation beam direction of the antenna is shifted.

Biasing lines and electrodes are defined by evaporating 110 nm layer of germanium (Ge) thin film. Then a 300nm thick silicon dioxide (SiO_2) layer is deposited and patterned to cover the Ge Biasing lines. The thin dielectric film is used for preventing direct contact between the gold cantilever and the Ge electrode. The antenna structure and the feeding network are defined by E-beam evaporating of 0.04/1.0 μm layer of titanium/gold (Ti/Au). Titanium is used for adhesion layer between the gold and substrate. The length of the cantilever beam is 80 μm and the actuation gap is 2.5 μm.

In this design, a high resistive Ge biasing network is proposed as shown in figure 5.19. The measured conductivity of the annealed Ge is less than 1000 Siemens/m which is 7600 times smaller than the conductivity of Cr. The Ge biasing network with such low conductivity is invisible to the antenna structure at 60 GHz and it has very little effect on antenna's performance. The dimple of the cantilever beam is facing outwards and the anchor is placed on the inner side of the dipole elements so that all the switches can share the 0V (reference DC ground). To simplify the biasing network, the electrodes of the RF MEMS switches that actuated at the same time are connected together as a group. The biasing lines in red color are extended to connect to biasing pads where positive voltage is applied (+V1) to control the switch actuation. It is noted that there is no current between the cantilever beams and electrodes while the switches are actuated. This feature guarantees that the cascaded electrodes will be able to share the same biasing voltage of +V1. When the biasing voltage is applied to the electrodes on same side of the dipole arm, the dimple of the RF MEMS switches will be pulled down touching the gold dipole (ON state). Therefore, the gap is bridged to form longer dipole arm to steer the radiation pattern. The switching mechanism is shown in table 5.6.

Table 5.6. Switching mechanism for three states with beam shift of: -15°, 0°, 15°

Radiation shift	ON state switches	OFF state switches
-15°	1, 2, 5, 6	3, 4, 7, 8
0°	2, 3, 5, 6	1, 4, 7, 8
15°	3, 4, 7, 8	1, 2, 5, 6

Release holes are added on the cantilever beams to strip out the sacrificial layer. The pull-down voltage is decided mainly upon the width and length of the cantilever beam as well as the actuation gap. This voltage is calculated to be 40 V.

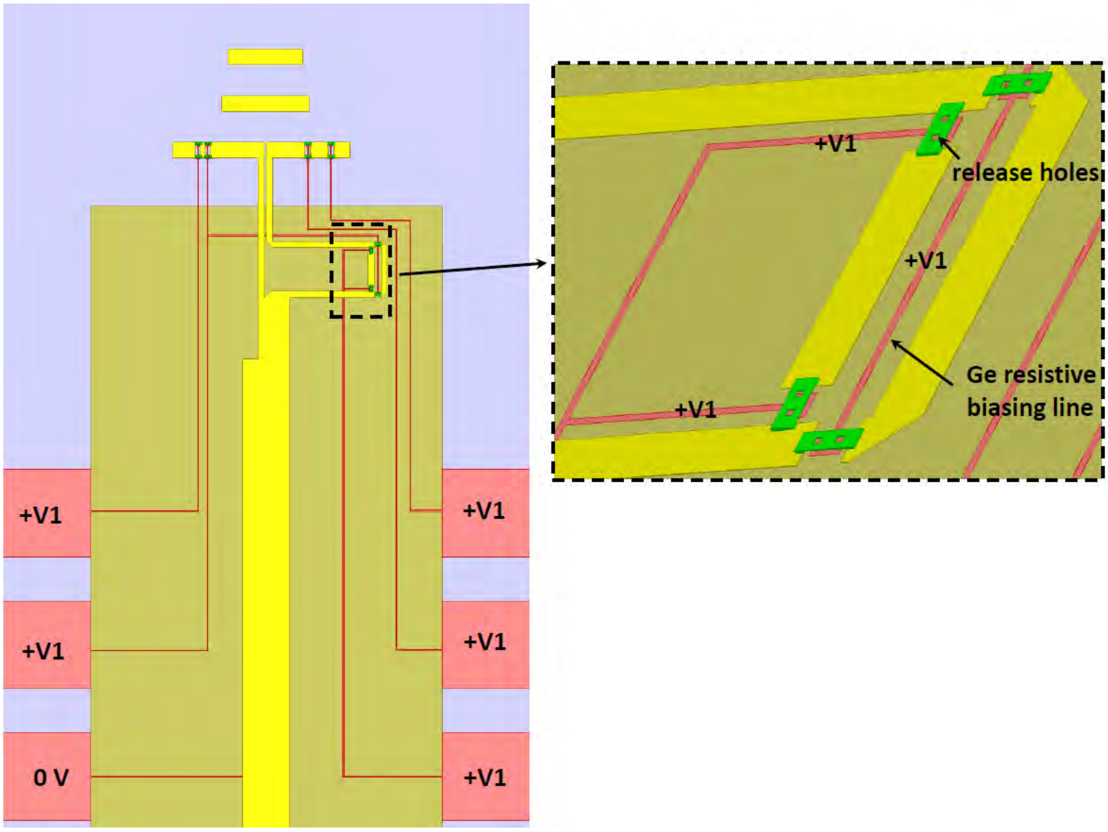

Figure 5.19. Resistive biasing configuration for the proposed reconfigurable antenna. Zoomed-in diagram shows the detail of the biasing line and the orientation of the RF MEMS switches.

5.3.2. SIMULATION RESULTS

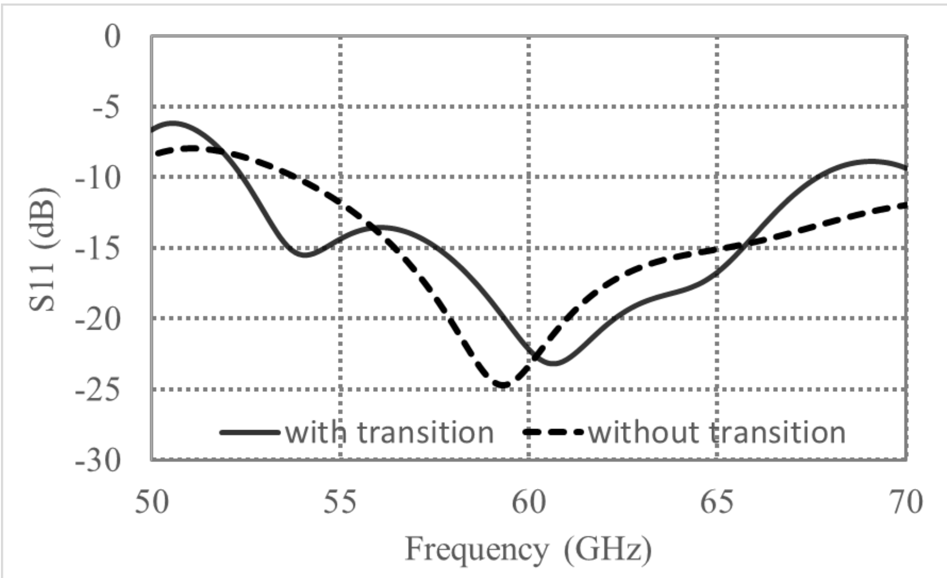

(a)

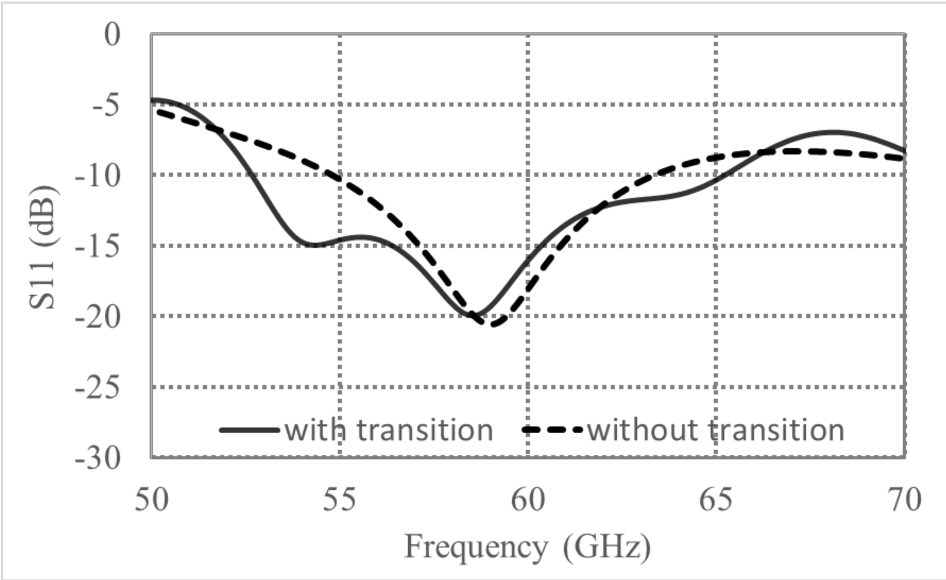

(b)

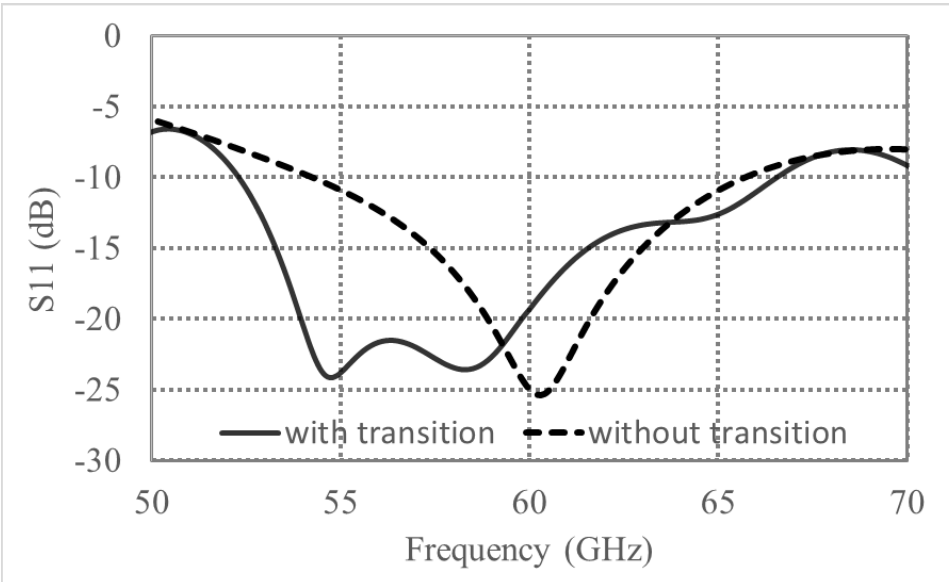

(c)

Figure 5.20. Reflection coefficient of antennas with and without microstrip-to-waveguide transition block for different beam shift: (a) -15° (b) 0° (c) 15°

As can be seen in the figure 5.20, the microstrip-to-waveguide transition block does add certain frequency shift to the antenna. The operating spectrum of antennas with or without transition block with good impedance matching (|S11| ≤ -10 dB) is sufficiently large to cover 57 GHz – 66 GHz WPAN band.

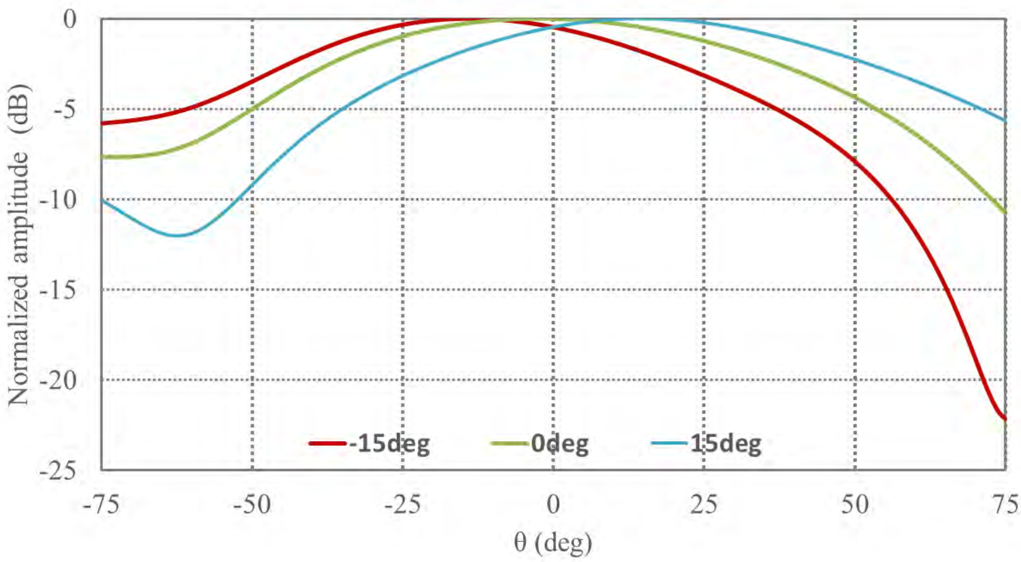

(a)

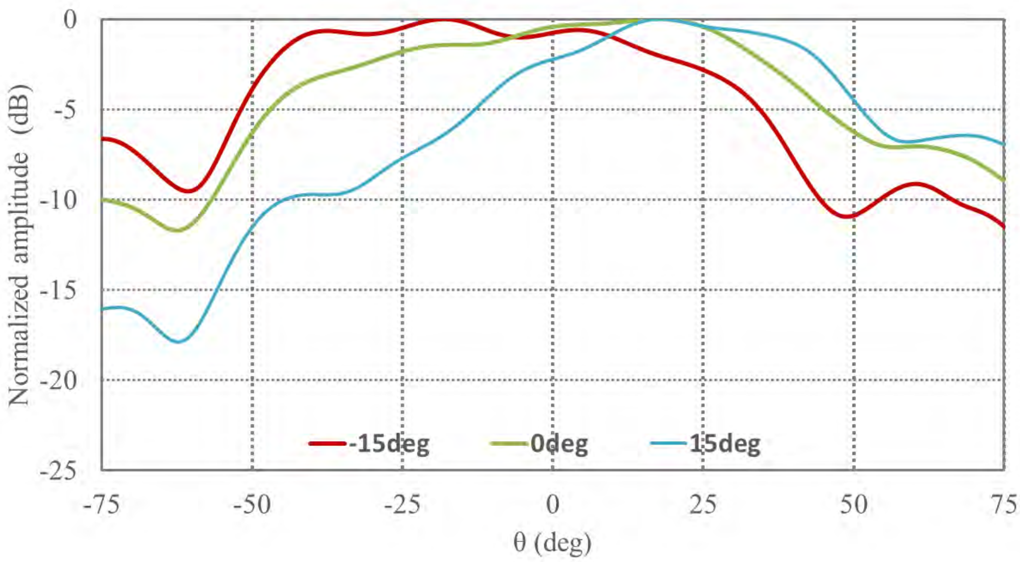

(b)

Figure 5.21. Simulated antenna E-plane radiation patterns, maximum beam direction steered of: -15°, 0°, 15° (a) antennas without transition (b) antennas mounted on transition (normalized gain)

As shown in figure 5.21, the antenna radiation pattern reconfigurability is clearly observed. The transition block add some ripples on the radiation patterns and affect the maximum beam direction. Although the maximum beam width of 0° antenna with transition is shifted to +16° (figure 5.21 (b)), the half power beamwidth (HPBW) is still unchanged (covers -38° to +39°) which centered at 0.5°. The total coverage of monolithic reconfigurable antenna is from -54° to +58°, which is 31° more that the fixed single Yagi antenna. And the pattern reconfigurability gives monolithic antenna more flexibility to point its beam at intended customer's direction while avoid the noise from unwanted directions. The antenna's realized gains are listed in the table below.

Table 5.7. Simulated antenna realized gain (dB)

Angle	-15°	0°	15°
Gain without transition	6.62	6.31	6.06
Gain with transition	6.69	6.68	7.71

5.3.3. FABRICATION

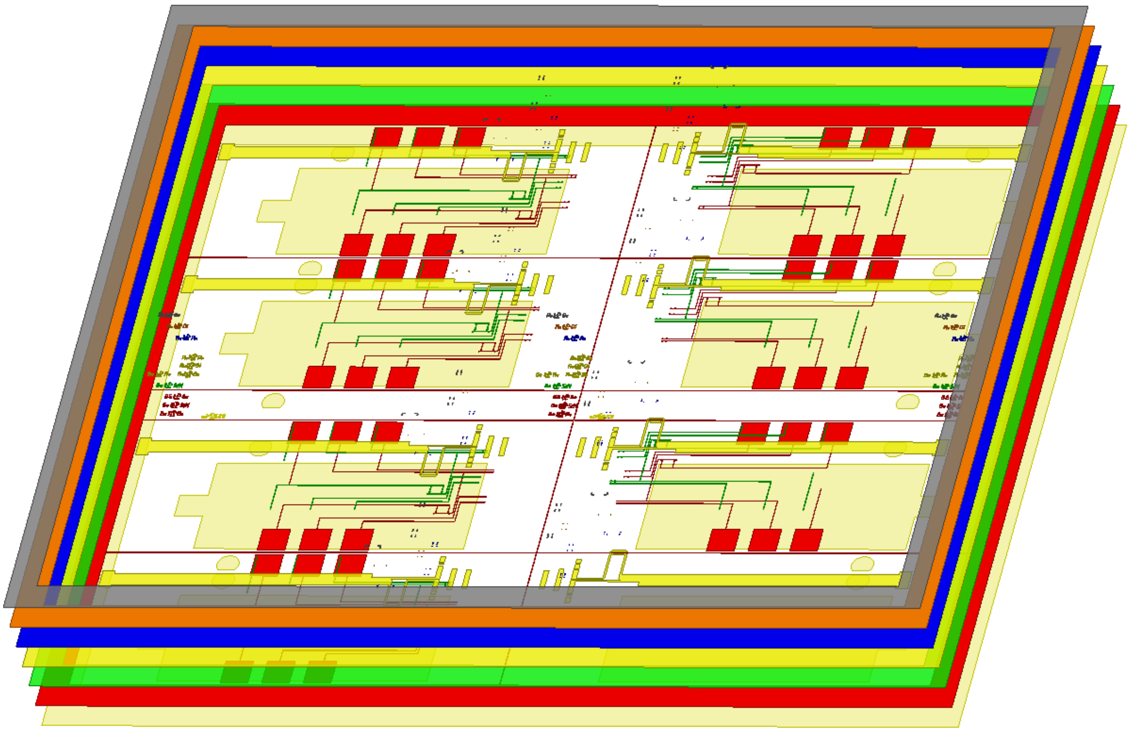

Figure 5.22. Seven layers mask for antenna fabrication

A seven layers mask has been designed and fabricated for the monolithic antenna fabrication. The fabrication is under progress, and fabrication processes details are provided in the next chapter.

5.3.4. CONCLUSION

In this section, a new RF MEMS-integrated millimeter-wave pattern reconfigurable quasi-Yagi antenna is proposed. The E-plane radiation beam direction is switchable between -15°, 0° and 15°by actuating of the RF MEMS switches employed on the driven dipole and transition delay line elements. The total coverage of monolithic antenna is from -54° to +58°, which is 31° more that the fixed single Yagi antenna while maintaining good reflection coefficient and realized gain at WPAN band (57 GHz – 66 GHz). This antenna, only take space same as a fixed printed Yagi antenna, is much smaller compared to the phased array which requires at least two antennas and complex phase shifting network. A germanium very low conductivity biasing configuration is proposed. The low conductivity make the biasing network invisible to the antenna structure therefore guarantees the excellent radiation performance. This is the first monolithic antenna utilizing Ge and integrating its deposition into the fabrication process. The next step of work will focus on the fabrication of the antenna.

5.4. RHCP PATTERN-RECONFIGURABLE SPIRAL ANTENNA BIASED WITH TWO DC SIGNALS

In this section, a right-hand circularly-polarized (RHCP) beam steering spiral antenna is presented. It was designed using the standard PIN technology, while enhanced the arm switches and biasing lines. The design is easily manufactured and its function is competitive with the more complex ones based on RF MEMS. Three beams, tilted 40° with respect to the spiral central axis, are generated at 3.3 GHz for WiMax systems. These beams are directed at approximately 90°, 180°, and 270° (case 1-3) in the azimuth space. Beam directions depend on various configurations of the seven PIN diodes added to the spiral structure. The states of the diodes are controlled by the DC bias voltage connected to the spiral arm. The radiation performance over the 200-MHz-bandwidth (3.2 - 3.4GHz) is relatively stable. The measurement results shows good impedance match ($|S11| < -10dB$) in the desired bandwidth and the axial ratio below or close to 3 dB at the peak beam directions. This work was a collaboration with postgraduate student Liang Gong.

5.4.1. INTRODUCTION

Spiral antennas feature circular polarization and broad frequency band. Many designs have been reported with switching circuits on the spiral arm to achieve pattern reconfigurability [187-190]. In [2], the packaged RF-MEMS switches are inserted into the spiral arm to reconfigure the radiation pattern between end-fire and broadside. Capacitors and resistors were used to build the biasing networks, enabling automatic reconfigurability. In [3], more beam directions are achieved when monolithically integrated RF-MEMS switches are used. High impedance surface were used to get wider coverage in the azimuth plane and to decrease thickness of the substrate in [4]. However, no biasing strategy has been proposed due to the use of the high impedance surface.

5.4.2. SPIRAL ANTENNA DESIGN

The spiral arm is fabricated on Rogers 4350 using conventional circuit printing technology. This substrate has dielectric constant of 3.66. The total thickness is set to be 11.43 mm, which is approximately a quarter of guided wavelength at the operating frequency. As 11.43 mm thick Rogers 4350 is not commercially available, seven substrates of 1.524 mm thick and one of 0.762 mm thick are stacked together to achieve this thickness. Four plastic screws are placed in the corners of the substrate to minimize the air gap between adjacent laminates and avoid loss and interference.

The spiral arm is composed of multiple copper traces with the first strip of length a=4.8 mm. The subsequent lengths increase, following the pattern a, 2a, 2a, 3a, 3a… 7a, 7a, 8a; this is closed off with the last strip of 3 mm long. The spiral structure is center-fed through a coaxial SMA connector, with its outer conductor soldered to the ground plane and the inner probe connected to the center of the top trace.

This work uses seven switches and two bridges on the antenna. PIN diode model

MA4AGBLP912 was used in this design gives a series resistance of 4Ω at ON state, isolation of 30 dB at OFF state, and a total capacitance of 28 fF. Current threshold for switching ON the diode is around 10 mA. Typical voltage to actuate the switches is 1.4 V. Two DC bias signals, DC1 and DC2 along with a DC ground are connected to the spiral arm to actuate the switches and alter the current distribution. DC1 is superimposed with the RF signal via the inner conductor of the coaxial cable connecting with a bias-tee, while DC2 and DC ground are applied to the spiral arm via the side biasing pads on the edges of substrate. Specifically, Pad 1 is reserved for DC2, while both Pad 2 and Pad 3 are connected to the DC ground.

The equivalent circuit of the biasing network is illustrated in figure 5.23. Both positive and negative voltages are required to satisfy the switch states for Case 1 - 3, presented in table 5.8. For instance, to enable Case 3, the DC1 and DC 2 are set to +4.2 V and -1.4 V respectively. During the measurements, two 68 Ω resistors are used to limit the current increment and prevent damage. Extra Ampère meters are used for monitoring the current. The resistors and Ampère meters are not compulsory components for the antenna system if the voltages can be tuned precisely by the DC voltage source.

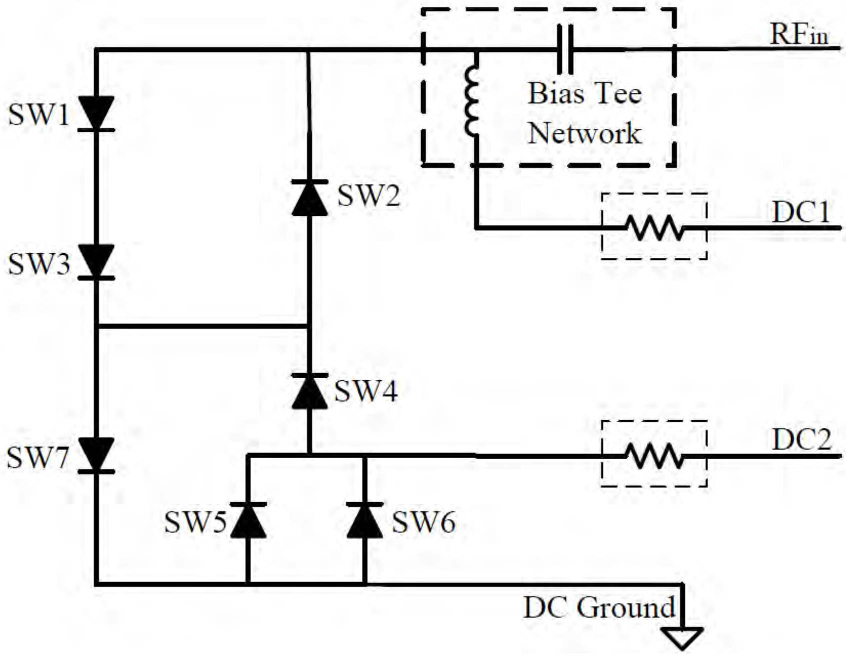

Figure 5.23. Equivalent circuit of the biasing network

Table 5.8 switching mechanism for case 1-3

	SW1	SW2	SW3	SW4	SW5	SW6	SW7
Case 1	OFF	ON	OFF	ON	OFF	OFF	OFF
Case 2	ON	OFF	ON	ON	OFF	OFF	ON
Case 3	ON	OFF	ON	OFF	ON	ON	ON

In general, bias networks and filters, which consist of capacitors and inductors, are necessary for biasing PIN diodes while blocking RF signals from flowing to DC sources. As a result, the via-holes need to be drilled on the substrate. In this design, the substrate is too thick to make via-holes from the top to the bottom layer. Instead, quarter wavelength open stubs are applied to choke RF signals. Both biasing lines and matching stubs are set to be a quarter wavelength long to ensure the signals are open-circuited at the pads.

5.4.3. MEASUREMENTS

All of the measurements are carried out in CSIRO ICT Center. S-parameter is measured by Agilent E8363B PNA Network Analyzer. Figure 5.24 shows both the simulated and measured S-parameters for the different cases. It can be seen that the return loss is better than 10 dB for all the cases in the 3.3 GHz band.

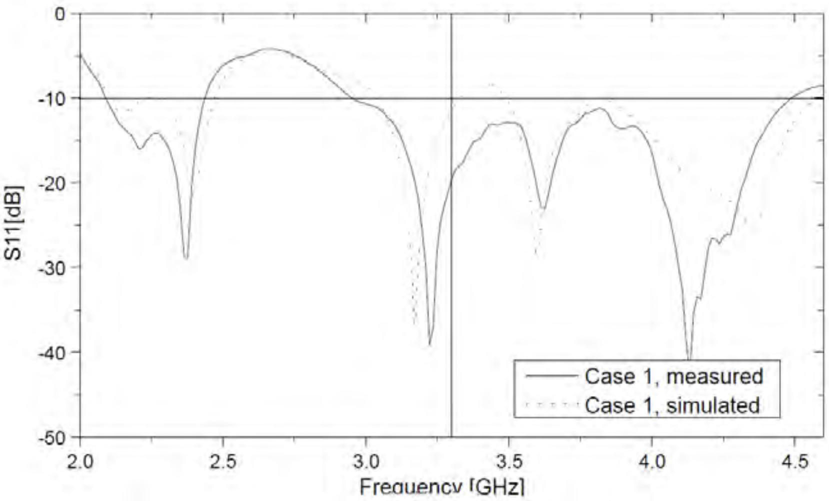

(a)

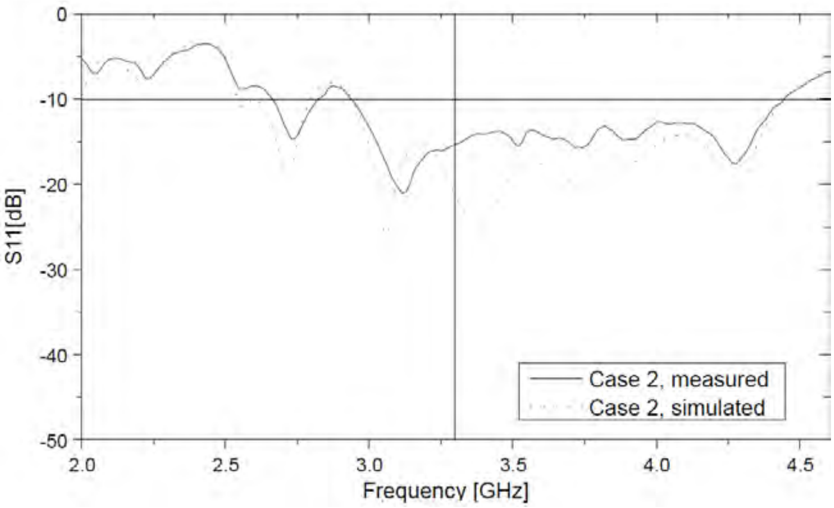

(b)

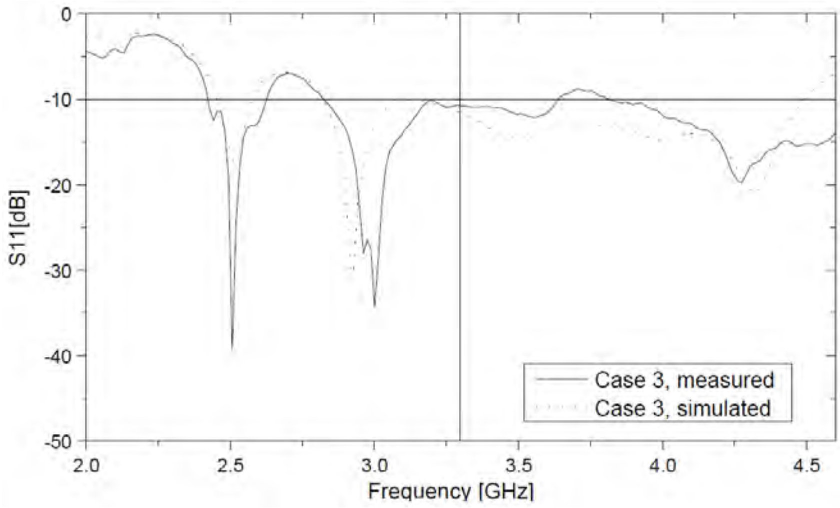

(c)

Figure 5.24. Simulated and measured reflection coefficient of: (a) case 1, (b) case 2 and (c) case 3

For radiation pattern, it would require a 3-D pattern to sketch the shape of spiral antenna radiation. However, it is not feasible considered that this task needs infinite measurements for three cases. Therefore, the actual measurements are guided by the simulated maximum φ (azimuth angle), and then plot the radiation patterns with corresponding θ (elevation angle).

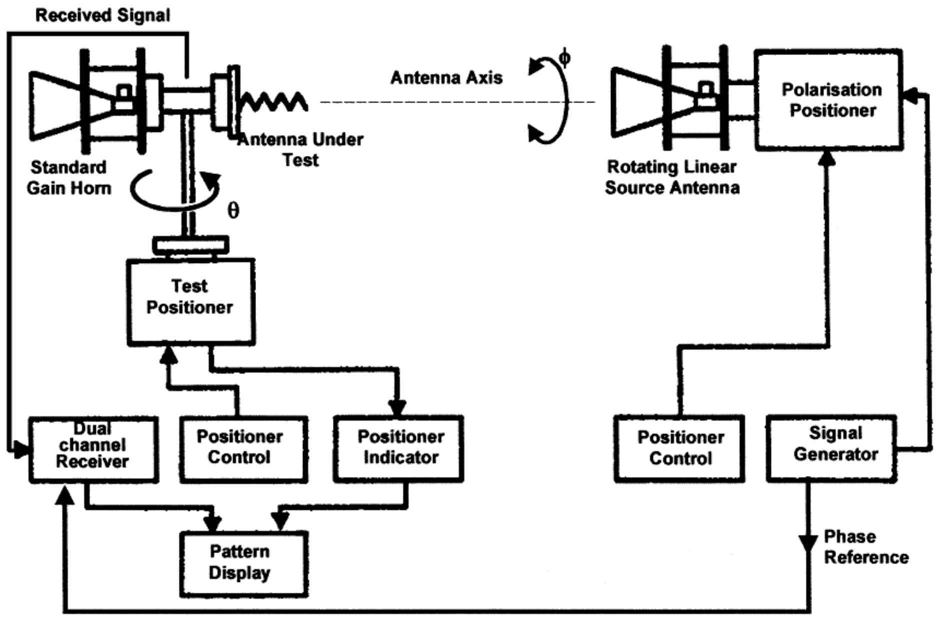

Figure 5.25. Antenna test equipment setup

Figure 5.25 illustrates a general setup for radiation pattern measurement for elliptically polarized antennas. There are two rotating elements in this configuration: one is the positioner on the antenna under test (AUT) side, while the other one is the rotating linear transmit antenna.

Three different methods are proposed for measuring this elliptically polarized antennas:

1) Using a rotating transmit antenna with linear polarization. One example is shown in figure 5.26. The upper contour represents the maximum power received by the AUT at a certain direction, and it gives the total radiation gain combines the left-hand circular polarization (LHCP) and right-hand circular polarization (RHCP) gains. The lower contour represents the minimum power received which gives the subtraction of the left-hand circular polarization (LHCP) and right-hand circular polarization (RHCP) gains. The distance between the upper contour and the lower contour gives the axial ratio (AR). Then the LHCP and RHCP radiation pattern can be calculated.

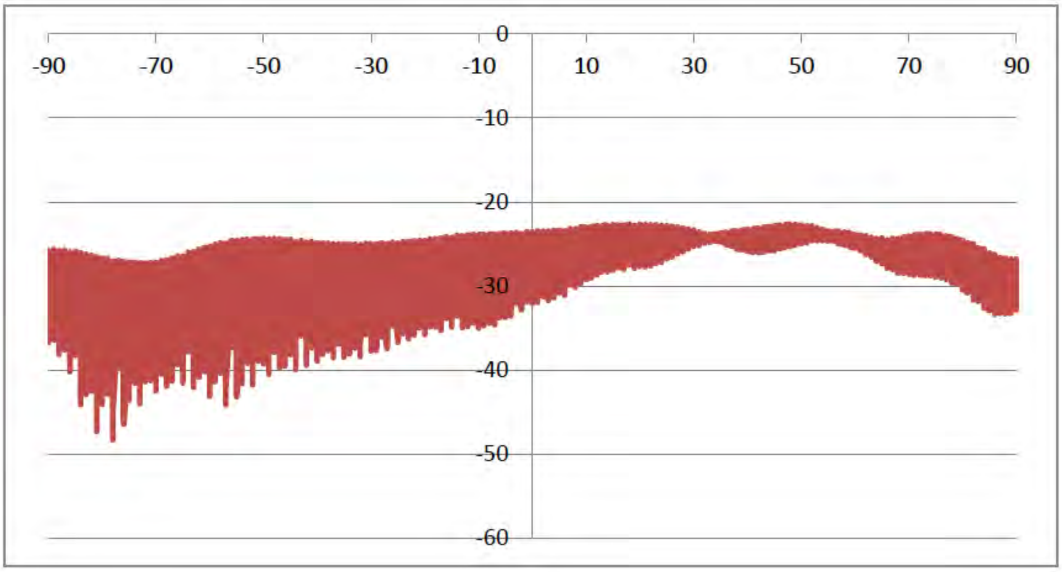

Figure 5.26. Total radiation pattern for case 3 at 3.3 GHz

2) The second method for extracting the individual polarization pattern is to employ two standard circular polarized antennas, in our case cavity-backed Archimedean spiral antennas, one for RHCP and another one for LHCP, to measure the AUT separately. This method is quite straightforward but the drawback is that the precision relies on the circular polarization purity of the standard CP antennas. It is difficult to fabricate a pure circular polarized antenna, so the LHCP proportion in a RHCP transmit antenna leads to errors for the radiation pattern and gain.

3) The third approach proposed is to measure the AUT with two orthogonal cuts. The testing equipment setup is same as the first method, except that the transmit antenna does not spin this time. Initially, set the linear polarized transmit antenna in the vertical position, records the power and phase received by the AUT. Then rotate the transmit antenna to horizontal position, and record the power and phase again. After that the collected data is processed based on follow equations.

If the complex voltage terms in the horizontal and vertical planes (or any two orthogonal cuts) E_H and E_V are of equal amplitude and in phase quadrature (±90°), these terms may be combined to express either the RHCP or LHCP wave components:

$$E_{RHCP} = \frac{1}{\sqrt{2}}(E_H + jE_V) \quad (1) \text{ and } \quad E_{LHCP} = \frac{1}{\sqrt{2}}(E_H - jE_V) \quad (2)$$

Let the real and imaginary components of the horizontal and vertical response be expressed as

$$E_H = E_{Hr} + jE_{Hi}$$

Where

$$E_{Hr} = H_A \cos(H_P); \qquad E_{Hi} = H_A \sin(H_P)$$

And

$$E_V = E_{Vr} + jE_{Vi}$$

Where

$$E_{Vr} = V_A \cos(V_P); \qquad E_{Vi} = V_A \sin(V_P)$$

The horizontal and vertical amplitude (H_A, V_A) and phase components (H_P, V_P) are quantities that are measured at each angle θ in the far field of the antenna. Inserting into (1) and (2) gives the field in the two hands of polarization

$$E_{RHCP} = \frac{1}{\sqrt{2}}\{[H_A \cos(H_P) - V_A \sin(V_P)] + j[H_A \sin(H_P) + V_A \cos(V_P)]\}$$

$$E_{LHCP} = \frac{1}{\sqrt{2}}\{[H_A \cos(H_P) + V_A \sin(V_P)] + j[H_A \sin(H_P) - V_A \cos(V_P)]\}$$

Then we can calculate the radiation pattern using computer.

Figure 5.27 compares the RHCP and LHCP patterns generated by the method 2 and 3. In order to provide an easier comparison, all of them have been normalized with respect to the corresponding maximum RHCP values. The results are quite similar which means the proposed methods are feasible for measuring the circular polarized antenna. Considering the purity problem in method 2, all the final results were generated using method 3.

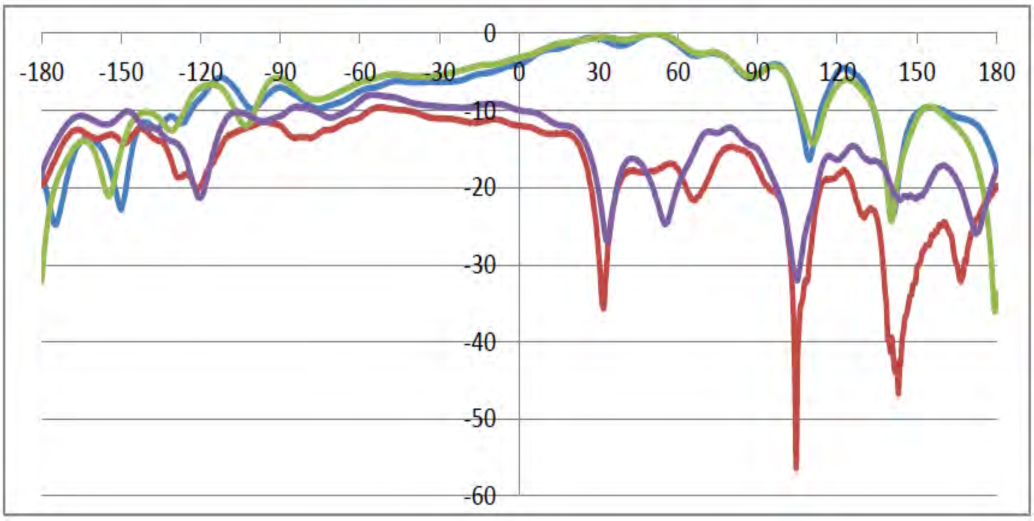

Figure 5.27. Normalized radiation patterns measured by cavity-backed Archimedean spiral antennas: LHCP (red) RHCP (green) and two orthogonal linear polarized antennas: LHCP (purple) and RHCP (blue)

Both the simulated and measured radiation patterns (with method 3) for LHCP and RHCP radiation patterns at 3.3 GHz are compared in figure 5.28.

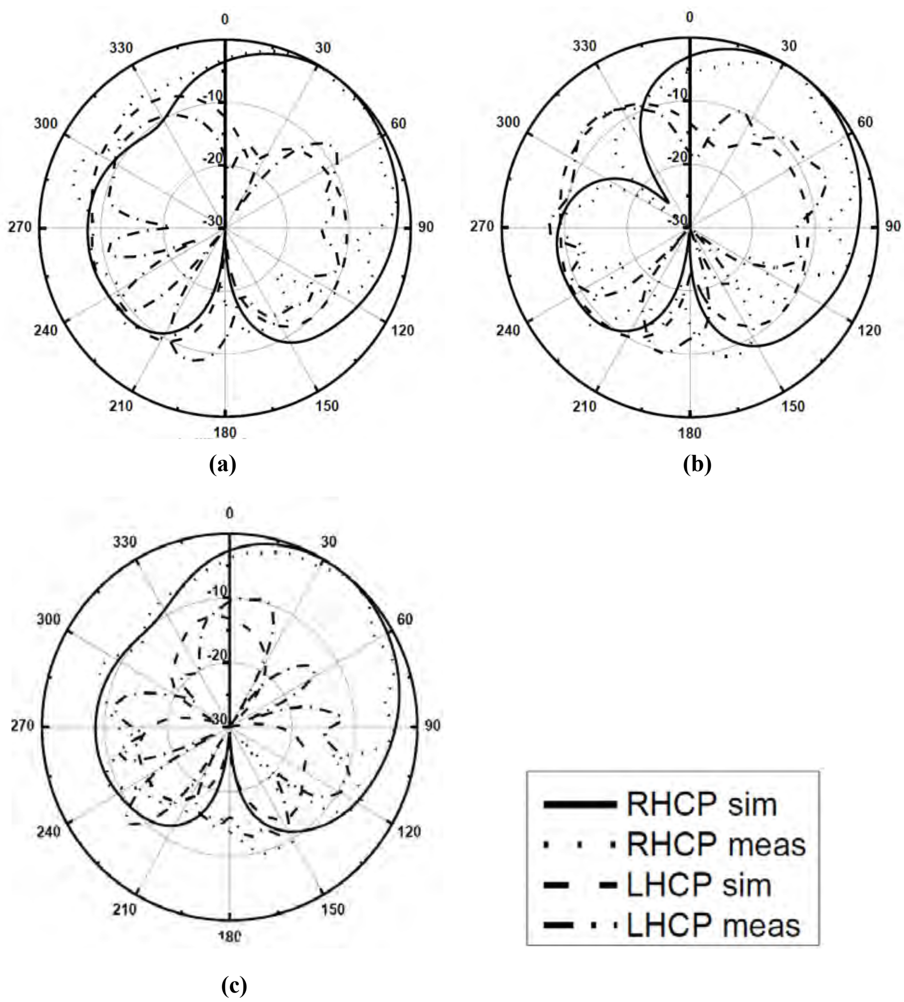

Figure 5.28. Radiation patterns at 3.3 GHz for (a) case 1, φ=93°, (a) case 2, φ=268°, (a) case 3, φ=183°

As the spiral arm is center-fed and right-hand winded, it mainly radiates the RHCP wave. The measured RHCP patterns follow the same trend as the simulated ones while the measured LHCP results do not always resemble the simulation; this suggests possible polarization degradation. This could be due to biasing of the cables attached to pads.

Table 5.9 summarizes parameters and measurement results at different frequency points, (3.2, 3.3 and 3.4 GHz) in terms of their maximum beam directions, showing the maximum gain and axial ratio (AR) at each direction. The maximum beam directions and the gains are dependent on frequency. The gain drops dramatically outside this frequency range, and the main beam splits.

Table 5.9. Summary of simulated and measured parameters for the proposed antenna.

	Freq.	Phi	Max RHCP gain (sim.)	Max theta (sim.)	AR (sim.)	Max theta (meas.)	Max RHCP gain at max theta, phi (meas.)	AR (meas.)
Case 1	3.2GHz	105.0°	4.75 dBic	36.0°	1.80 dB	44.5°	3.82 dBic	5.43 dB
	3.3GHz	93.0°	4.97 dBic	37.0°	3.39 dB	27.5°	4.61 dBic	1.84 dB
	3.4GHz	83.0°	4.50 dBic	36.0°	3.76 dB	36.5°	4.48 dBic	2.24 dB
Case 2	3.2GHz	271.0°	3.94 dBic	34.5°	4.19 dB	28.0°	4.66 dBic	2.47 dB
	3.3GHz	268.0°	4.93 dBic	36.0°	3.68 dB	34.0°	3.27 dBic	4.55 dB
	3.4GHz	231.0°	5.25 dBic	29.0°	4.24 dB	46.5°	2.32 dBic	3.65 dB
Case 3	3.2GHz	188.0°	4.72 dBic	38.5°	4.63 dB	34.0°	3.34 dBic	2.93 dB
	3.3GHz	183.0°	4.73 dBic	35.5°	1.63 dB	41.0°	3.52 dBic	1.76 dB
	3.4GHz	178.0°	4.63 dBic	31.5°	1.25 dB	51.0°	1.56 dBic	1.63 dB

As expected the measured axial ratio are close to the 3-dB criteria indicating a relatively pure polarization is realized. The measured gain and axial ratio do not always agree well with the predicted ones, suggesting that the beams have shifted away from the simulated maximum beam directions. The discrepancy may due to the poor manual alignment of the azimuth angle with the simulated maximum φ. In addition, the biasing lines, pads, and open-circuit stubs, even though finely tuned, become radiating elements of the antenna and therefore some performance deterioration is inevitable.

5.4.4. CONCLUSIONS

A beam steering spiral antenna is realized using PIN diodes switches. Wide beam coverage is achieved around 3.3 GHz. Antenna parameters are measured at 3.2, 3.3 and 3.4 GHz. RHCP patterns are almost identical to the simulated patterns while a discrepancy occurs for LHCP ones. Although some discrepancies exist between the simulations and measurements, the present work clearly validates the proposed solution for a reconfigurable spiral antenna.

CHAPTER 6

FABRICATION PROCESSES

This chapter discusses the fabrications issues. These issues cover micromachining techniques and the processing problems encountered during the fabrication of RF MEMS switches. A seven masks MEMS integrated monolithic antenna fabrication procedure is proposed for the first time in the University of New South Wales. Major optimizations of the fabrication processes have also been demonstrated. All the discussion is based on the equipment available in Australia National Fabrication Facility (ANFF) labs in UNSW.

6.1. OVERVIEW

Micromachining plays a vital role in the vast progress of MEMS. It is a key to the door of creating micro-scale moveable complex structures on a substrate. The basic approach starts from material deposition, patterning with photolithography process and then removing the unwanted material through etching to form the shape of the structure.

6.1.1. MATERIAL ISSUES

Surface micromachining is widely used for the fabrication of RF MEMS switches. This technique allowing any metal which can be deposited as a film to be utilized for building the mechanical structure. The use of films in RF MEMS fabrication presents number of challenges due to their inherent properties. For each deposition method, the deposition parameters are optimized to control the deposition conditions which lead to the desired electrical as well as mechanical characteristics of metals.

Properties like residual stress and dielectric degradation are critical to the device operation. Any leakage or breakdown of the dielectric layer can lead to the device failure. Any residual stress particularly stress gradient for cantilever beam switches imparts a bending force that can affect the shape of the structure. Stress that develops during the deposition of film can lead to cracking, buckling or blistering.

6.1.2. PHYSICAL VAPOR DEPOSITION

Among different depositions methods, PVD is the most important one. The major advantage of PVD is that the deposition occurs in the line of sight from target directly to the substrate. Evaporation uses boiling or sublimation to obtain the vapors from a heated material (target) then the vapor forms a thin film on a cooler substrate located above the target. The boiling or sublimation is conducted in vacuum chamber. The vacuum reduces the chance of any undesirable reaction between vapored target material and atmospheric gases, the product of which will contaminate the deposited metal film. The film thickness is controlled by measuring the time of operation as well as the detecting crystal.

There are two types of commonly used metal evaporation techniques: the resistive and e-beam evaporation. Resistive evaporation is mainly used in the laboratories and e-beam evaporation is mostly used for the industrial application. In our fabrication process, both resistive and e-beam evaporation have been used. Resistive heating (or thermal evaporation) is one of the oldest and simplest way of depositing the thin metal layer. It utilize electrical current to heat a tungsten boat or filament that contains the target metal to vaporize the material. In the e-beam evaporation, a high intensity (3-20keV) electron beam gun is focused on the surface of the target metal held within the recess of a water cooled hearth. This electronic beam is magnetically directed and focused electrons to heat and melt the target material.

6.1.3. SPUTTERING DEPOSITION

In sputtering process, the target at a high negative potential is bombarded by argon ions created in plasma. The target metal atoms are sputtered away and ejected on the surface of the substrate forming a deposited film. The sputtered films result in superior adhesion as these ejected atoms with high ejection energies of 10-100eV can penetrate at least one to two atomic layers deep into the substrate surface. As compared to evaporated films which are mainly used for the lift-off process, the sputtered films are preferred when conformal films on high aspect ratio surface features are required.

6.1.4. ETCHING

Two methods are mainly used in material etching during the RF MEMS fabrication process: wet and dry etching. Wet etching is a technique for selectively etching a material away from the surface of a wafer with dedicated chemical solvent. During my process, I have used Au etchants to remove unwanted gold and hydrofluoric acid (HF) to clean oxide layer. Dry etching uses RF plasma and chemical etching to remove the materials. The hollow cathode RIE and Denton Vacuum Inc. PE-250 O2 plasma are used for etching polyimide and photoresist respectively.

6.2. MATERIAL CHOICES

6.2.1. CHOICE OF SUBSTRATE

The choice of the substrate depends on the application of the circuits as well as the fabrication feasibility of RF MEMS switches. The semiconducting substrates such as silicon have significantly high dielectric losses along with high conductive losses due to large number of free carriers in the doped material as compared to ceramic substrates. Especially for antenna applications, the losses will severely degrade the RF performance and the radiation gain, so silicon substrate is ruled out.

I have selected quartz substrate with low dielectric constant (ε_r=3.75) for the fabrication of the RF MEMS switches. These substrates were fabricated by CoorsTek Inc. with 99.6%

purity. The thickness of the substrate is 250μm and an extremely low loss tangent of 0.0001. Unlike the most of conventional antenna substrates, the quartz substrate is compatible with the well-established standard CMOS fabrication process, so the chemical agents can be used freely on the wafer.

6.2.2. METAL SELECTION

Metal selection is a critical step in overall switch design and fabrication to ensure compatibility with the fabrication process. Contact material should be selected carefully as its contact resistance is an important criterion. Other than that, metal sticking behavior, life time, environmental and packaging compatibility are also need to be taken into consideration. An ideal choice of metal should be a good conductor of electricity and resistance to oxidation.

Gold (Au) is a metal which is frequently proposed for the fabrication of these types of devices. Gold can be deposited using PVD or electroplating techniques and is compatible through the fabrication processes such as deposition, lithography and etching. Gold happened to be the most resistive metal to the oxidation. Only copper and silver are better than gold in terms of transferring of heat and electricity, but unlike these metals gold does not tarnish which makes it indispensable in electronics. For micro switches, gold is mostly used as a contact material for its superior conductivity and its compatibility with MMICs. Gold is selected due to its features.

6.3. SEVEN-MASK ANTENNA FABRICATION PROCESS

The fabrication of the RF MEMS switches loaded reconfigurable antenna is a seven mask all metal fabrication process as shown in figure 6.1. All processing steps are developed on the basis of standard CMOS processes. The fabrication is a seven-mask all metal process. The procedure starts with the standard wafer cleaning process. The double polished quartz wafer is used for frontside and backside fabrication. Backside gold ground planes and alignment marks are deposited by thermal evaporating 1 μm of gold layer. This layer is patterned with mask 1. Then we flip to the frontside and do the cleaning process again. DC biasing lines, electrodes and actuation pads are defined by thermal evaporating 110nm of Ge and patterning with mask 2. The Ge evaporation is done using Lesker evaporator operating under 10^{-6} Torr pressure. After deposition, the Ge layer is not conductive so we need to put it in the general purpose furnace to reform its crystal structure. The furnace is set to 500°C and the time is manually controlled to be around 5 minutes. The Ge layer is now conductive but with very high resistivity so it will not affect the antenna performance. A dielectric layer in a series switch serves as an electrical isolation between the electrode and the cantilever beam. A 50 nm SiO_2 layer is deposited as dielectric layer using Edward sputtering machine and patterned with mask 3. The antenna structure, impedance matching network and actuation pads (on top of Ge pads) are defined by thermal evaporating of 50nm/1μm thick layer of Ti/Au and patterned with mask 4. Ti is employed as an adhesion layer between the Au and the quartz substrate.

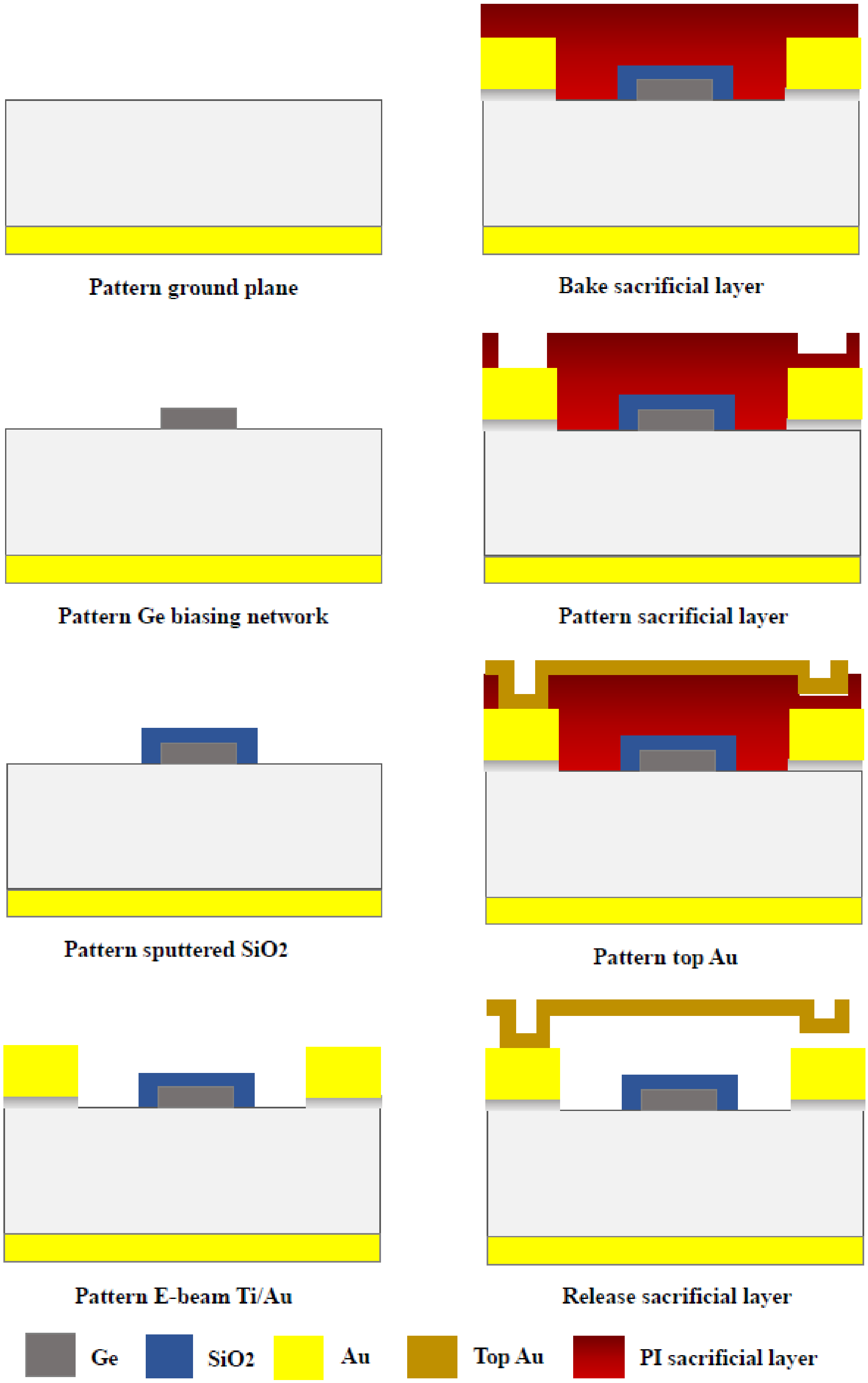

Figure 6.1. Seven-mask fabrication process for RF MEMS switches integrated antenna

After that, a 2.5μm thick layer of polyimide (PI) is span across the wafer as a sacrificial layer. The PI needs to be cured at 350°C for 30 minutes in the muffle furnace. Then a thick layer of photoresist is span and patterned for the anchor and dimple with mask 5and 6 respectively. This is followed by a 1 μm thick layer of E-beam evaporated Au which is patterned with mask 7 to form the cantilever beam. E-beam evaporator is used instead of thermal evaporator here because it can construct the beam with low residue stress this feature avoids peeling or cracking of the beam after it is released. Finally, the cantilever beam is released by using RIE dry etching release process.

A standard one layer photoresist (AZ2035) is used as a mask during the fabrication process to provide precise pattern definition. The AZ2035 photoresist is a negative photoresist sensitive to ultraviolet (UV) radiation and can be developed with AZ826 photoresist developer. Throughout the fabrication process, alignment is performed with Quintal Q-6000 mask aligner with UV light exposure.

6.4. FABRICATION PROCESS OPTIMIZATION

6.4.1. AZ2035 PHOTORESIST CHARACTERIZATION

The AZ2035 is a new type of photoresist which has never been used in the ANFF lab in UNSW. At first some bubble problem was encountered when developed the photoresist (shown in figure 6.2 (a)). The bubble problem is because of the humidity on the surface of substrate is not entirely expelled during the baking. Some of the bubbles were through the whole photoresist layer. This led to issue that the small pieces of metal were deposited on the unwanted area of the substrate. The problem has been solved by introducing dehydration process and extending the pre-bake time (figure 6.2 (b)). The mature photoresist process is demonstrated in table 6.1.

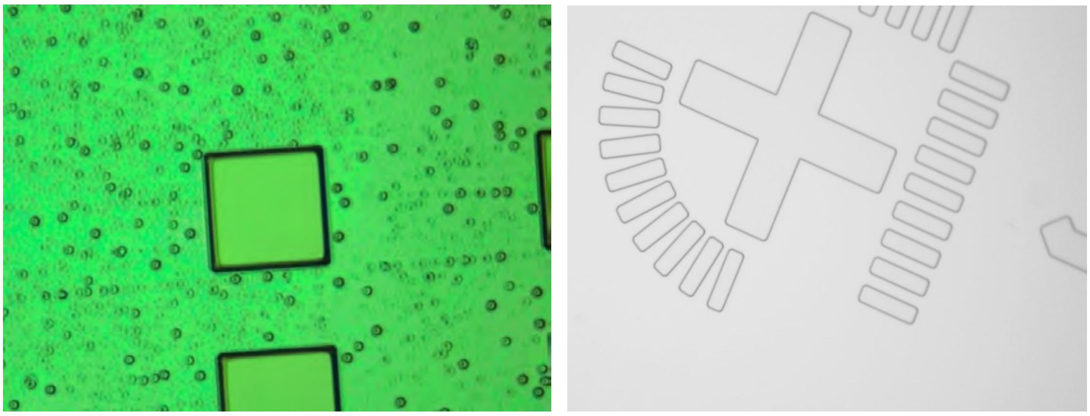

(a) **(b)**

Figure 6.2. Developed photoresist (a) standard CMOS process (b) optimized process

Table 6.1. Optimized photoresist process

Cleaning wafer	spin Acetone + IPA
Dehydration bake	3min @110°C, 1min cooling
Spin photoresist	30s @3000rpm, 3.4µm thickness 30s @2000rpm, 4.5µm thickness
Pre-baking	1min @110°C
exposure	8s under 10mw/ cm^2 UV light
Post-baking	1min @110°C
Develop	60s in AZ 826 MIF, DI water rinsing

6.4.2. LIFT OFF PROCESS

All the metal layers are patterned using lift-off process instead of wet etching. The lift-off process can provide clean edges of the structure. For wet etching process, the etching time need to be precisely controlled and the etchant left dentate edges that jeopardized the RF performance. During wet etching the gold is protected by a photoresist layer with same pattern, the gold etchant will etch down to the substrate and then etch sideway to undercut the gold underneath the photoresist protection layer. The wet etching results for a slightly longer time are shown in figure 6.3. As can be seen, the gold was etched inward, while the gold and the silver color Ti adhesion layer's edges were all attacked by the gold etchant. The rough edge problem is a big issue for wet etching due to that it will degrade the performance of the circuit.

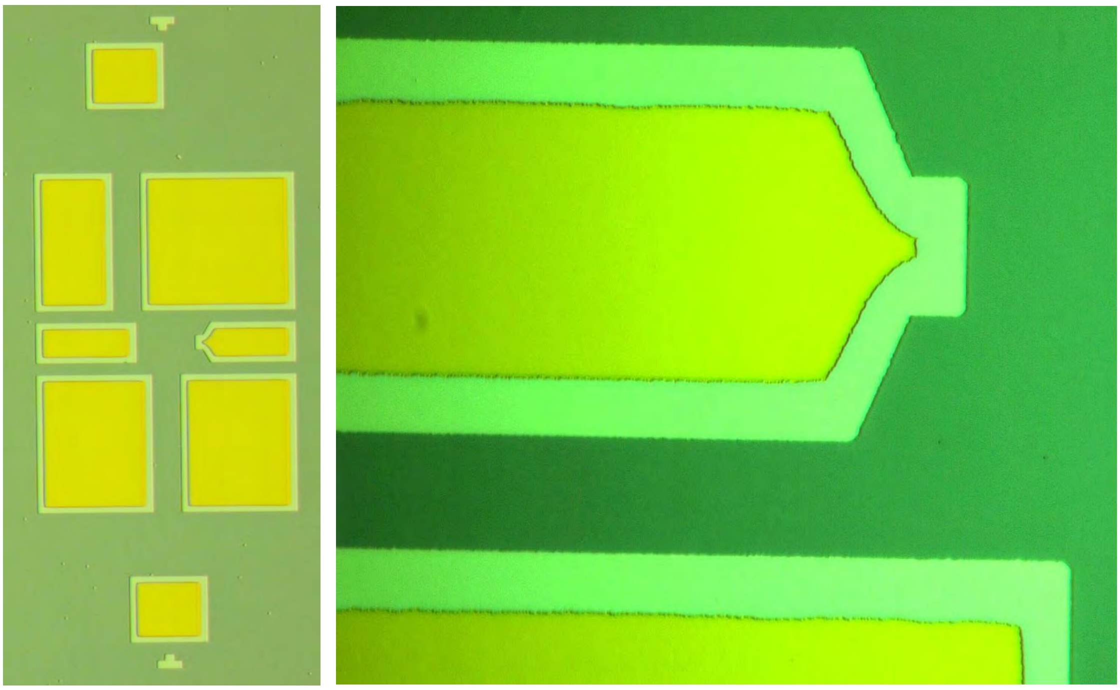

(a) **(b)**

Figure 6.3. Gold wet etching: (a) edges are undercut for slightly longer etching time (b) edges are not smooth

The lift-off process fully utilize the property of the negative photoresist to form clean edges on metal structures (shown in figure 6.4).

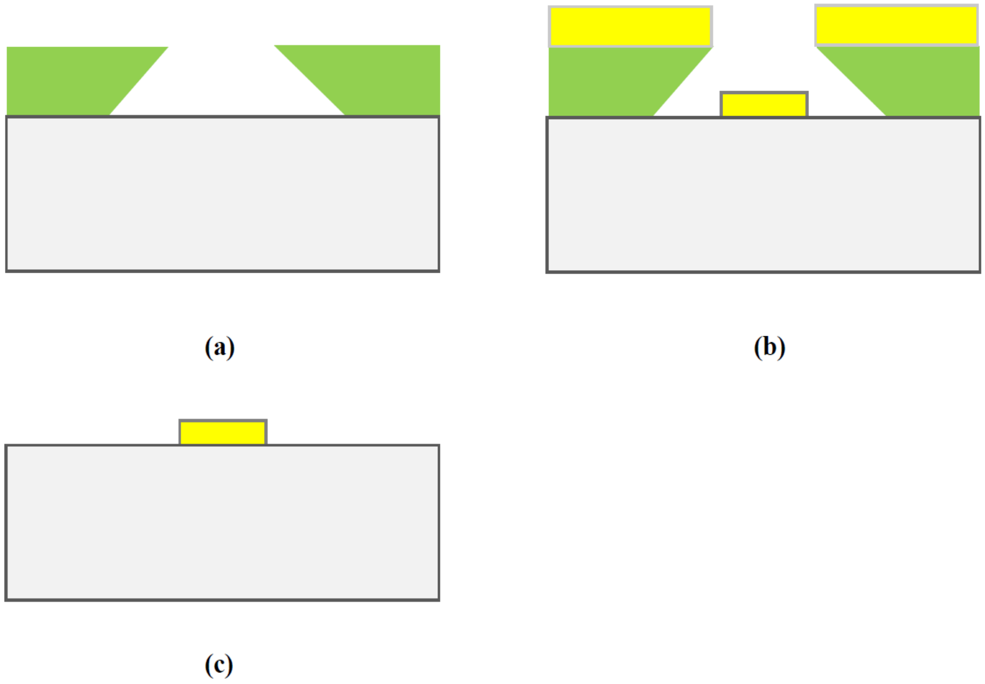

Figure 6.4. Negative PR lift-off process: (a) pattern the photoresist (b) deposit metal on the substrate (c) lift-off the unwanted metal using NMP solution

6.4.3. GERMANIUM ANNEALING CHARACTERIZATION

The Ge is first time introduced to the antennas biasing structure. The conductivity is studied by following procedure: pattern the substrate with photoresist, deposit the Ge using thermal evaporator and lift-off, heat it up in the general purpose furnace tube for certain time, take it out and wait it cooling down to the room temperature then measure the resistivity using four probe station. The data collected from the experiments are demonstrated in table 6.2.

Table 6.2. Ge resistivity measured by the four probe station

Ge 110nm patterned				
Temperature (degree)	Time (min)	Current reading (uA)	Voltage reading (mV)	Sheet resistance (Ohm/sq.)
400	60	not conductive		
450	12	not conductive		
	14	not conductive		
	15	not conductive		
	15	not conductive		
	15.5	not conductive		
	15.75	not conductive		
	16	45	271	27100
	16	45	373	37300
	20	45	186.3	18630
	25	45	831	83100
	34	45	18.3	1830
500	5	45	917	91700
	5	45	549	54900
	5	45	587	58700
	5	45	489	48900
	6.5	45	548	54800
	6.5	45	2870	287000
	8	45	479	47900

As can be seen from the table above, the data is relatively random but the resistivity can be maintain above 48900Ω/sq. for leaving the Ge in the furnace for 5 minutes at 500°C. This resistivity is sufficiently large for choking RF current that generating on the biasing lines. The reason for measuring the patterned Ge is that the unpatterned large Ge film has a different resistivity characteristic under the temperature.

6.4.4. SILICON DIOXIDE SPUTTERING

The silicon nitride is most commonly used as the dielectric layer, but the plasma enhanced chemical vapor deposition machine is offline in ANFF lab. So a substitution or silicon dioxide (SiO_2) is proposed for the dielectric layer using Edward sputtering machine. Unlike the thermal evaporation or the E-beam evaporation, the sputtering process is not directional, which means the sputtered SiO_2 will cover every corner and hard to be lift-off by NMP solution. We used to sputter 600nm of gold and failed to lift it off (figure 6.5).

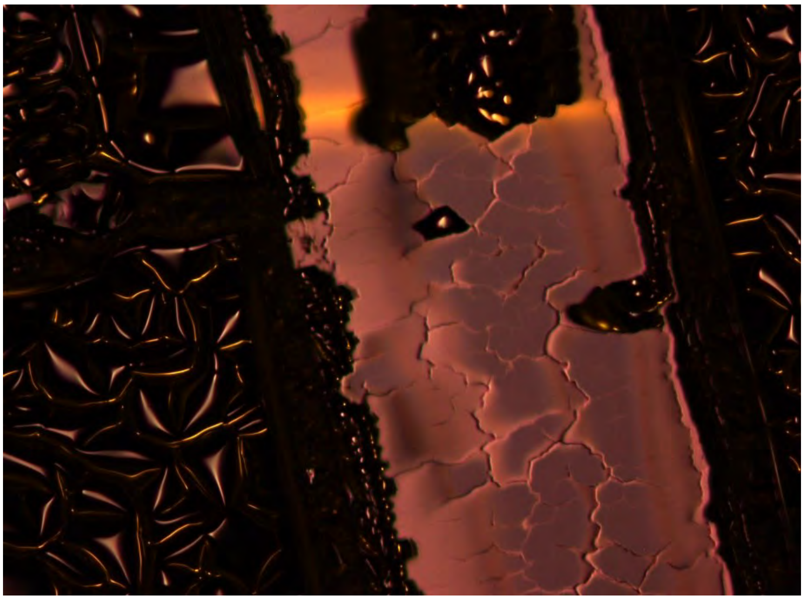

Figure 6.5. Gold lift-off failure

Fortunately, the 300nm thick SiO_2 layer can be successfully lift-off with smooth edges. The photographs of lift-off dielectric layers are shown in figure 6.6.

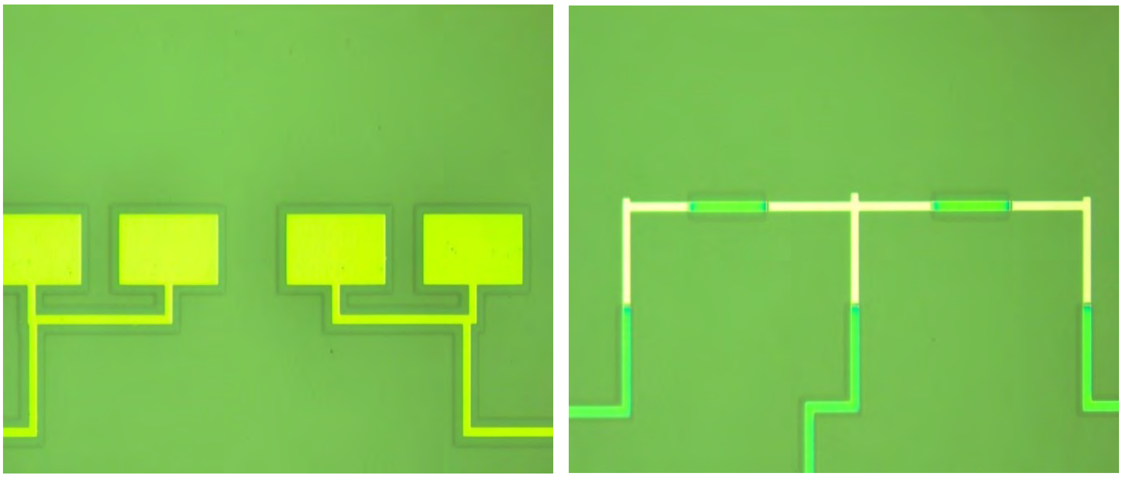

(a) **(b)**

Figure 6.6. Silicon dioxide patterns after lift-off process (a) the SiO2 layer covers the Ge biasing lines and electrodes (b) the SiO2 layer covers particular segment of the Ge biasing line

6.4.5. RIE RELEASING PROCESS

The sacrificial layer are commonly released by the O2 plasma asher. After several attempts, I found that the power of asher is not high enough to etch away the polyimide layer under the cantilever beam. So reactive ion etching (RIE) is proposed to release the RF MEMS switch. The process complete in two steps. In step one the etching is done using high power and low pressure (15sccm O2, 180 W, 8 Pa) giving an anisotropic etch of the polyimide around the cantilever. In step two low power and high pressure (15sccm O2, 50 W, 40 Pa) is used which resulted in isotropic etching of the polyimide underneath the beam thus giving a free standing structure at the end. The release holes were designed on the cantilever to assist the etching of the sacrificial layer underneath the beam.

6.5. CONCLUSIONS

In this chapter, fabrication processes of RF MEMS switches and related issues have been discussed. The quartz substrate and gold are chosen for their excellent electrical and mechanical properties. A seven-mask all metal fabrication process is presented. The annealed Ge conductivity is studied and results show that Ge is an ideal choice integrating biasing network into antenna structure while maintain its RF performance. The fabrication equipment and chemical agents used in the processes are detailed in the appendix. A self-written manual of how to operate all the fabrication machines is also attached in the appendix.

CHAPTER 7

CONCLUSIONS AND FUTURE WORKS

The contributions of this research work are summarized as conclusions. Several explored but uncompleted areas are suggested as the future and continuation work of this research.

7.1. CONTRIBUTIONS

The key contributions of this research work are outlined as follows.

- A 3-bit NEMS delay lines phase shifter has been designed, and optimized with good electrical performance. Multiple methods are introduced to solve the problems like high insertion loss of the transmission line, CPW bend phase error and impedance mismatch of the T-junction.
- Two types of slow wave structures were proposed and simulated. The slow wave structures can significantly reduce the manufacturing cost of microwave circuits because the cost of printed circuit is mainly decide by the chip size and the proposed slow wave structure managed to reduce the coupler size down to 28% and 39% respectively.
- Two new RF MEMS-integrated millimeter-wave frequency reconfigurable quasi-Yagi antenna was designed. The operation frequency of the antenna is switchable

between the millimeter wave 60 GHz WPAN band (57-66 GHz) and E-band (71-86 GHz) by actuating of the RF MEMS switches employed on the driven and director dipole elements. The end-fire radiation pattern of the Yagi antenna is maintained in both two-bands. As the 60 GHz band and E-band are becoming available in more and more countries, this technology can provide users with flexibility of enjoying the fast data transmission speed in both spectrum while reduce the noise when stay in one selected band. A resistive biasing configuration using silicon-chromium thin film is proposed. Simulation results have shown that it has small effect on the antenna reflection coefficient when the surface resistance is greater than 13.16 ohm/square.

- A microstrip-to-CPS transition design problem was unveiled by comparing two antenna structures using these baluns. Results show that certain type of microstrip-to-CPS transition cannot provide 180 degree phase change. So it is not suitable for the applications requires balanced input such as dipole or Yagi antennas. A new testing method is proposed to use Yagi antenna connected directly to the transition to test the phase balance. Also the directivity problem shed light on the possibility of using phase unbalanced transition to control the directivity of Yagi antenna forming pattern reconfigurable antenna.
- An innovative design method of pattern reconfigurable quasi-Yagi antenna were proposed. Experimental results have proved the feasibility of this methodology. The design principle and steps are provided. The designed RF MEMS-loaded

quasi-Yagi antenna's E-plane radiation beam is switchable between -15°, 0° and 15°by actuating of the RF MEMS switches employed on the driven dipole and transition delay line elements. The total coverage of monolithic antenna is from -54° to +58°, which is 31° more that the fixed single Yagi antenna while maintaining good reflection coefficient and realized gain at WPAN band (57 GHz – 66 GHz). This antenna is a competitor of the phased array. Compared to the large complex phased array, it has much smaller size and is easy to integrate with MMIC circuit. A germanium low conductivity biasing configuration is used in antenna structure for the first time. The low conductivity make the biasing network invisible to the antenna structure therefore guarantees the excellent radiation performance.

- A seven-mask all metal fabrication process is proposed for the first time for MEMS loaded reconfigurable antenna. The annealed Ge conductivity is studied and results show that Ge is an ideal choice integrating biasing network into antenna structure while maintain its RF performance. The fabrication processes and chemical agents used in the processes are presented.

7.2. FUTURE WORKS

- The designed slow wave structures are intended to fabricate using ink-jet printer with nano silver particle ink. The printing quality is still under testing and working procedure is not fully developed. So the next step work is to complete the fabrication process of this technology and get the first structure fabricated in UNSW.

- The designed MEMS loaded pattern reconfigurable antenna are being fabricating in the lab. The measurement need to be done as soon as possible to demonstrate the real world RF performance.

APPENDIX

Brief introduction of fabrication tools, materials and processes used during RF MEMS switches fabrication is presented as follows. The equipment is available in the ANFF lab, the University of New South Wales.

1. Photolithography equipment

i) Photo-mask

It is an optically flat glass or quartz plate with an absorber pattern metal that is opaque to light and is used to pattern photo-sensitive material on the surface of a wafer. A typical photo-mask consists of a thick Cr surface coated with photo-resist. The photo-mask which has been used in this fabrication is a 4×4 inch glass mask fabricated by Bandwidths foundry.

ii) Photoresist

It is a light sensitive material which is deposited on the surface of the wafer. Depending on the polarity of the photoresist (positive or negative), it is exposed to the UV light. During development, exposed positive resist area and unexposed area in case of negative photoresist is removed.

iii) PWM-32 Spinner

A tool used to coat the thin layer of photoresist on the surface of the wafer. The thickness of the photo-resist is controlled by the spin speed (rpm) of the spinner.

iv) Quintal Q-6000 Mask Aligner

The mask aligner is used to transfer the pattern from mask to the photo-resist on a wafer. The mask aligner aligns the photo-mask to a new or existing pattern on the wafer. The aligned mask and wafer are then exposed with UV light, transferring the pattern on the photoresist.

v) Thermoline Hot Plates

Hot plates are used for stirring the photo-resist during the pre- and post-bake process during the micro fabrication. Hot plates are portable and can be used with variable temperature limits.

vi) Pre-Bake or Soft Bake

Pre-bake is a process which partially removes the solvents present in a photoresist before aligning and exposing the wafer using a mask aligner.

vii) Photoresist Development

Developer is a chemical solution that will remove the exposed or unexposed area of the photo-resist after lithography process. The development procedure removes the exposed resist area in case of positive photo-resist and the unexposed area in case of negative photo-resist.

viii) Post-Bake or Hard Bake

Post-bake is a process which completely removes the solvents present in a photoresist and will solidify the photoresist after the develop process and before etching.

ix) Sacrificial Layer

It is a layer of material that separates the lower metal layer from the upper metal layer thus creating a gap between both the layers.

2. MATERIAL DEPOSITION SYSTEMS

x) Lesker evaporator

The Lesker evaporator works on resistive heating evaporation. In this method, current is passed through a tungsten boat or filament that contains the target metal and sublimate it.

xi) Solan/Varian E-Beam Evaporator

In this type of deposition, a high energy beam is used to evaporate the material from a source crucible. The evaporated material is ejected from the crucible and deposited in form of a thin film on the surface of a wafer.

xii) Edward Sputtering System

Sputtering is a process in which high energy plasma is used to bombard particles out of target metal. The target particles are ejected in a random direction giving a conformal coating on the substrate.

3. ETCHING TECHNIQUES

xiii) Dry Etch

This technique uses RF plasma and chemical etching to remove the materials from the surface of a wafer or a metal.

BIBLIOGRAPHY

[1] 2014, Teledyne Technologies Incorporated. Available: http://www.teledynerelays.com

[2] K. E. Petersen, "Micromechanical membrane switches on silicon," IBM J. Res. Dev, vol. 23, pp. 376-385, 1979.

[3] F. Assal, et al., "A Wide-Band Satellite Microwave Switch Matrix for SS/TDMA Communications," Selected Areas in Communications, IEEE Journal on, vol. 1, pp. 223-231, 1983.

[4] 2014, DowKey Microwave Corporation. Available: http://www.dowkey.com/

[5] 2014, L-3 Communications Corporation Narda Microwave - East. Available: http://www.nardamicrowave.com/east/index.php

[6] V. K. Varadan, et al., RF MEMS and Their Applications: John Wiley & Sons, 2003.

[7] M. B. Shifrin, et al., “Monolithic FET Structures for High-Power Control Component Applications,” IEEE Transactions on Microwave Theory and Techniques, Vol. 37, pp. 2134-2141, 1989.

[8] 2014, Skyworks Solutions, Inc. Available: http://www.skyworksinc.com/

[9] 2014, Advanced Control Components, Inc. Available: http://www.advanced-control.com/

[10] 2014, Advance Switch Technology. Available: http://www.astswitch.com/

[11] S. Lucyszyn, “Review of Radio Frequency Microelectromechanical Systems

Technology," IEEE Proc-Sci. Meas. Tech., Vol.151, No. 2, pp. 93-103, 2004.

[12] G. M. Rebeiz and J. B Muladavin, "RF MEMS Switches and Switch Circuits," IEEE Microwave Magazine, Vol. 2, No. 4, pp. 59-71, 2001.

[13] H. J. De Los Santos, "RF MEMS Circuit Design for Wireless Communications," Artech House, London, 2002.

[14] W. D. MaMalsche et al., "An Auto Injection System for Sub Micron Sized Channels used in Shear Driven Chromatography," J. of Royal Society of Chemistry (lab on a chip), Vol. 6, pp. 1322-1327, 2006.

[15] 2014, Home stuff Works, Available: http://www.howstuffworks.com/airbag.htm

[16] R. P. Feynman, "There's Plenty of Room at the Bottom," J. of Microelectromechanical Systems, Vol. 1, No. 1, pp. 60-66, 1992.

[17] 2014, Analog Devices, Inc., Available: http://www.analog.com/

[18] M. A. Basha, S. Chaudhari, S. S. Naeini, "A Rotating Micromirror Switching Element for 1×N Optical MEMS Switch," Proc. of IEEE Intl. Symp. on Micro-Nano Mechatronics and Human Sciences, Vol. 2, pp.901-903, 2004.

[19] P. M. Zavracky, et al., "Microswitches and Microrelays with a View toward Microwave Applications," J. of RF and Microwave Computer-Aided Engineering, Vol. 9, pp. 338-347, 1999.

[20] G. M. Whitesides, "The Origins and the Future of Microfluidics," J. of Nature, Vol. 442, No. 27, pp. 368-373, 2006.

[21] D. T. Kewley et al., "Plasma Etched Neural Probes," J. of Sensors and Actuators,

Vol. 58, No. 1, pp. 27-35, 1997.

[22] V. K. Varadan, K. J. Vinoy and K. A. Jose, “RF MEMS and Their Applications,” John Wiley & Sons, New York, 2003.

[23] J. A. Walranven, “Introduction to Applications and Industries for Microelectromechanical Systems (MEMS),” Proc. of IEEE ITC Intl. Test Conf., pp. 674-680, 2003.

[24] H. J. De Los Santos and R. J. Richards, “MEMS for RF/Microwave Wireless Applications: The Next Wave-Part II,” Microwave Journal, 2001.

[25] L. E. Larson, “Microwave MEMS Technology for Next Generation Wireless Communications,” IEEE MTT-S, Vol. 3, pp. 1073-1076, 1999.

[26] G. M. Rebeiz, “RF MEMS Theory, Design, and Technology,” John Wiley & Sons, New York, 2003.

[27] P. M. Zavracky, et al., "Microswitches and microrelays with a view toward microwave applications," International Journal of RF and Microwave Computer-Aided Engineering, vol. 9, pp. 338-347, 1999.

[28] C. Bozler, et al., "MEMS microswitch arrays for reconfigurable distributed microwave components," in Microwave Symposium Digest., 2000 IEEE MTT-S International, 2000, pp. 153-156 vol.1.

[29] R. E. Mihailovich, et al., "MEM relay for reconfigurable RF circuits," Microwave and Wireless Components Letters, IEEE, vol. 11, pp. 53-55, 2001.

[30] C. Chang and P. Chang, "Innovative micromachined microwave switch with very

low insertion loss," Sensors and Actuators. A, Physical, vol. 79. Lausanne, SUISSE: Elsevier, 2000.

[31] R. Meichun, et al., "Latching micromagnetic relays," Micro-electro-mechanical Systems, Journal of, vol. 10, pp. 511-517, 2001.

[32] D. Hyman, et al., "GaAs-compatible surface-micromachined RF MEMS switches," Electronics Letters, vol. 35, pp. 224-226, 1999.

[33] D. Hah, et al., "A low voltage actuated micromachined microwave switch using torsion springs and leverage," in Microwave Symposium Digest., 2000 IEEE MTT-S International, 2000, pp. 157-160 vol.1.

[34] J.-C. Chiao, et al., "MEMS millimeterwave components," in Microwave Symposium Digest, 1999 IEEE MTT-S International, 1999, pp. 463-466 vol.2.

[35] S.-D. Lee, et al., "An RF-MEMS Switch With Low-Actuation Voltage and High Reliability," Microelectromechanical Systems, Journal of, vol. 15, pp. 1605-1611, 2006.

[36] C. L. Goldsmith, et al., "Performance of low-loss RF MEMS capacitive switches," Microwave and Guided Wave Letters, IEEE [see also IEEE Microwave and Wireless Components Letters], vol. 8, pp. 269-271, 1998.

[37] D. Peroulis, et al., "MEMS devices for high isolation switching and tunable filtering," Microwave Symposium Digest., 2000 IEEE MTT-s International, 2000, pp. 1217-1220 vol.2.

[38] 2014, MEMSCAP Inc., Available: http://www.memscap.com/en_mumps.html

[39] 2014, Sandia national Laboratories, Available: http://www.mems.sandia.gov

[40] D. Girbau, et al., “RF MEMS Switches Based on the Buckle-beam Thermal Actuator,” Proc. of 33rd European Microwave Conference, 33rd European, 2003, pp. 651-654, 2003.

[41] L. Que, J. S. Park, Y. B. Gianchandani, “Bent-beam Electro-thermal Actuators for High Force Applications,” Proc. of IEEE Micro Electro Mechanical Systems (MEMS-1999), pp. 31–36, 1999.

[42] M. Daneshmand, et al., “Thermally Actuated Latching RF MEMS Switch and its Characteristics,” IEEE Transactions on Microwave Theory and Techniques, Vol. 57, pp. 3229-3238, 2009.

[43] Y. Zhang, et al., "Low-stress permalloy for magnetic MEMS switches," Magnetics, IEEE Transactions on, vol. 42, pp. 51-55, 2006.

[44] C. Il-Joo, et al., "A low-voltage and low-power RF MEMS series and shunt switches actuated by combination of electromagnetic and electrostatic forces," Microwave Theory and Techniques, IEEE Transactions on, vol. 53, pp. 2450-2457, 2005.

[45] A. Barzegar,R. Bagheri, A. Karimi Taheri, "Aging of piezoelectric composite transducers," Journal of Applied Physics , vol.89, no.4, pp.2322-2326, Feb 2001.

[46] H. C. Lee, et al., “Piezoelectrically Actuated RF MEMS DC Contact Switches with Low Voltage Operation,” IEEE Microwave and Wireless Components Letters, Vol. 15, pp. 202-204, 2005.

[47] R. G. Polcawich, et al., “Surface Micromachined Microelectromechancial Ohmic

Series Switch using Thin-Film Piezoelectric Actuators," IEEE Transactions on Microwave Theory and Techniques, Vol. 55, pp. 2642-2654, 2007.

[48] Q. M. Zhang, J. Zhao, L. E. Cross, "Aging of the Dielectric and Piezoelectric Properties of Relaxor Ferroelectric Lead Magnesium Niobate–Lead Titanate in the Electric Field Biased State," J. of Applied Physics, Vol.79, No.6, pp. 3181-3187, 1996.

[49] A. Barzegar, R. Bagheri, A. K. Taheri, "Aging of Piezoelectric Composite Transducers," J. of Applied Physics, Vol.89, No.4, pp. 2322-2326, 2001.

[50] I. D. Robertson, S. Lucyszyn, RFIC and MMIC Design and Technology. London: IET, 2001.

[51] J. S. Hayden, G. M. Rebeiz, "Low-loss cascadable MEMS distributed X-band phase shifters," Microwave and Guided Wave Letters, IEEE , vol.10, no.4, pp.142-144, Apr 2000

[52] G. Tan, R. E. Mihailovich, J. B. Hacker, J. F. DeNatale, G. M. Rebeiz, "Low-loss 2- and 4-bit TTD MEMS phase shifters based on SP4T switches," Microwave Theory and Techniques, IEEE Transactions on, vol.51, no.1, pp. 297- 304, Jan 2003.

[53] A. Borgioli, Y. Liu, A. S. Nagra, R. A. York, "Low-loss distributed MEMS phase shifter," Microwave and Guided Wave Letters, IEEE, vol.10, no.1, pp.7-9, Jan 2000.

[54] Y. Liu, A. Borgioli, A. S. Nagra, R. A. York, "K-band 3-bit low-loss distributed MEMS phase shifter," Microwave and Guided Wave Letters, IEEE, vol.10, no.10, pp.415-417, Oct 2000.

[55] B. Lakshminarayanan, T. M. Weller, "Optimization and Implementation of Impedance-Matched True-Time-Delay Phase Shifters on Quartz Substrate," Microwave Theory and Techniques, IEEE Transactions on , vol.55, no.2, pp.335-342, Feb. 2007

[56] Tan, Guan-Leng; Mihailovich, R.E.; Hacker, J.B.; DeNatale, J.F.; Rebeiz, G.M., "A 2-bit miniature X-band MEMS phase shifter," Microwave and Wireless Components Letters, IEEE , vol.13, no.4, pp.146,148, April 2003

[57] Songbin Gong; Hui Shen; Barker, N.S., "A 60-GHz 2-bit Switched-Line Phase Shifter Using SP4T RF-MEMS Switches," Microwave Theory and Techniques, IEEE Transactions on , vol.59, no.4, pp.894,900, April 2011

[58] J. Park, H. Kim, W. Choi, Y. Kwon, Y. Kim, "V-band reflection-type phase shifters using micromachined CPW coupler and RF switches," Microelectromechanical Systems, Journal of , vol.11, no.6, pp. 808- 814, Dec 2002

[59] J. Kim, S. Lee, J. Park, C. Baek, Y. Kwon, Y. Kim, "A 5-17 GHz wideband reflection-type phase shifter using digitally operated capacitive MEMS switches," TRANSDUCERS, Solid-State Sensors, Actuators and Microsystems, 12th International Conference on, 2003, pp. 907-910 vol.1, 8-12 June 2003

[60] A. Malczewski, S. Eshelman, B. Pillans, J. Ehmke, C. L. Goldsmith, "X-band RF MEMS phase shifters for phased array applications," Microwave and Guided Wave Letters, IEEE, vol.9, no.12, pp.517-519, Dec 1999.

[61] S. Barker, G. M. Rebeiz, "Distributed MEMS true-time delay phase shifters and

wide-band switches," Microwave Theory and Techniques, IEEE Transactions on , vol.46, no.11, pp.1881-1890, Nov 1998

[62] J. S. Hayden, G. M. Rebeiz, "2-bit MEMS distributed X-band phase shifters," Microwave and Guided Wave Letters, IEEE, vol.10, no.12, pp.540-542, Dec 2000.

[63] H. K. Kim, J. H. Park, S. Lee, S. Kim, J. Kim, Y. Kim, Y. Kwon, "V-band 2-b and 4-b lowloss and low-voltage distributed MEMS digital phase shifter using metal-air-metal capacitors," Microwave Theory and Techniques, IEEE Transactions on, vol.50, no.12, pp.2918- 2923, Dec 2002.

[64] J. S. Hayden, G. M. Rebeiz, "Very low-loss distributed X-band and Ka-band MEMS phase shifters using metal-air-metal capacitors," Microwave Theory and Techniques, IEEE Transactions on, vol.51, no.1, pp. 309- 314, Jan 2003.

[65] C. Esta, K. Dombrowski, V. Brankovic, D. Radovic, "Antenna solutions for UWB communication devices in 60GHz range," in Future Network and Mobile Summit, 2010.

[66] URL:http://www.bridgewave.com/wireless_products/60-Ghz-wirelessoverview.html.

[67] Panagamuwa, C.J., Chauraya, A., and Vardaxoglou, J.C., “Frequency and beam reconfigurable antenna using photoconducting switches,” IEEE Transactions on Antennas and Propagation, vol. 54, pp. 449–454, February 2006.

[68] Freeman, J.L., Lamberty, B.J., and Andrews, G.S., “Optoelectronically reconfigurable monopole antenna,” Electronics Letters, vol. 28, no. 16, pp. 1502–

1503, July 1992.

[69] Kiriazi, J., Ghali, H., Radaie, H., and Haddara, H., “Reconfigurable dual-band dipole antenna on silicon using series MEMS switches,” Proceedings of the IEEE/URSI International Symposium on Antennas and Propagation, vol. 1, pp. 403–406, 2003.

[70] Roscoe, D.J., Shafai, L., Ittipiboon, A., Cuhaci, M., and Douville, R., “Tunable dipole antennas,” Proceedings of the IEEE/URSI International Symposium on Antennas and Propagation, vol. 2, pp. 672–675, 1993. doi:10.1109/APS.1993.385257

[71] Weedon, W.H., Payne, W.J., and Rebeiz, G.M., “MEMS-switched reconfigurable antennas,” Proceedings of the IEEE/URSI International Symposium on Antennas and Propagation, vol.3, pp. 654–657, 2001.

[72] Weedon, W., Payne, W., Rebeiz, G., Herd, J., and Champion, M., “MEMS-switched reconfigurable multi-band antenna: Design and modeling,” Proceedings of the 1999 Antenna Applications Symposium, vol. 1, pp. 203–231, 1999.

[73] Brown, E.R., “On the gain of a reconfigurable-aperture antenna,” IEEE Transactions on Antennas and Propagation, vol. 49, pp. 1357–1362, October 2001.

[74] Ali, M.A., and Wahid, P., “A reconfigurable Yagi array for wireless applications,” Proceedings of the IEEE/URSI International Symposium on Antennas and Propagation, vol. 1, pp. 466–468, 2002.

[75] Anagnostou, D., Chryssomallis, M.T., Lyke, J.C., and Christodoulou, C.G., “Re-

configurable Sierpinski gasket antenna using RF-MEMS switches," Proceedings of the IEEE/URSI International Symposium on Antennas and Propagation, vol. 1, pp. 375–378, 2003.

[76] Anagnostou, D.E., Zheng, G., Chryssomallis, M.T., Lyke, J.C., Ponchak, G.E., Papapolymerou, J., and Christodoulou, C.G., "Design, fabrication, and measurements of an RFMEMS–based self-similar reconfigurable antenna," IEEE Transactions on Antennas and Propagation, vol. 54, no. 2, pp. 422–432, February 2006.

[77] Gupta, K.C., Li, J., Ramadoss, R., and Wang, C., "Design of frequency-reconfigurable slot ring antennas," Proceedings of the IEEE/URSI International Symposium on Antennas and Propagation, vol. 1, p. 326, 2000.

[78] Peroulis, D., Sarabandi, K., and Katehi, L.P.B., "Design of reconfigurable slot antennas," IEEE Transactions on Antennas and Propagation, vol. 53, pp. 645–654, February 2005.

[79] Huff, G.H., and Bernhard, J.T., "Frequency reconfigurable CPW-fed hybrid folded slot/slot dipole antenna," Proceedings of the IEEE/ACES International Conference on Wireless Communications and Applied Computational Electromagnetics, pp. 574–577, 2005.

[80] Kawasaki, S., and Itoh, T., "A slot antenna with electronically tunable length," Proceedings of the IEEE/URSI International Symposium on Antennas and Propagation, vol. 1, pp. 130–133, 1991.

[81] Behdad, N., and Sarabandi, K., “A varactor-tuned dual-band slot antenna,” IEEE Transactions on Antennas and Propagation, vol. 54, pp. 401–408, February 2006.

[82] Behdad, N., and Sarabandi, K., “Dual-band reconfigurable antenna with a very wide tenability range,” IEEE Transactions on Antennas and Propagation, vol. 54, pp. 409–416, February2006.

[83] Erdil, E., Topalli, K., Unlu, M., Civi, O.A., and Akin, T., “Frequency tunable microstrip patch antenna using RF MEMS technology,” IEEE Transactions on Antennas and Propagation, vol. 54, pp. 1193–1196, April 2007.

[84] Kiely, E., Washington, G., and Bernhard, J.T., “Design and development of smart microstrip patch antennas,” Smart Materials and Structures, vol. 7, no. 6, pp. 792–800, December 1998.

[85] Kiely, E., Washington, G., and Bernhard, J.T., “Design, actuation, and control of active patch antennas,” Proceedings of the SPIE International Society for Optical Engineering, vol. 3328, pp.147–155, 1998.

[86] Bernhard, J.T., Kiely, E., and Washington, G., “A smart mechanically-actuated two-layer electromagnetically coupled microstrip antenna with variable frequency, bandwidth, and antenna gain,” IEEE Transactions on Antennas and Propagation, vol. 49, pp. 597–601, April 2001.

[87] Langer, J.-C., Zou, J., Liu, C., and Bernhard, J.T., “Reconfigurable out-of-plane microstrip patch antenna using MEMS plastic deformation magnetic actuation,” IEEE Microwave and Wireless Components Letters, vol. 13, pp. 120–122, March

2003.

[88] Pozar, D.M., and Sanchez, V., “Magnetic tuning of a microstrip antenna on a ferrite substrate,” Electronics Letters, vol. 24, pp. 729–731, June 9, 1988.

[89] Mishra, R.K., Pattnaik, S.S., and Das, N., “Tuning of microstrip antenna on ferrite substrate,” IEEE Transactions on Antennas and Propagation, vol. 41, pp. 230–233, February 1993.

[90] Brown, A.D., Volakis, J.L., Kempel, L.C., and Botros, Y., “Patch antennas on ferromagnetic substrates,” IEEE Transactions on Antennas and Propagation, vol. 47, pp. 26–32, January 1999.

[91] Romanofsky, R.R., Miranda, F.A., Van Keuls, F.W., and Valerio, M.D., “Recent advances in microwave applications of thin ferroelectric films at the NASA Glenn Research Center,” Materials Research Society Symposium Proceedings, vol. 833, pp. 173–181, 2004.

[92] Miranda, F.A., Van Keuls, F.W., Romanofsky, R.R., Mueller, C.H., Alterovitz, S., and Subramanyam, G., “Ferroelectric thin films-based technology for frequency- and phase-agile microwave communication applications,” Integrated Ferroelectrics, vol. 42, pp. 131–149, 2002.

[93] Xu, H., Pervez, N.K., and York, R.A., “Tunable microwave integrated circuits BST thin film capacitors with device structure optimization,” Integrated Ferroelectrics, vol. 77, pp. 27–35, 2005.

[94] Clarricoats, P.J.B., and Zhou, H., “The design and performance of a reconfigurable

mesh reflector antenna," IEE Seventh International Conference on Antennas and Propagation, vol. 1, pp. 322–325, 1991.

[95] Clarricoats, P.J.B., Zhou, H., and Monk, A., "Electronically controlled reconfigurable reflector antenna," Proceedings of the IEEE/URSI International Symposium on Antennas and Propagation, vol. 1, pp. 179–181, 1991.

[96] Sievenpiper, D., Schaffner, J., Lee, J.J., and Livingston, S., "A steerable leaky-wave antenna using a tunable impedance ground plane," IEEE Antennas and Wireless Propagation Letters, vol. 1, pp. 179–182, 2002.

[97] Sievenpiper, D., and Schaffner, J., "Beam steering microwave reflector based on electrically tunable impedance surface," Electronics Letters, vol. 38, no. 21, pp. 1237–1238, October 10, 2002.

[98] Sievenpiper, D.F., "Forward and backward leaky wave radiation with large effective aperture from an electronically tunable textured surface," IEEE Transactions on Antennas and Propagation, vol. 53, pp. 236–247, January 2005.

[99] Chang, K., Li, M., Yun, T.-Y., and Rodenbeck, C.T., "Novel low-cost beam steering techniques," IEEE Transactions on Antennas and Propagation, vol. 50, pp. 618–627, May 2002.

[100] Rodenbeck, C.T., Li, M., and Chang, K., "Design and analysis of a reconfigurable dual-beam grating antenna for low-cost millimeter-wave beam-steering," IEEE Transactions on Antennas and Propagation, vol. 52, pp. 999–1006, April 2004.

[101] Nikolaou, S., Bairavasubramanian, R., Lugo, Jr., C., Carrasquillo, I., Thompson,

D.C., Ponchak, G.E., Papapolymerou, J., and Tentzeris, M.M., “Pattern and frequency reconfigurable annular slot antenna using PIN diodes,” IEEE Transactions on Antennas and Propagation, vol. 54, pp. 439–448, February 2006.

[102] Zhang, S., Huff, G.H., Feng, J., and Bernhard, J.T., “A pattern reconfigurable microstrip parasitic array,” IEEE Transactions on Antennas and Propagation, vol. 52, pp. 2773–2776, October 2004.

[103] Zhang, S., A Pattern Reconfigurable Microstrip Parasitic Array: Theory, Design, and Applications, PhD dissertation, University of Illinois at Urbana–Champaign, 2005.

[104] Dinger, R.J., “Reactively steered adaptive array using microstrip patch elements at 4GHz,” IEEE Transactions on Antennas and Propagation, vol. 32, pp. 848–856, August 1984.

[105] Dinger, R.J., “A planar version of a 4.0 GHz reactively steered adaptive array,” IEEE Transactions on Antennas and Propagation, vol. 34, pp. 427–431, March 1986.

[106] Schlub, R., Lu, J., and Ohira, T., “Seven-element ground skirt monopole ESPAR antenna design from a genetic algorithm and finite element method,” IEEE Transactions on Antennas and Propagation, vol. 51, no. 11, pp. 3033–3039, November 2003.

[107] Lovat, G., Burghignoli, P., and Celozzi, S., “A tunable ferroelectric antenna for fixedfrequency scanning applications,” IEEE Antennas and Wireless Propagation Letters, vol. 5, pp. 353–356, 2006.

[108] Yashchyshyn, Y., and Modelski, J.W., “Rigorous analysis and investigations of the scan antennas on a ferroelectric substrate,” IEEE Transactions on Microwave Theory and Techniques, vol. 53, pp. 427–438, February 2005.

[109] Varadan, V.K., Varadan, V.V., Jose, K.A., and Kelly, J.F., “Electronically steerable leaky wave antenna using a tunable ferroelectric material,” Smart Materials and Structures, vol. 3, pp. 470–475, 1994.

[110] Iskander, M.F., Zhang, Z., Yun, Z., Jensen, R., and Redd, S., “Design of a low-cost 2-D beam-steering antenna using ferroelectric material and CTS technology,” IEEE Transactions on Microwave Theory and Techniques, vol. 49, pp. 1000–1003, May 2001.

[111] Borowick, J., and Stern, R., “A line source array for limited scan applications,” Proceedings of the IEEE/URSI International Symposium on Antennas and Propagation, vol. 1, pp. 164–167, October 1976.

[112] N. S. Barker, "The future of N/MEMS," Microwave Magazine, IEEE, vol.8, no.6, pp.52-55, Dec. 2007.

[113] M. Abdelmoneum, D. Browning, T. Arabi, W. Khalil, "Micro and Nano Electro Mechanical Systems (MEMS/NEMS) for Mobile Computing Systems," Vehicular Technology Conference Fall (VTC 2009-Fall), 2009 IEEE 70th, pp.1-4, 20-23, Sept. 2009.

[114] R. L. Badzey, G. Zolfagharkhani, A. Gaidarzhy, P. Mohanty, "A controllable nanomechanical memory element," Applied Physics Letters, vol.85, no.16,

pp.3587-3589, Oct. 2004.

[115] M. Dequesnes, S. V. Rotkin, N. R. Aluru, "Calculation of pull-in voltages for carbon-nanotube-based nanoelectromechanical switches," Nanotechnology, vol.13, no.1, pp.120-131, Jan. 2002.

[116] K. L. Ekinci, and M. L. Roukes, "Nanoelectromechanical systems," Review of Scientific Instruments, vol.76, no.6, pp.061101-061101-12, June 2005.

[117] V. K. Varadan, K. J. Vinoy and K. A. Jose, RF MEMS and their applicatoins. New York: Wiley, 2003.

[118] G. M. Rebeiz, RF MEMS Theory, Design, and Technology. New York: Wiley, 2003.

[119] K. R. Jha, G. Singh, "Analysis of Dielectric Permittivity and Losses of Two-layer Substrate Materials for Microstrip Antenna at THz Frequency," Advances in Recent Technologies in Communication and Computing, 2009. ARTCom '09, pp.672-675, 27-28 Oct. 2009.

[120] K. R. Jha, and G. Singh, "Microstrip patch antenna on photonic crystal substrate at terahertz frequency," Applied Electromagnetics Conference (AEMC), 2009, pp.1-4, 14-16, Dec. 2009.

[121] J. Cong, M. Chang, G. Reinman, S. Tam, “Multiband RF-interconnect for reconfigurable network-on-chip communications,” International Workshop on System Level Interconnect Prediction, SLIP '09, pp.107-108, 2009.

[122] H. Rahman, K. Y. Chan, Y. Yang, and R. Ramer, “Fabrication of RF NEMS Series Switch Using Surface Micromachining”, in Proc. Of IASTED Technology

Conference, pp.1-7, 2010.

[123] R. N. Simons, Coplanar Waveguide Circuits, Components, and Systems, 1st ed. New York: Wiley, 2001.

[124] J. S. Hong and M. J. Lancaster, Microstrip Filters for RF/Microwave Applications. New York: Wiley, 2001.

[125] L. Zhu, "Guided-wave characteristics of periodic coplanar waveguides with inductive loading-unit-length transmission parameters," IEEE Trans. Microw. Theory Techn., vol. 51, no. 10, pp. 2133–2138, Oct. 2003.

[126] T. S. D. Cheung and J. R. Long, "Shielded passive devices for silicon based monolithic microwave and millimeter-wave integrated circuits," IEEE J. Solid-State Circuits, vol. 41, no. 5, pp. 1183–1200, May 2006.

[127] D. Kaddour, H. Issa, A. L. Franc, N. Corrao, E. Pistono, F. Podevin, J. M. Fournier, J. M. Duchamp, and P. Ferrari, "High- slow-wave coplanar transmission lines on 0.35 m CMOS process," IEEE Microw. Wireless Compon. Lett., vol. 19, no. 9, pp. 542–544, Sep. 2009.

[128] A. A. M. Ali, H. B. El-Shaarawy, and H. Aubert, "Miniaturized hybrid ring coupler using electromagnetic bandgap loaded ridge substrate integrated waveguide," IEEE Microw. Wireless Compon. Lett., vol. 21, no. 9, pp. 471–473, Sep. 2011.

[129] C. K. Wu, H. S. Wu, and C. K. C. Tzuang, "Electric–magnetic–electric slow-wave microstrip line and bandpass filter of compressed size," IEEE Trans. Microw. Theory Techn., vol. 50, no. 8, pp. 1996–2004, Aug. 2002.

[130] Y. Yun, "A novel microstrip-line structure employing a periodically perforated ground metal and its application to highly miniaturized and low-impedance passive components fabricated on GaAs MMIC," IEEE Trans. Microw. Theory Techn., vol. 53, no. 6, pp. 1951–1959, Jun. 2005.

[131] Y. Zhang and H. Y. D. Yang, "Ultra slow-wave periodic transmission line using 3-D substrate metallization," in IEEE MTT-S Int. Microw. Symp. Dig., pp. 891–894, Jun. 2008.

[132] S. K. Srivastava and S. P. Ojha, "Reflection and anomalous behavior of refractive index in defect photonic bandgap structure," Microw. Opt. Technol. Lett., vol. 38, no. 4, pp. 293–297, Aug. 2003.

[133] J. S. Hong and M. J. Lancaster, "A novel microwave periodic structure-the ladder microstrip line," Microw. Opt. Technol. Lett., vol. 9, no. 4, pp. 207–210, Jul. 1995.

[134] V. Radisic, Y. Qian, R. Coccioli, and T. Itoh, "Novel 2-D photonic bandgap structure for microstrip lines," IEEE Microw. Guided Wave Lett., vol. 8, no. 2, pp. 69–71, Feb. 1998.

[135] F. R. Yang, K. P. Ma, Y. Qian, and T. Itoh, "A uniplanar compact photonic-bandgap (UC-PBG) structure and its applications for microwave circuits," IEEE Trans. Microw. Theory Techn., vol. 47, no. 8, pp. 1509–1514, Aug. 1999.

[136] C. S. Kim, J. S. Park, D. Ahn, and J. B. Lim, "A novel 1-D periodic defected ground structure for planar circuits," IEEE Microw. Guided Wave Lett., vol. 10, no. 4, pp. 131–133, Apr. 2000.

[137] Q. Xue, K. M. Shum, and C. H. Chan, "Novel 1-D microstrip PBG cells," IEEE Microw. Guided Wave Lett., vol. 10, no. 10, pp. 403–405, Oct. 2000.

[138] G. A. Lee, H. Y. Lee, and F.De Flaviis, "Perforatedmicrostrip structure for miniaturising microwave devices," Electron. Lett., vol. 38, no. 15, pp. 800–801, Jul. 2002.

[139] K. W. Eccleston and S. H. M. Ong, "Compact planar microstripline branch-line and rat-race couplers," IEEE Trans. Microw. Theory Techn., vol. 51, no. 10, pp. 2119–2125, Oct. 2003.

[140] K. O. Sun, S. J. Ho, C. C. Yen, and D. van der Weide, "A compact branch-line coupler using discontinuous microstrip lines," IEEE Microw. Wireless Compon. Lett., vol. 15, no. 8, pp. 519–520, Aug. 2005.

[141] J. Wang, B. Z. Wang, Y. X. Guo, L. C. Ong, and S. Xiao, "A compact slow-wave microstrip branch-line coupler with high performance," IEEE Microw. Wireless Compon. Lett., vol. 17, no. 7, pp. 501–503, Jul. 2007.

[142] W. S. Chang and C. Y. Chang, "Novel microstrip periodic structure and its application to microwave filter design," IEEE Microw. Wireless Compon. Lett., vol. 21, no. 3, pp. 124–126, Mar. 2011.

[143] J. Q. Huang, Q. X. Chu, and H. Z. Yu, "A mixed-lattice slow-wave transmission line," IEEE Microw. Wireless Compon. Lett., vol. 22, no.1, pp. 13–15, Jan. 2012.

[144] 2014, Methode Electronics, Inc. Available: http://www.methode.com/

[145] V. Dyadyuk, J. Bunton, J. Pathikulangara, R. Kendall, O. Sevimli, L. Stokes, and

D. Abbott, “A multi-gigabit mm-wave communication system with improved spectral efficiency,” IEEE Trans. Microwave Theory Tech., vol. 55, no. 12, pp. 2813–2821, Dec. 2007.

[146] Gabriel M. Rebeiz, “RF MEMS Switches: status of the technology,” The 12th International Conference on Solid State Sensors, Actuators and Microsystems, Boston, June 8-12, 2003, pp. 1726-1729.

[147] P.D. Grant, M.W. Denhoff, and R.R. Mansour, “A Comparison Between RF MEMS Switches and Semiconductor Switches,” Proceedings of International Conference on MEMS, NANO and Smart Systems, 25-27 Aug. 2004, Banff, Canada.

[148] C. Palego, A. Pothier, A. Crunteanu, and P. Blondy, “A dual-band MEMS reconfigurable filter for a multi-standard radio front-end,” Proceedings of the 38th European Microwave Conference, pp.587-590, Amsterdam, The Netherlands, October 2008.

[149] Gabriel M. Rebeiz, Guan-Leng Tan, and Joseph S. Hayden, “RF MEMS Phase shifters: design and applications,” IEEE Microwave Magazines, pp.72-81, June 2002.

[150] K. Y. Chan, M. Daneshmand, R. R. Mansour, R. Ramer, "Scalable RF MEMS Switch Matrices: Methodology and Design," IEEE Trans. on Microwave Theory Tech., vol. 57, no. 6, pp. 1612-1621, 2009.

[151] Bedri A. Cetiner, Gemma Roqueta Crusats, Lluís Jofre, and Necmi Bıyıklı, “RF MEMS Integrated Frequency Reconfigurable Annular Slot Antenna,” IEEE Trans.

Antennas Propag., vol. 58, no. 3, pp. 626-632, 2010.

[152] D. E. Anagnostou, Guizhen Zheng, M. T. Chryssomallis, J. C. Lyke, G. E. Ponchak, John Papapolymerou, and C. G. Christodoulou, “Design, Fabrication, and Measurements of an RF-MEMS-Based Self-Similar Reconfigurable Antenna,” IEEE Trans. Antennas Propag., vol. 54, no. 2, pp. 422-432, 2006.

[153] W. R. Deal, N. Kaneda, J. Sor, Y. Qian and T. Itoh, “A new quasi-Yagi antenna for planar active antenna arrays,” IEEE Trans. Microw. Theory Tech., vol. 48, no. 6, pp. 910-918, June 2000.

[154] N. Nikolic and A. R. Weily, “Printed quasi-Yagi antenna with folded dipole driver,” in IEEE AP-S Int. Symp. Dig., 2009.

[155] Robert K. Waits, “Sputtered Silicon – Chromium Resistive Films”, Journal of Vacuum Science and Technology, vol. 6, no. 2, pp.308-315, 1969.

[156] W.-H. Tu and K. Chang, “Wide-band microstrip-to-coplanar stripline/slotline transitions,” IEEE Trans. Microw. Theory Tech., vol. 54, no. 3, pp. 1084–1089, Mar. 2006.

[157] ANSYS HFSS Version 15, Pittsburgh, PA, ANSYS Corporation.

[158] Robert K. Waits, “Sputtered Silicon – Chromium Resistive Films”, Journal of Vacuum Science and Technology, vol. 6, no. 2, pp.308-315, 1969.

[159] J. T. Bernhard, K. Chang, “Reconfigurable antennas," in The Wiley Encyclopedia of RF and Microwave Engineering. New York: Wiley, Feb. 2005.

[160] A. R. Weily et al., "A reconfigurable high-gain partially reflecting surface antenna,"

IEEE Trans. Antennas Propagat., vol.56, no. 11, pp. 3382-3390, Nov. 2008.

[161] W. R. Deal et al., “A new quasi-Yagi antenna for planar active antenna arrays,” IEEE Trans. Microw. Theory Tech., vol. 48, no. 6, pp. 910–916, Jun. 2000.

[162] H. K. Kan et al., “Simple broadband planar CPW-fed quasi-Yagi antenna,” IEEE Antennas Wireless Propag. Lett., vol. 6, 2007, pp. 18–20.

[163] P. D. Grant et al., “A Comparison Between RF MEMS Switches and Semiconductor Switches,” Proc. of Int. Conf. MEMS, NANO and Smart Systems, 25-27 Aug. 2004, Banff, Canada.

[164] C. Palego et al., “A dual-band MEMS reconfigurable filter for a multi-standard radio front-end,” Proc. 38th European Microwave Conf., Amsterdam, The Netherlands, pp.587-590, October 2008.

[165] G. M. Rebeiz, “RF MEMS Switches: status of the technology,” The 12th Int. Conf. Solid State Sensors, Actuators and Microsystems, Boston, pp. 1726-1729, June 8-12, 2003.

[166] D. Hyman, and M. Mehregany, “Contact Physics of Gold Microcontacts for MEMS Swithces”, IEEE Trans. Compon. Packag. Technol., vol. 22, pp.357-364, Sept. 1999.

[167] N. I. Dib, R. N. Simons, and L. P. B. Katehi, “New uniplanar transitions for circuit and antenna applications,” IEEE Trans. Microw. Theory Tech., vol. 43, no. 12, pp. 2868–2872, Dec. 1995.

[168] Y. Qian and T. Itoh, “A broad-band uniplanar microstrip-to-CPS transition,” in Proc. Asia–Pacific Microw. Conf., vol. 2, 1997, pp. 609–612.

[169] R. N. Simons, N. I. Dib, and L. P. B. Katehi, “Coplanar stripline to microstrip transition,” Electron. Lett., vol. 31, no. 20, pp. 1725–1726, Sep. 1995.

[170] Y.-H. Suh and K. Chang, “A wide-band coplanar stripline to microstrip transition,” IEEE Microw. Wireless Compon. Lett., vol. 11, no. 1, pp.28–29, Jan. 2001.

[171] T. Chiu and Y.-S. Shen, “A broad-band transition between microstrip and coplanar stripline,” IEEE Microw. Wireless Compon. Lett., vol. 13, no. 2, pp. 66–68, Feb. 2003.

[172] Y. Qian, T. Itoh, "A broadband uniplanar microstrip-to-CPS transition," Microwave Conference Proceedings, 1997. APMC '97, 1997 Asia-Pacific, pp.609-612 vol.2, 2-5 Dec 1997.

[173] W. Tu; K. Chang, "Wide-band microstrip-to-coplanar stripline/slotline transitions," Microwave Theory and Techniques, IEEE Transactions on , vol.54, no.3, pp.1084-1089, March 2006.

[174] Y. Yang, Y. Cai, K. Y. Chan, R. Ramer, Y. J. Guo, "MEMS-loaded millimeter wave frequency reconfigurable quasi-Yagi dipole antenna," Microwave Conference Proceedings (APMC), 2011 Asia-Pacific , pp.1318-1321, 5-8 Dec. 2011.

[175] Y. P. Zhang, M. Sun, K. M. Chua, L. L. Wai, D. Liu, B. P. Gaucher, "Antenna-in-Package in LTCC for 60-GHz Radio," Antenna Technology: Small and Smart Antennas Metamaterials and Applications, 2007 IWAT '07. International Workshop on, pp.279-282, 21-23 March 2007

[176] E. Perahia, C. Cordeiro, P. Minyoung, L. L. Yang, "IEEE 802.11ad: Defining the

Next Generation Multi-Gbps Wi-Fi," Consumer Communications and Networking Conference (CCNC), 2010 7th IEEE, pp.1-5, 9-12 Jan. 2010

[177] P. Cheolhee, T. S. Rappaport, "Short-Range Wireless Communications for Next-Generation Networks: UWB, 60 GHz Millimeter-Wave WPAN, And ZigBee," Wireless Communications, IEEE, vol.14, no.4, pp.70-78, August 2007

[178] P. Pursula, T. Vaha-Heikkila, A. Muller, D. Neculoiu, G. Konstantinidis, A. Oja, J. Tuovinen, "Millimeter-Wave Identification—A New Short-Range Radio System for Low-Power High Data-Rate Applications," Microwave Theory and Techniques, IEEE Transactions on, vol.56, no.10, pp.2221-2228, Oct. 2008

[179] Y. Cai, Y. J. Guo, and A. R. Weily, "A Frequency Reconfigurable Quasi-Yagi Dipole Antenna, " IEEE Antennas Wireless Propag. Lett., vol. 9, pp. 883-886, 2010

[180] E. Siew, K. Y. Chan, Y. Cai, Y. Yang, R. Ramer, A. Dzurak, "RF MEMS-integrated frequency reconfigurable quasi-Yagi folded dipole antenna," Microwave Conference Proceedings (APMC), 2011 Asia-Pacific, pp.558-561, 5-8 Dec. 2011

[181] Y. Yang, Y. Cai, K. Y. Chan, R. Ramer, Y. J. Guo, "MEMS-loaded millimeter wave frequency reconfigurable quasi-Yagi dipole antenna," Microwave Conference Proceedings (APMC), 2011 Asia-Pacific, pp.1318-1321, 5-8 Dec. 2011

[182] L. Gong, K. Y. Chan, and R. Ramer, "A beam steering single-arm rectangular spiral antenna with large azimuth space coverage," 2013 IEEE 14th Annual Wireless and Microwave Technology Conference (WAMICON), 7-9 April 2013

[183] A. A. Eldek, "Design of double dipole antenna with enhanced usable bandwidth for

wideband phased array applications," Progress In Electromagnetics Research, Vol. 59, 2006

[184] P. Y. Qin, Y. J. Guo, A. R. Weily, L. Chang-Hong, "A Pattern Reconfigurable U-Slot Antenna and Its Applications in MIMO Systems," Antennas and Propagation, IEEE Transactions on, vol.60, no.2, pp.516-528, Feb. 2012

[185] Y. Yang, K. Y. Chan and R. Ramer, "60GHz Pattern Reconfigurable Quasi-Yagi Antenna-Proof through Computational Design," in Proc. iWAT 2014

[186] C. A. Balanis, "Antenna theory: analysis and design," 2nd ed., New York: John Wiley & Sons, Inc., 1997.